

Diss. ETH No. 27315

Synthesis of Nanoporous Graphene Membranes for Separation

A dissertation submitted to
ETH ZÜRICH

for the degree
DOCTOR OF SCIENCES

presented by

Karl-Philipp Schlichting

MSc. Mechanical Engineering ETH Zürich

born February 9, 1990
citizen of Germany

Doctoral Committee

Prof. Dr. Dimos Poulikakos, examiner

Prof. Dr. Patrick Jenny, co-examiner

Prof. Dr. Aleksandra Radenovic, co-examiner

2021

Document typeset by the author using L^AT_EX with the document class book. Figures were prepared with Matlab and Microsoft PowerPoint.

© Karl-Philipp Schlichting, Zurich (2021).

Auch eine Enttäuschung, wenn sie nur gründlich und endgültig ist, bedeutet einen Schritt vorwärts, und die mit der Resignation verbundenen Opfer würden reichlich aufgewogen werden durch den Gewinn an Schätzen neuer Erkenntnis.

—Max Planck, *Königsberg (1910)*

Abstract

Separation of fluid mixtures with the help of membranes occurs ubiquitously in nature and technology. However, the membranes typically limit processes due to inefficient transport, and improving transport efficiency is conventionally targeted by reducing membrane thickness. By this rationale, the ideal membrane thickness is only a single atomic layer thin. Graphene, the single atomic layer thin material, thus, together with its high stability and flexibility, promises to be the ultimate membrane material.

Since pristine graphene is practically impermeable to all species down to a single molecular size, pores in the crystal are required to transform the barrier into a membrane. Early research has focused on finding methods to perforate graphene and study the transport properties; however, no available process has proven to meet all demands for practical applications, and various questions regarding the transport physics remain unsolved. The limited understanding and fabrication methods prevent the application of graphene membrane outside research-based environments, such that graphene membranes could not yet live up to their promises.

This Thesis aims to solve some of the standing issues to understand transport at the fundamental level better and move graphene membranes closer to applications.

First, the thickness paradigm that aims for ever-thinner membranes irrespective of application is challenged. Double-layer graphene membranes containing pores with diameters from ≈ 6 to 1000 nm are synthesized to investigate liquid permeation over a wide range of viscosities and pressures. Pressure driven flow across these atomically thin membranes follows the prediction of Sampson's formula, with permeation being independent of membrane thickness, due to viscous dissipation-limited permeation at the pore entrance. Atomic layer deposition (ALD) is utilized to increase the membrane thickness, and it is found that membranes with aspect ratios up to above one transport similarly efficient as atomically thin membranes, since up to these aspect ratios, the entrance resistance still dominates. Furthermore, ALD coating reduces membrane fouling and thus increases membrane lifetime. The permeation limitation is universal for porous materials and sets an upper bound to viscous transport. The results imply that membranes with near-ultimate permeation should feature rationally selected thicknesses based on the target solute size and introduce a proper perspective to the pursuit of ever-thinner membranes.

On the problem of membrane manufacturing, this Thesis proposes a novel approach to overcome limitations of state-of-the-art graphene membrane fabrication processes: a dry, facile, and scalable process introduces atomic defects by design, followed by selective etching of graphene edge atoms allows to controllably expand the nanopore dimensions from sub-nm to 5 nm. The attainable average pore sizes at 10^{15} m^{-2} pore density promise applicability to various separation applications.

This fabrication process allowed investigating the gas permeation and separation mechanisms of graphene nanopores. It is found that these membranes display molecular sieving at high membrane permeance for the smallest pores (H_2/CH_4 separation factor = 9.3; H_2 permeance = 3370 gas permeation units (GPU)) and smoothly transition to effusion at unprecedented permeance (H_2/CH_4 separation factor =

3.7; H_2 permeance = 10^7 GPU), when expanding the pore sizes from sub-nm to 5 nm.

Single gas, mixture gas, and pressure studies reveal the presence of interweaved transport phenomena of pore chemistry, surface flow, and gas molecule momentum transfer. The scalable graphene membrane fabrication approach in combination with sub-5 nm pores opens a new route employing 2D membranes to study gas transport and effectively paving the way to industrial applications.

Last, the developed pore synthesis approach is adapted to be compatible with low-cost and scalable graphene membrane supports and overall feasibility for roll-to-roll integration. It is demonstrated that up to 5 cm²-sized graphene membranes can be fabricated on porous polymeric support, with the etching-free transfer of the graphene from its growth catalyst. Reducing partially oxidized copper surfaces is key for successful electrochemical delamination, and the reduction of membrane defects was achieved by an optimized fabrication protocol and creating double-layer graphene membranes. Analytical flow modeling is utilized, predicting the large-scale membrane to be promising for nanofiltration applications when pores are introduced. Oxygen plasma exposure was identified as a promising approach to nucleate nanoscale defects in graphene for subsequent pore expansion, and additionally, proof-of-concept, controlled growth of graphene nanopores on its synthesis substrate is achieved.

Zusammenfassung

Die Trennung von fluiden Mixturen mithilfe von Membranen passiert allgegenwärtig in Natur und Technologie. Membranen sind jedoch typischerweise der limitierende Prozessschritt, da Transport durch Membranen ineffizient ist, und daher ist es da üblicherweise Ziel den Transport durch Membranen zu verbessern, indem die Membrandicke verringert wird. Dieser Überlegung folgend, bestünde die ideale Membran lediglich aus einem eine Atomlage dünnen Material. Graphen, das eine Atomlage dünne Material, ist daher, gemeinsam mit seiner Stabilität und Flexibilität, möglicherweise das ultimative Membranmaterial. Perfektes Graphen ist jedoch praktisch undurchlässig für jedwedes Moleküle inklusive einzelner Moleküle; daher sind Poren im Graphen notwendig, um die perfekte Barriere in eine Membran umzuwandeln. Frühe Studien haben sich darauf fokussiert Methoden zu entwickeln, um Graphen zu durchlöchern und anschliessend die Transporteigenschaften zu untersuchen. Allerdings hat bisher kein Prozess gezeigt alle Bedingungen für die praktische Anwendung zu erfüllen und diverse Fragen bezüglich der Transportphysik verbleiben unbeantwortet. Das limitierte Verständnis und Herstellungsmethoden verhindern die Anwendung von Graphen ausserhalb zu Forschungszwecken, sodass Graphenmembranen bisher ihren Erwartungen nicht gerecht werden konnten.

Diese Dissertation zielt darauf ab einige der bestehenden Probleme zu lösen und die Transport auf fundamentaler Eben besser zu verstehen sowie Graphenmembranen näher in Richtung Anwendung zu bewegen.

Zuerst wird das Paradigma der immer dünneren Membranen, unabhängig der Anwendung, herausgefordert. Doppelschichtgraphenmembranen mit Porendurchmessern beim Bereich von ≈ 6 bis 1000 nm werden hergestellt um Flüssigkeitstransport über einen weiten Bereich von Viskositäten und Drücken zu untersuchen. Druckgetriebene Strömungen durch diese atomar dünnen Membranen folgt den Vorhersagen von Sampson's Modell, mit einer Permeation die Unabhängig von der Membrandicke ist, da der Transport durch viskose Dissipation vor der Pore limitiert ist. Atomlagenabscheidung (ALD) wird benutzt um die Membrandicke zu erhöhen und es zeigt sich, dass Membranen über zu einem Längenverhältnis von eins weiterhin vom Eintrittswiderstand limitiert sind. Desweiteren wird gezeigt, dass ALD die Membranverschmutzung reduziert und somit die Lebensdauer der Membranen erhöhen kann. Die Permeationslimitierung ist universell und gilt fuer jedwedem Material und setzt ein oberes Limit für die Permeation von viskosem Transport. Die Ergebnisse implizieren, dass Membranen mit nahezu ultimativer Permeation eine rational gewählte Dicke besitzen sollten, basierend auf der Grösse des Filtrats und geben damit dem Streben nach immer dünneren Membranen eine korrekte Perspektive.

Seitens der Herausforderungen der Membranherstellung, stellt diese Forschungsarbeit einen neuen Prozess der Membranherstellung vor, welcher die Limitierungen der bisherigen Technologies überwindet: ein trockener, simpler, und skalierbarer Prozess fügt atomar kleine Defekte in das Graphen, welche nachfolgend mithilfe selektivem Ätzens von Graphenrandatomen kontrollierbar die Nanoporengrössen von sub-nm bis auf 5 nm Durchmesser erweitert. Die erreichten durchschnittlichen Porengrössen zusammen mit Porendichten von $1 \times 10^{15} \text{ m}^{-2}$ sind vielversprechen für den Einsatz in verschiedenen Separationsanwendun-

gen.

Der Herstellungsprozess erlaubt es ausserdem die Mechanismen der Gaspermeation und - Trennung von den Graphennanoporen zu untersuchen. Es wird gezeigt, dass die Membranen als Molekularsieb mit hoher Permeation fungieren (H_2/CH_4 Separationsfaktor = 9.3; H_2 Permeation = 3370 Gaspermeationseinheiten (GPU)) und stufenlos zur Effusion übergehen mit bisher unerreichter Permeation (H_2/CH_4 Separationsfaktor = 3.7; H_2 Permeation = 10^7 GPU), wenn sich die Porengrösse von sub-nm auf 5 nm ausweitet.

Einzelgas-, Mischgas-, und Druckstudien zeigen das verwobene Zusammenspiel von Porenchemie, Oberflächenströmung, und Impulsaustausch der Gasmoleküle. Der skalierbare Graphenmembranenherstellungsprozess eröffnet einen neuen Weg 2D Membranen für Gastransportstudien anzuwenden und legt den Grundstein für industrielle Anwendungen.

Zuletzt wird der entwickelte Porensyntheseprozess angepasst, damit er mit günstigen und skalierbaren Graphenunterstützungsmembranen kompatibel ist und um die Möglichkeit für Rolle-zu-Rolle-Verfahren zu eröffnen. Es wird gezeigt, dass Membranflächen von bis zu 5 cm^2 auf einer porösen Polymerunterlage hergestellt werden können, die mit Hilfe eines ätzfreien Prozesses von Wachstumskatalyst entfernt werden können. Die Reduktion von partiell oxidiertem Kupfer ist kritisch für eine erfolgreiche elektrochemische Ablösung und die Verringerung von Membrandefekten wurde mit Hilfe einer Herstellungsoptimierung erreicht und mit Hilfe von Doppelschichtgraphenmembranen. Analytische Strömungsmodellierung wird genutzt und es wird vorausgesagt, dass die grossflächigen Membranen vielversprechend für Nanofiltrationsanwendungen sind, sobald die Poren haben. Das Aussetzen der Membrane von Sauerstoffplasma wird als Methode identifiziert um kleine Defekte in die Membranen einzufügen, um diese anschliessend auszuweiten. Des Weiteren wird per Proof-of-Concept gezeigt, dass es möglich ist Graphenporen auch kontrolliert auf dem Wachstumskata-

lysten auszuweiten.

Acknowledgements

This thesis would not have been possible without the support of numerous people, and I am very grateful to each one of them. I would not have completed my dissertation if it weren't for Prof. Dr. Dimos Poulikakos, who enabled me to transition into his research group and from thereon supervised my research. He gave me the freedom, trust, time, and solution-oriented advice that I needed to succeed. His guidance restored my positive working spirit to accomplish my goals. I am deeply grateful for this.

I am also grateful to my committee members Prof. Dr. Aleksandra Radenovic and Prof. Dr. Patrick Jenny, for their evaluation of my thesis.

I want to thank my colleagues at LTNT and NETS sincerely: Seeing each one of you working on cutting-edge technology and pushing the boundaries of knowledge is truly inspiring. I am especially thankful to Dr. Jakob Buchheim and Dr. Roman Wyss for our project together. Jakob, thank you for teaching me your knowledge about the FIB, the liquid flow experiments, and giving me advice when I was still in the early phase of my Ph.D. Roman, thank you for sharing your outstanding knowledge in cleanroom fabrication, scientific methodology, and, most importantly, our continued discussions about science and life long after you graduated. I am also thankful to Dr. Amirhossein Droudian: Thank you, Amir, for sharing your knowledge about the Mass Spec, gas transport, and always bringing a positive spirit to the

lab, irrespective of the circumstances.

I had the fortune to supervise several student projects in the past years, which contributed directly to my research and inspired me in their drive to do outstanding research. Thank you, Anna de Vries, Roman Berger, Nicolas Carmody, Sebastian Lang, Niklaus Leuenberger, and Dmytro Lytvynenko.

Then, I would like to thank Steffen Reidt, Diana Davila Pineda, Ute Drechsler, and Ronald Grundbacher of the operations team at BRNC, who made sure that the tools I needed for my research were always well maintained.

In the most challenging time of my Ph.D., Prof. Dr. Patrick Jenny, Prof. Dr. David Norris, and Dr. Maddalena Velonà offered support and advice that was profoundly helpful; thank you.

I thank all of my friends for enduring my narratives about the excitements of nanopore transport but also supporting me during the setbacks of my studies. Paul Baade, Max Brunner, Raphael Glaesener, Christian Ohm, and Max Willaschek always had an open ear and advice: thank you very much. Special thanks go to my parents and my sister for their continued, unconditional support throughout the last years.

Last, I thank my wife Levke. Your perpetual support, advice, and empathy contributed invaluablely. I am beyond proud to have you by my side and to be at yours.

Contents

1	Graphene Membranes for Separation	1
1.1	Mixing and Separation	1
1.2	Membranes for Separation	4
1.3	Graphene as a Membrane	7
1.4	Motivation, Aim and Thesis Outline	8
2	Membrane Transport Theory	9
2.1	Flow Regimes	11
2.2	Continuum Transport Theory	12
2.3	Non-Continuum Transport Theory	15
2.4	Design Principles	16
3	Status Quo of Graphene Membrane Studies	19
3.1	Gas Transport	19
3.2	Liquid Transport	33
3.3	Ionic Transport	35
3.4	Proton Transport	47
3.5	Discussion	53
4	Liquid transport at the Limit of Atomic Thinness	59
4.1	Graphene Membrane Manufacturing	62
4.2	Liquid Permeation Measurements	67
4.2.1	Experimental Setup	67
4.2.2	Nonlinear Permeation	74
4.2.3	Post Flow Membrane Evaluation	75

Contents

4.2.4	Atomic Layer Deposition to Change Pore Size & Membrane Thickness	84
4.3	No-Slip, Continuum Permeation	89
4.3.1	Pore Size Scaling	89
4.3.2	Pressure Scaling	90
4.3.3	Viscosity Scaling	91
4.3.4	Rational Definition of Infinitesimal Thickness.	93
4.3.5	Upper Bound for Viscous Permeation through Pores	98
4.4	Discussion	100
5	Scalable Manufacturing of Nanoporous Graphene Membranes	103
5.1	State of Graphene Membrane Manufacturing	103
5.2	Selective Nanopore Etching for Graphene Membranes	105
5.2.1	Selective Etching Conditions	108
5.2.2	Pore size quantification	114
5.2.3	Pore Density Control	122
6	Gas Transport at the Limit of Atomic Thinness	127
6.1	Gas Transport Characterization	127
6.1.1	Calibration	128
6.1.2	Experimental Setup & Control Experiments	134
6.2	Transport Analysis	136
6.2.1	Single Gas Transport	136
6.2.2	Mixture Gas Transport	143
6.2.3	Pressure Effects	146
6.2.4	Membrane Performance Assessment	148
6.3	Conclusions	150
7	Scaling-Up to cm²-Scale	153
7.1	Support Membrane and Transfer	156
7.1.1	Proof-of-concept	159
7.1.2	Optimization	162
7.1.3	Origin of Ruptures and Their Reduction	168

7.1.4	Double Layer Graphene	171
7.2	Defect Nucleation	180
7.3	Nanopore Growth	180
7.3.1	Proof-of-concept	181
7.3.2	Image Analysis and Quantification	184
7.3.3	Nanopore Growth Dynamics	185
7.4	Transport Estimation	187
7.5	Discussion	191
8	Conclusions & Outlook	195
8.1	Conclusions	195
8.2	Outlook	198
	References	201
	Curriculum Vitae	229
	Publications	231

Chapter 1

Graphene Membranes for Separation

1.1 Mixing and Separation

The separation of mixtures is omnipresent in nature and technology: from evaporating seawater as part of the natural fresh-water cycle, down to water transport across cell membranes of living organisms as well as in evaporative cooling in power plants, down to nanochannel transport across membranes for water desalination. Pure fluids are integral for petrochemical, agricultural, and electronics industries for chemical compounds and fuels, food, and transistors at the origin of a plethora of value chains or the backbone of entire industries. In the light of the society, the importance of separation applications equally stems from their vast impact on down-the-value-chain products and the associated energy costs, in fact roughly 50 % of the industrial energy consumption is for separation processes,¹ and the resulting global warming impact.

1. Graphene Membranes for Separation

Separation of mixtures of the preceding examples is only a technical problem because the involved components mix spontaneously when brought into contact such that they are naturally found as a mix instead of pure components. The fundamental driving force that results in mixing is randomness: Imagine a box containing two types of molecules, idealized as balls of two colors, separated by a wall in the center (Figure 1.1 a). The balls move freely in space in random directions and collide with each other. Imagine now that at one point in time, the wall disappears. Each color is free to occupy more space, and after a while, the balls have spread out homogeneously (Figure 1.1 b). While it is certainly possible to find all blue balls on the right and all red ones on the left at a later point, it is more likely to find the balls in some mixed configuration, since there is a larger number of possibilities to arrange the balls in space in a mixed way compared to arranging the balls in a separated way.

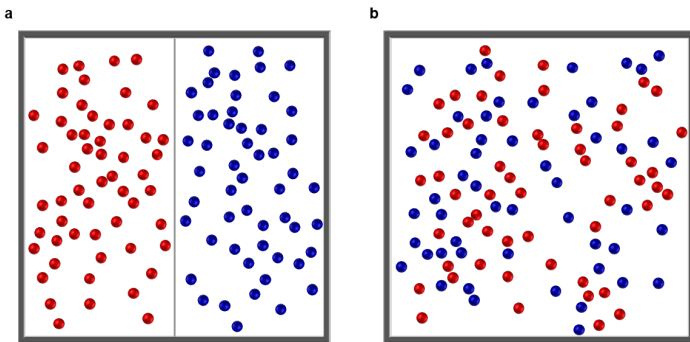


Figure 1.1: Fundamentals of Mixing. **a** A box containing equal balls of either blue or red color moving freely in space but separated by a wall in the center. **b** A box containing equal balls of either blue or red color after the wall in (a) was removed a while ago.

The mathematical description and physical prediction of the occurring phenomena can be achieved from thermodynamics concepts and, more specifically, from the thermodynamics of mixing. Fundamentally, any technological separation seeks to reverse this spontaneous mixing.

Thermodynamics of Mixing and Energy of Separation

To derive the minimum required work to separate the mixture in **Figure 1.1 b** again into the state of **Figure 1.1 a**, several simplifying assumptions are necessary. These may not precisely describe the system in real-world applications such that refinements may be necessary. However, the ideal case provides the minimum theoretical energy required for separation and can thus serve as a benchmark for evaluating a separation technology.

First, assume that the molecules mix and do not show preferred molecular interaction forces with each other or with the other molecules. The separating wall has no volume, such that the volume after its removal is precisely the sum of volumes of each compartment. The compartments are at the same temperature and pressure before mixing. In this idealized situation, removing the separating wall does not change the box's volume, such that no work is done during the mixing of the molecules **Figure 1.1 (a)**.

To separate with theoretical minimum energy requirement, a reversible thermodynamic process is required. The energy corresponds to the maximum work obtainable from a closed system at constant pressure, and the change in Gibbs free energy describes the temperature during mixing, $\Delta_{mix}G$, of ideal solutions.²

$$\Delta_{mix}G = -T\Delta_{mix}S \quad (1.1)$$

as the the negative product of temperature, T , with entropy of mixing, $\Delta_{mix}S$.

The entropy of mixing is given by

$$\Delta_{mix}S = -nR(x_1 \ln x_1 + x_2 \ln x_2) \quad (1.2)$$

1. Graphene Membranes for Separation

with n molecules available in total, the ideal gas constant, R , and the mole fractions, x_i , of the two molecule types.

As an example, the minimum theoretical work to separate 1 m³ seawater at 3.5 % salt concentration with around 50% recovery is 1 kWh.² No separation technology of any kind can undercut this minimum energy requirement.

While the mixing was enabled in the initial thought experiment by the simple vanishing of the separating wall, various ideas were developed to achieve the technical separation of mixtures. These can be broadly classified into the concept they use to achieve separation:

1. Filtration: one or more components of the mixture do not pass through pores of a membrane.
2. Evaporation: the species with the higher boiling point remains while species with lower boiling points evaporate.
3. Adsorption: certain species adsorb to a surface and accumulate there, thus increasing the concentration.

Generally speaking, any separation process utilizes differences in the physio-chemical properties of the mixtures' components to be separated and have advantages and disadvantages depending on the application.

1.2 Membranes for Separation

Given the range of potential technologies to achieve separation, membranes - like any other technical approach - have advantages and disadvantages depending on the application. The key advantages of membranes are separation without phase change, low spatial footprint,

1.2. Membranes for Separation

continuous operation, the simple concept, and versatility.³⁻⁵

Separation without phase change can reduce the energy costs by 90 %¹, and enable medical applications as in hemodialysis. A low spatial footprint comes from integrating large membrane surface areas into compact modules. They can be integrated into factories and machines, for example, in microelectronics fabrication plants, where process liquids are purified immediately before the process step to minimize trace contaminants. Versatility comes from the simple fact that membranes can filter various particle sizes from a mixture such as sand, bacteria, viruses, organic molecules, dyes, and ultimately ions. Lastly, continuous operation is beneficial due to simplicity but also for the dimensioning of materials and reduced material fatigue compared to discontinuous operation.

Nevertheless, of course, membranes also have downsides that inhibit their spread to more applications.

Compared to phase change based separation, membranes typically provide lower selectivity - the ratio of wanted species transport to unwanted species transport across the membrane. Then, wanted species transport across membranes is often very slow, such that the membrane separation step is often the rate-limiting step of an overall process. However, working on the rate-limiting step promises to improve the overall process-performance proportionally to the improvement at the rate-limiting step. From an engineering point of view, this is where technology improvements generate the most value to the overall process.

The following properties characterize the ideal membrane for any separation application, universal for all separation applications:

1. High throughput

1. Graphene Membranes for Separation

2. High selectivity

Once selectivity and throughput meet the goals, improving secondary properties will facilitate widespread use of membrane materials, and may be required to different amounts for different applications:

1. Mechanical stability: operating at higher pressures increases range of applicability
2. Thermal stability: operating at higher or lower temperatures increases range of applicability
3. Chemical compatibility: operating in different chemical environments increases range of applicability
4. Cost of fabrication: often times the separated products are low cost per unit such that the membrane costs need to be low as well
5. Scale of fabrication: many membrane applications require large areas and high numbers of membranes to achieve market relevant impact

Irrespective of membrane type, the first property, throughput, is generally considered to be inversely proportional to the membrane thickness, for constant membrane area and driving force difference.³⁻⁵ As membranes are often the limiting factor in separation processes, it has been a long-standing challenge in membrane science to increase throughput, which often leads to difficulties in selectivity - due to many materials' intrinsic trade-offs - mechanical stability, continuity, durability, and difficulties in synthesis.

What if there was a material that has the potential to meet all of the above requirements?

1.3 Graphene as a Membrane

Graphene is the single sheet form of graphite, carbon atoms arranged in a hexagonal lattice (**Figure 1.2**), and anyone who has ever written with a pencil likely created some micrometer-sized graphene flakes. It was first successfully isolated and integrated into a device in 2004 by Novoselov and Geim from Manchester University⁶, which resulted in a 'gold-rush' on research and the awarding of the 2010 Nobel Prize in Physics to the two physicists.⁷

Soon after its first isolation, its astounding electrical⁶, thermal⁸, and mechanical⁹ properties have been experimentally verified, proving graphene as a 'best in class' material in all of these categories. Of importance for membrane applications are mechanical stability, which was measured on mechanically exfoliate graphene flakes using atomic force microscopy and determined a Young's Modulus of 1000 GPa.⁹ Furthermore, graphene has high thermal and chemical stability making it a promising material for two more membrane ideals.

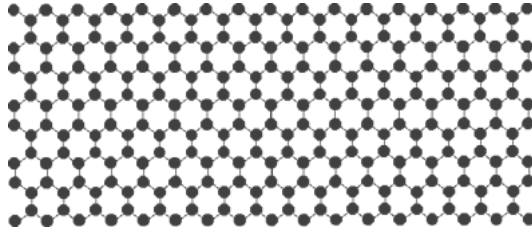


Figure 1.2: The hexagonal lattice of graphene. Graphene is a crystal lattice of sp^2 bond carbon atoms forming a single layer of graphite. The carbon-carbon bond length is 0.142 nm and the pores within the hexagons have an equivalent diameter of 0.064 nm.¹⁰

Crystalline graphene is basically impermeable to gases, even as small as helium, making it an impermeable barrier and not a semipermeable membrane.¹¹ The impermeability stems from the close packing

1. Graphene Membranes for Separation

of the carbon atoms leaving only an open circle of 0.064 nm diameter, far smaller than gas molecules or hydrated ions.¹⁰ However, early theoretical studies have predicted mass transport across nanometric sized pores in graphene to be extremely efficient promising graphene to be the ultimate membrane for any separation application, if pores are introduced into graphene.^{12–14}

The research field of graphene membranes is thus concerned in developing methods to obtain porous graphene with precisely controlled pore size and porosity at scales relevant to applications, and in studying and understanding the separation mechanisms that dominate and control transport of various species across the atomically thin pores in graphene.

1.4 Motivation, Aim and Thesis Outline

This thesis aims to push the knowledge of graphene membrane fabrication technologies and mass transport investigations to bring graphene membranes closer to real-world applications. It is outlined as follows:

1. Identify open challenges in this rapidly evolving field of graphene membranes
2. Study liquid and gas transport across nanoporous graphene membranes
3. Advance the state-of-the-art synthesis technology of versatile membrane fabrication
4. Develop strategies for further technological implementation of graphene membrane manufacturing

Chapter 2

Membrane Transport Theory

An ideal membrane exclusively passes one component of a mixture, while it does not allow transport of another component from a mixture. Starting the previous example in a slightly different configuration where initially (at $t = 0$) both molecules, red and blue, are on one side of a perfect membrane (depicted in green), a mixture is present on the left side, and transport into the full volume of the cell is only possible via the membrane (**Figure 2.1**). The membrane is called semi-permeable in that it allows only the passage of blue molecules, while red ones cannot pass. Over time the situation will resemble the right configuration, where blue molecules again occupy the entire volume, including that to the right of the membrane, while the red molecules cannot pass the membrane. The membrane is ideal because not a single red molecule passes to the right such that the selectivity of the membrane is infinite.

To analyze and compare membranes, defining commonly used terminology to describe membranes is required. The flow, Q , is the num-

2. Membrane Transport Theory

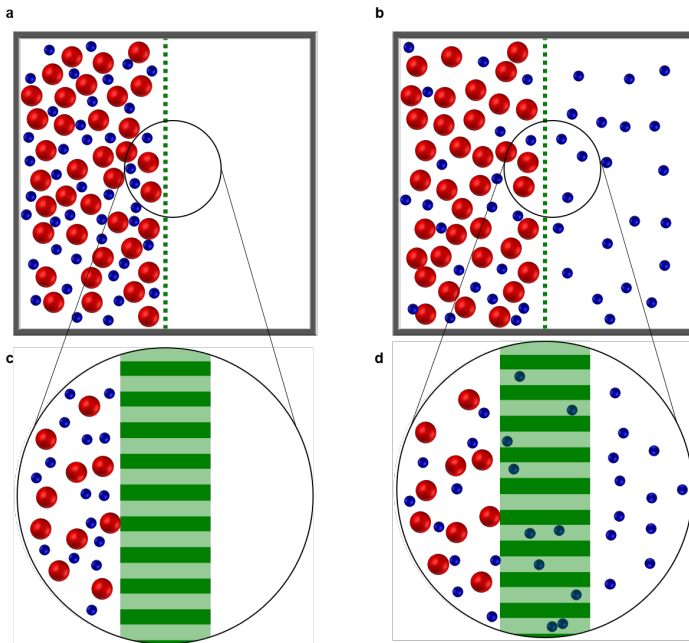


Figure 2.1: The ideal membrane. **a** A box initially containing balls of blue and red color moving freely in space but separated by a semi-permeable membrane in the center. **b** The same box with red and blue balls and the semi-permeable membrane, but after a long time has passed

ber of molecules passing across a membrane per unit time. The flux, $q = Q/A$, is the flow normalized by the membrane area. The permeation, P , across a membrane is the flow normalized by the driving force, ΔP . These terms conventionally describe the performance of membranes:

1. Flux, $q = Q/A$: transport of a species per unit area and time
2. Permeation $Q/\Delta P$: Transport of species across a membrane normalized by its driving force
3. Selectivity, α : Defined as ratio of flux, q of desired species to

flux of undesired species, i , each normalized by their driving force, ΔP , (pressure or concentration) $\alpha = (q_i/q_j)/(\Delta P_i/\Delta P_j)$

4. Permeance $Q/(\Delta P A_{mem})$: permeation normalized by the active membrane area, A_{mem}
5. Permeability $Q t_{mem}/(\Delta P A_{mem})$: permeance multiplied by membrane thickness, t_{mem}

The two primary performance indicators to compare different membranes are the selectivity and the permeance giving information on how well a membrane can select between wanted species and unwanted species together with a metric of how efficient the wanted species passes across the membrane. Often, permeability is used for polymeric membranes to compare different polymer types, while accounting for thickness differences. This thesis will not use permeability as it does not reflect the membrane material's actual capability to generate throughput and, therefore, skews the interpretation.

2.1 Flow Regimes

The flow across membrane channels is essentially a fluid dynamic problem and can follow different laws depending on the fluid flow details. The fluid flow behavior is affected by several dimensionless numbers that compare which physical effects dominate the overall fluid flow behavior. For membranes, the most important is the so-called Knudsen number, Kn , which compares the mean free path a molecule in a fluid flow travels before colliding with another fluid molecule, λ , with the spatial dimension of the flow constricting geometry, d :

$$Kn = \frac{\lambda}{d} \tag{2.1}$$

2. Membrane Transport Theory

The flow constricting geometry for membranes is the pore diameter. Depending on the size of the membrane pores and the physical properties in which the fluid flow happens, the Knudsen number can vary largely, and different fluid flow regimes are defined:¹⁵

1. $Kn \ll 1$: continuum flow regime. The molecules almost exclusively collide with one another and very rarely with the membrane walls. The flow behaves collectively, and the fluid can be treated as a continuous medium, where its constituents' molecular nature does not need to be considered.
2. $Kn \approx 1$ transition flow. The molecules collide similarly often with the walls as with each other, and the collective behavior part becomes less while the random molecular motion starts to have a measurable effect.
3. $Kn \gg 1$ free molecular flow. The molecules rarely collide with each other and mostly with the walls. The random molecular motion of the molecule dominates, and the effects of their collision are negligible.

2.2 Continuum Transport Theory

The mathematical description of continuum transport across membranes can be classified into two types of transport modes or mechanisms, depending on the respective membrane material. These types are dense membranes and porous membranes.

Strictly speaking, every membrane is porous, and the difference is more precisely the dynamic nature of the transport channels: rigid and flexible. Dense membranes are often polymeric, and transport pathways temporarily occur as gaps between the moving polymeric chains. Porous membranes possess a rigid pore structure that is more accurately described as static and continuously available for transport.

2.2. Continuum Transport Theory

The so-called solution-diffusion mechanism is accurate for describing flux across dense membranes using Fick's law.

$$q = D \frac{\Delta C}{L} \quad (2.2)$$

with the diffusivity, D , and the concentration difference, ΔC , across the membrane thickness, L . The mechanism of permeation in dense membranes relies on differences in diffusivity coefficients of the passing molecules, which leads to separation during the passage. Additionally, the dense membranes are also characterized by differences in solubility of the passing species onto and into the membrane surface, such that the passing species driving force, the local concentration at the surface, may differ from bulk concentration. The separation mechanism is therefore known as the solution-diffusion model.

On the other hand, transport across porous membranes is described, according to standard textbook theory, using channel flow and the corresponding Hagen-Poiseuille formalism

$$Q = \frac{\pi r^4}{8\mu} \frac{\Delta P}{L} \quad (2.3)$$

giving a flow, Q , through a straight channel of length, L , with radius, r of a fluid with viscosity, μ , driven by a pressure difference, ΔP , across the length of the channel. Selectivity in porous membranes stems largely from size exclusion, where the rigid channels are smaller than one of the approaching species and selectivity, therefore results.

Therefore, both types of membranes are characterized by inverse proportionality of transport to membrane thickness, which motivates the thickness-reduction efforts across membrane materials to improve membrane permeance. Additional mechanisms that affect selectivity and

2. Membrane Transport Theory

permeance, such as surface charge and play a role as well, depending on the materials and species at hand. The mean free path in liquids is almost always on the order of a few angstroms due to liquids' dense nature. Correspondingly, the Knudsen number of a nanometric pore would very rarely be smaller than one such that one may be inclined to apply continuum flow theories.¹⁶ The standard textbook theory of continuum flow through a circular channel is given by the Hagen-Poiseuille equation; however, several assumptions are made during the derivation of these equations. First, the channel length is assumed to be infinitely long, such that the flow field is fully developed, and entrance effects are negligible. Second, the flow is considered to be without slip at the walls, steady and laminar. While slip at the walls may occur and needs to be tested depending on the surface, flow across membrane pores is almost always in the laminar flow regime since the Reynolds numbers using flows with typical pressures are at the creeping flow limit

$$Re = \frac{uL}{\nu} \quad (2.4)$$

with typical viscosity of water $\nu \approx O(10^{-3})Pas$, channel lengths of the order of microns ($L \approx O(10^{-4})m$) water flow rates at hypersonic speeds ($u > 10^4m/s$) would be required to achieve Reynolds numbers at the threshold of turbulence ($Re \approx 10^3$). Therefore, it is safe to say that all liquid transport across membranes relevant for this thesis is in the laminar regime, more specifically, the Reynolds numbers are often below one, such that the Navier-Stokes equations simplify to the Stokes equation, since inertial effects are negligible and Stokes flow applies.¹⁷

The Hagen-Poiseuille equation predicts inverse proportionality with the channel length or membrane thickness. However, the model predicts infinity flow or a singularity when the thickness approaches zero,

2.3. Non-Continuum Transport Theory

as graphene could potentially be. The problem of the continuum, creeping flow across an infinitely thin orifice, has been theoretically analyzed by Sampson¹⁸ and follow-up works by Roscoe¹⁹. They analytically derived the governing flow equation as:

$$Q = \frac{r^3}{3\mu} \Delta P \quad (2.5)$$

where no thickness dependence of the flow appears. Dagan²⁰ then combined the two models into a more general model for all channel lengths, which considers the inverse permeance of Sampson and Hagen-Poiseuille as flow resistances in series:

$$R_{total} = R_{Sampson} + R_{Hagen-Poiseuille} = \frac{3\mu}{r^3} + \frac{8\mu L}{r^4} \quad (2.6)$$

such that a general flow prediction can be made

$$Q = \frac{r^3}{3\mu} \left[1 + \frac{8L}{3r} \right]^{-1} \Delta P \quad (2.7)$$

assuming that the fluid does not slip along the pore channel walls.

2.3 Non-Continuum Transport Theory

Non-continuum transport is considered to be in the free molecular flow regime if the molecules mostly scatter with the constricting geometry rather than among each other.²¹ Gas separation using membranes can only be achieved in non-continuum flow conditions, as the molecules otherwise stream in a mixed way through the transport channels.

The mean free path can be derived from the kinetic theory of gases²² for an ideal gas at temperature, T , and pressure, p :

2. Membrane Transport Theory

$$\lambda = \frac{k_B T}{\sqrt{2\pi} d_{kin}^2 p} \quad (2.8)$$

With k_B the Boltzmann constant and d_{kin} the kinetic diameter of the molecule. The resulting mean free Knudsen numbers are all > 10 for all ambient pressure single gas and mixture gas experiments. The kinetic diameter is obtained from the effective scattering cross-section simplifying the gas molecules as spheres. For typical experimental conditions used throughout this thesis, ($\approx 300K, 1bar$) the mean free paths are between $50 - 100nm$.

To achieve gas separation, therefore, pore sizes in this range or smaller is necessary. The transport across graphene membranes can thus either be described using transition flow theory or effusion, which is the transport across an infinitely thin aperture²²:

$$Q = A_{open} \frac{\Delta P}{\sqrt{2\pi MRT}} \quad (2.9)$$

2.4 Design Principles

The fundamental design principles of membranes can be derived based on the transport theory across membranes to optimize performance. These are:

1. Uni-sized pores: With pore size distributions as narrow as possible, the best selectivity is obtained for a given size cut-off
2. As thin as possible: permeance increases due to a reduction in internal friction losses during permeation

3. highest possible porosity: permeance increases due to more available transport pathways for permeation

However, it is not clear *a priori* whether the assumptions made in the derivations of the transport models will also prove accurate for fluid transport across graphene membranes. For example, does the no-slip condition hold, does the molecular size of gases play a role, do intermolecular effects or surface effects affect transport noticeably or other unanticipated mechanisms and questions about which pore size results in what selectivity for a given mixture.

Furthermore, it will be the engineers' task to balance properties of membranes, once mechanical stability and pore expansion drawbacks from thinness and porosity begin counteracting each other.

Chapter 3

Status Quo of Graphene Membrane Studies

This section is published in parts as: Schlichting, K. P., & Park, H. G. (2018). Mass Transport Across Atomically Thin Membranes. *Graphene-based Membranes for Mass Transport Applications*, 47, 43. DOI: <https://doi.org/10.1039/9781788013017-00043>

3.1 Gas Transport

The study of gas transport across porous graphene membranes has been motivated by graphene's potential impermeability to gases despite the atomic thinness. Once the graphene is chopped open to bear tiny pores, the thinness of graphene, in turn, acts as an ultimate gas permeator. In this light, the focus of the gas transport study across porous graphene has been geared toward engineering highly selective membrane materials. High selectivity is expected for pores that are of similar size to the kinetic diameters of the gas molecules to be sepa-

3. Status Quo of Graphene Membrane Studies

rated, a mechanism known to be molecular sieving.

The pioneers of the gas separation applications of porous graphene are Jiang and co-workers who have used a density functional theory (DFT) to investigate the transport behavior of light inorganic gases through subnanometer pores on graphene.¹⁴

After removing two hexagonal carbon rings (10 carbon atoms) from a graphene lattice in a modeling domain, they considered two types of pores: one by hydrogen passivation of all the carbon dangling bonds, and the other by nitrogen and hydrogen passivation. Such passivation constricted the pore width from 3.0 Å to 2.5 Å on the basis of the isoelectric surface of the electron density distribution of the pore edge atoms ($0.02 e/\text{Å}^3$). Ballistic transport of H_2 and CH_4 across these model pores undergoes diffusion barriers describable with activation energies of an Arrhenius formula (assuming an identical exponential prefactor).

Once determining the smallest width of a pore to dictate the permeance, they found out that molecules orient preferentially against the pore edges during the passage and that this orientation is reliant on the molecule and edge-passivation pair. The H_2/CH_4 selectivity has been reported as high as $1e8$ for the 3.0 Å pore and $1e23$ for the smaller pore. They attributed the 15-order-of-magnitude rise in the selectivity to the exponential dependence of the gas diffusion barrier, elevating greatly when the constricting width becomes commensurable with the kinetic diameters of the transporting molecules (2.89 Å for H_2 and 3.80 Å for CH_4). Even though they have not extended the modelling beyond the ballistic transport for simplicity, this study has predicted the potentially astounding selectivity of graphene membranes for gas separation and proposed an activation energy of pore passage as an indicator of the cross-graphene-pore gas transport.

Following this pioneering work, Li et al. have investigated the permeation of H_2 , CO , CO_2 , and CH_4 with DFT by considering a graphene pore as large as one benzene-ring size passivated by hydrogen atoms.²³ They show an increasing passage energy barrier for increasing isoelectric surface overlap of molecule and pore in the transition state, elu-

cidating that the electron density distributions of pore and molecule root in the repulsion. Extending a similar analysis to noble gases such as *Ne*, *He*, and *Ar*, Blankenburg et al. have reported that noble gases follow a pathway of a minimum potential energy valley, attributed to attractive electrostatic interaction caused by the large polarizability of the noble gases.²⁴

*NH*₃ can also permeate following the minimum potential pathway for its capability of hydrogen-bond formation with the hydrogen-terminated graphene pore edge. Also, the membrane can deform during the passage of gases due to their strong interaction, which lowers the energy barrier effectively compared with rigid pores. These findings support that not only the size comparison but also the various physical and chemical interactions between the graphene pore and the passing molecules can participate in the cross-graphene-pore gas transport mechanism.

The pore deformation phenomenon has been subsequently investigated in more detail by Hauser and Schwerdtfeger for gases crucial in natural gas processing.²⁵ With the graphene pore system similar to Jiang and colleagues' pores, they observed the pores to adapt their size after removal of the benzene rings and also monitored strong pore deformation during the passage of various gas species.

For the nitrogen-terminated pore, they also observed a slight bending of the *CO*₂ molecule during the passage, explainable by a Lewis-acid-base mechanism of the charge distribution of bent *CO*₂ that shows a propensity to the Lewis-base nitrogen. The non-negligible interaction between the transporting molecule and pore edge can cause the molecular deformation during gas permeation. Thus, a simple comparison between molecular and pore sizes loses its significance beyond the first approximation of permeation/separation.

The first molecular dynamics (MD) simulation of the gas transport (*H*₂ and *N*₂) across the graphene pore has been carried out by Du et al., scanning the pore sizes from 10 C equivalence to 32.²⁶ For the

3. Status Quo of Graphene Membrane Studies

smallest pores, the pore size is smaller than the kinetic diameter of N_2 , and so they observed no N_2 passage.

Unexpectedly, though, as pores opened up large enough to pass N_2 , the calculated N_2 flow rate exhibited a superlinear proportionality with the open pore area, whereas H_2 followed the pore area scaling quite linearly. From the MD simulation, they found out that a layer of N_2 molecules can adsorb to the graphene surface via van-der-Waals interaction, resulting in a surface diffusion of the molecules to outpace the ballistic diffusion.

The unveiled surface adsorption and diffusion of gas molecules at pore dimensions slightly larger than the molecular sieving regime poses significant practical importance; for example, surface diffusion mechanism could deteriorate an otherwise molecular-sieving-level separation factor or could enhance the selectivity towards strongly adsorbing species. Preferential adsorption onto the graphene surface is also confirmed. According to an investigation of adsorption of H_2 , CO_2 , CH_4 , and N_2 , a charge variation of the membrane surface has an influence on the physisorption of the gases.²⁷

A subsequent DFT calculation for hydrogenated pores with sizes of two benzene rings has added that the large quadrupole moment of CO_2 can be related to stronger adsorption to the graphene surface than CH_4 , N_2 , and O_2 .²⁸ Further analyses by MD simulations found out that linear molecules can adsorb flat onto the surface and that CO_2 requires several events for the complete passage of the pore; for the passage, the adsorbate should be oriented properly to overcome the barrier, an event unlikely to happen to molecules approaching from the gas phase to the pore directly. These findings were simplified to a Langmuir adsorption model, leading to an argument that the surface-diffusion-related pore passage is the single, rate-limiting step. Competitive adsorption had a negligible impact on the selectivity because the gas adsorption did not fully saturate the membrane surface in the temperature and pressure ranges scanned in this investigation. On the other hand, Draushuk et al. have proposed a five-step analytical model by making an analogy of the surface-diffusion-incorporated

transport to a surface-site-mediated catalytic reaction.²⁹ The five identified steps are surface adsorption (on the feed side), pore association, pore passage (engagement), surface diffusion (on the permeate side), and surface desorption (detachment). Steady-state solutions of the differential equations of the analytical model for a range of graphene pore sizes from the 2-benzene-ring equivalent to the 32-carbon-atom equivalent brought out that “pore passage” is the rate-limiting step when the pore size is close to that of molecular sieves whereas “surface diffusion” can become the rate-limiting step for larger pores. They further predicted the importance of pressure-dependent permeance and the influence of feed composition due to competitive adsorption, in contrast to direct gas-phase passage. Sun et al. have further compared the relative contributions of direct and surface diffusions for He , H_2 , N_2 , and CH_4 by MD simulation as a function of pore size.³⁰ The surface diffusion mechanism may contribute significantly to the entire permeation, such that its contribution could add up to 16 times higher than the direct transmission part for a transport of such a strongly absorbing species as CH_4 across a 12-C-removal equivalent pore. Surface diffusion may still take part in the trans-graphene transport, by at least an equal amount of contribution, for weakly interacting gases like He and H_2 .

The effect of pore functional groups on permeation, a topic addressed briefly at the early time of the field, has been given renewed attention. Shan et al. looked into CO_2/N_2 separation across pores of 10 to 19 C atom equivalence by MD simulations.³¹ Pore functionalization with nitrogen could render the CO_2/N_2 selectivity as high as 11 for the otherwise unselective pores, attributable to higher electrostatic interaction between nitrogen edge and CO_2 rather than with N_2 , since CO_2 has a higher quadrupole moment. They also showed that the functionalization of the membrane surface with hydroxyl groups could lead to the preferential adsorption of CO_2 to N_2 by about seven times. These two findings agree with the previous observation that the selectivity towards CO_2 relies on the feed partial pressure of CO_2 . Strong interaction among CO_2 molecules that can help overcome the passage

3. Status Quo of Graphene Membrane Studies

barrier turns vigorous with increased partial pressures.

The significance of the preferential molecular orientation in the trans-graphene passage noted earlier is confirmed by MD simulations. Solvik et al. examined the separation of various olefins and kinds of paraffin using all-hydrogenated pores of two-hexagon equivalence.^{14,24,28,32} They considered in their simulation free deformation of the membrane and its pores that had been recognized as crucial in the analysis yet often neglected. The simulation showed surface adsorption limited transport with preferential permeation, or separation, of ethene over ethane. Interestingly, the ethane, the molecule which adsorbs more, is permeating less compared to the less adsorbing molecule ethene. They explain their results by an unfavorable entropic energy barrier for ethane during the passage. During the trans-graphene passage, molecules fall into a potential well, though ethane does not reside well inside the pore compared with ethene. The researchers decomposed the total barrier of the permeation rate model into activation enthalpy, surface adsorption, and entropic terms and observed that the activation enthalpy is similar, so that surface adsorption would, in fact, favor the passage of ethane. However, the entropic barrier causes ethene transport prevalence across the membrane. This finding is rationalized by the small size of the ethane molecule, such that more configurations within the pore are possible during the passage. Hence, its entropic penalty is lower.

Another MD simulation looked into the molecular orientation during the passage of CO_2 and H_2S across 2-3-benzene-ring-equivalent, H - or N -functionalized pores has found out that the linear CO_2 molecule follows a narrow range of orientation during the passage.³³ Radial density distribution extending out of the pore exhibits an accumulation zone within the pores, surrounded by a ≈ 0.5 nm-wide depletion zone, that eventually transitions into a peripheral zone of constant adsorption density. Starting from the adsorption zone, the molecules feel no concentration gradient and thus accumulate homogeneously. However, near the pore, the concentration gradient caused by the pore, or a mass-sink, the molecule diffusion follows the density gradient.

Recently, another aspect of permeation across subnanometer openings has been predicted by combined DFT and MD simulations of CH_4 , CO_2 , and N_2 separation.³⁴ The barrier against the molecular passage consists of a combination of pore entry and exit barriers and varies depending on the pore, functionalization, and the passing molecule. For example, CO_2 usually occupies a potential well within the pore. To leave the pore, the molecule must escape the potential energy barrier. Once a charge is imposed at the pore edge, its strong interaction with the CO_2 quadrupole can adjust the transport energy barrier against CO_2 . This mechanism provides an additional means of separation other than size exclusion or hindered diffusion and may particularly signify for similarly sized molecules.

It is interesting to consider is the effect of a non-permeating species in a gas mixture on the permeance of a permeating mixture. Wen et al.'s MD simulation has delved into this question using CH_4 as non-permeating species and H_2 and N_2 as permeating species through a 13-C-atom-missing pore.³⁵ The presence of CH_4 can decrease both permeances of H_2 and N_2 , and this effect can be more severe for N_2 . They attribute it to two contributions: competitive adsorption and pore blocking. Competitive adsorption is stronger for N_2 as H_2 barely adsorbs to the surface. N_2 , on the other hand, tends to adsorb significantly and puts itself into competition with CH_4 , resulting in less surface occupancy than in the absence of CH_4 . Besides, number densities of both H_2 and N_2 can increase near the pore, though the permeation is curbed by the presence of CH_4 . According to their explanation, CH_4 may partly occupy the subnanometer pores and slow down the transport of H_2 and N_2 effectively. The combined effect of the competitive adsorption and the pore blocking can result in decreased permeance in the presence of a non-permeating species, implying practical importance in gas separations in which more than two species are often present.

Overall, the available literature revealed various facets of the perme-

3. Status Quo of Graphene Membrane Studies

ation mechanism of gaseous molecules across porous graphene membranes. Besides an energy barrier resulting from an interaction between a subnanometric pore and transporting molecules, in association with electron cloud overlapping, adsorption of the molecules to the graphene surface and subsequent surface diffusion significantly influences the permeation and selectivity of the graphene membranes with subnanometric pores. Furthermore, the effects of the pore and surface functionalization, an entropic barrier based on orientation restriction, and the mixture effects such as competitive adsorption and steric hindrance (i.e., pore-blocking) can altogether play a non-negligible role in the trans-graphene membrane transport. It is noteworthy that various simulations predict a wide range of permeance and selectivity values, calling for verification to clarify the deterministic transport mechanisms and to quantify, ultimately, the membrane performance for gas separation.

In this light, the experimental understanding of mass transport across porous graphene membranes can take two categories. The first category comprises publications based on mechanically exfoliated graphene flakes that are high in quality but only as wide as tens of micrometers. With these systems, it was possible to study the impermeability of and transport across subnanometric pores on graphene in the molecular sieving regime. The second category covers publications based on the graphene grown by chemical vapor deposition (CVD) and incorporating intrinsic or artificial pore formation. CVD can synthesize potentially large-scale membranes and is considered the most promising manufacturing method for the real graphene membrane applications. The large area allows for various manufacturing options for the graphene perforation and the membrane formation. Intrinsic defects and ruptures of the synthesized graphene could be a drawback of this approach during membrane manufacturing, while they can provide a molecular transport pathway per se.

The prerequisite for studying the transport across porous graphene is

the impermeability of the pristine graphene demonstrated by Bunch and colleagues.¹¹ Employing the same method, Koenig et al. have pressurized mostly bilayer graphene blisters with applying UV-oxidation etching.³⁶ If well controlled, this treatment may allow the formation of pores in the sub-nanometre dimension, a characteristic size regime useful for molecular sieving of various gases. The transport rates were either measured by atomic force microscope (AFM) tracking of the membrane deflection over time or by a temporal change in the resonance frequency of the membrane while transporting gases. They reported giant selectivity between 10^3 (for H_2/Ar) and 10^4 (for H_2/N_2) of the UV-oxidated bilayer graphene membrane as well as size exclusion of SF_6 having a kinetic diameter of 4.9 Å. The measured permeance matches Blankenburg et al.’s prediction for a H-passivated, 6-C-atom-equivalent pore, but interestingly their selectivity of 2 for H_2/CO_2 differs significantly from the theoretical prediction (10^{17}). Further work of the same group with a monolayer graphene blister having subnanometric pores has revealed that He permeance can vary by a factor of ≈ 5 , if the membrane surface is irradiated with a laser of 2 – 2.3 eV photon energy.³⁷ Additional laser shining could return the permeance to its initial value. They attributed this switchable permeance to the presence of gold nanoparticles that had been evaporated onto the surface. According to their speculation, energy input, such as photon irradiation, could induce surface migration of Au NPs to block the subnanometric pores. However, what remains to be clarified is a negative control of this permeance switching phenomenon for a graphene membrane without the nanoparticles on it. Additionally, stochastic Ne permeance switching of monolayer graphene in the absence of the surface nanoparticles was found. Their subsequent work provides a Hidden-Markov-model-based analysis of this stochastic permeance switching of three monolayer graphene pores that can switch their individual permeance values between “high” and “low” states.³⁸ For gas species having kinetic diameters larger than that of He , the permeance shows various discrete levels that can be mathematically modeled by this binary state system of the three pores.

3. Status Quo of Graphene Membrane Studies

From the switching frequency, the authors could estimate the activation energy value of 1 eV required to switch the permeance state, consistent with the energy barrier of cis-trans isomerization rearrangements. Interestingly, this energy is less than the laser photon energy previously reported to switch a molecular valve from “high” to “low”.³⁷

Due to the size limitations of graphene flakes, mechanical exfoliation is unsuited for membrane applications outside a laboratory. Instead, CVD-grown graphene can potentially take as large a dimension as a few meters such that its use as a large-scale gas separation membrane is a target.^{39,40}

Boutilier et al. have investigated the feasibility of achieving gas selective graphene membranes despite the presence of non-selective defects, ruptures, and incomplete graphene coverage of the support structure.⁴¹

They could show an exponential decrease of leakage pathways across CVD-grown graphene as well as increased gas permselectivity for multiple layers of graphene, confirming that both the total amount of leakage as well as the average size of the leakage path can diminish if multiple layers of imperfect CVD-grown graphene are stacked atop one another. In order to predict the selectivity of graphene, a model was proposed considering a membrane that possesses hypothetical, highly selective subnanometric pores and lies on a porous support, a membrane architecture so-called a thin-film composite. This model illustrates that, despite the presence of unselective defects in the graphene, it may be possible to obtain a highly selective membrane as long as the contribution of the unwanted defects is negligibly small. The authors argue that the support should slow down the non-selective transport through ruptures and only slightly reduce overall selectivity.

Later, they have used the comparable transport impedances of graphene and the support layer to show enhanced Knudsen diffusion permselectivity of an ion bombarded and subsequently PDMS spin-coated PDMS/graphene/PCTE composite.⁴² A further study uses tri-

layer graphene on 20-nm-pored anodic aluminum oxide (AAO) that is etched in O_2 plasma in various durations. Single-gas permeance measurements reveal a permselectivity above Knudsen, indicative of molecular sieving.⁴³ However, the contribution of unselective broken graphene with potentially highly selective subnanometric pores in graphene hampers unambiguous characterization of the graphene pores. Therefore, a model is utilized to estimate the selectivity of graphene pores in the subnanometric regime, when accounting for effects of ruptures and imperfect coverage of the graphene layer. The model predicts He/SF_6 selectivity ranging from 10 to 400 depending on the fabrication conditions. The permeance of their measured composite membranes is quite small due to small pores of a support membrane such that it is comparable to permeances of < 100 nm-thick polymeric membranes. Consequently, these composite structures cannot meet the promise of ultimate permeation of atomically thin membranes. These studies highlight the significant challenges of gas separation using porous graphene on macroscopic areas and suggest strategies to overcome these difficulties.

As the thickness of a pore approaches zero, transport physics will drop out the channel-length dependency along with one pore-width dimension, thus avoiding the singularity – an infinite mass flux – of the Fickian dynamics. The transport dynamics enter into non-Fickian physics. In a continuum mechanics regime, where this zero-thickness pore measures an opening size far in excess of the molecular interaction length scales, a Stokes flow model can provide analytical solutions. For a pressurized fluid flow across an opening through a 2D disc, for instance, the linear relation between the flux and the pressure forcing has been analytically obtained in the form of Sampson’s formula.^{18,44} In the Sampsonian dynamics, the mass flux of fluid is linearly proportional to the pore opening size (diameter) and the pressure forcing, inversely proportional to the fluid viscosity, and invariant to the pore length (or depth). On the other hand, in a molecular flow regime,

3. Status Quo of Graphene Membrane Studies

where pore size is comparable to or far smaller than the molecular interaction length scales, a ballistic transport model such as the effusion or dusty gas model can describe the transport dynamics. Effusion can occur to a gas species when both of the pore size and the depth are much smaller than the mean free path of the species. The simplest description of effusion is related to the Boltzmann gas dynamics; the mass flux across an aperture on a thin wall is proportional to the disparity in the product of gas density and thermal velocity. As the result, the effusive transport flux from one side to the other depends linearly on the pressure and inversely proportional to the square roots of molar mass and temperature. Inherent to the nature of the free molecular transport, the flux from one side to the other is independent on the counter flux, and thus the net flux is determined by the difference in both flux. It has been difficult to verify these flow theories and characterize them experimentally because of the deficiency of a method for manufacturing a nearly zero-thick pore. Characterization of the ballistic effusion could have been made in the high vacuum setup, yet this capability has been still bounded to the Knudsen diffusion limit if pore depth cannot be made ultrathin. One fundamental limit of the material thickness is an atom, and it is graphene, one of the ideal 2D materials that poses the mechanical, physical, and chemical potentials to enable the zero-thickness pores. Still, the primary difficulty in the verification of the aforementioned flow theories and the characterization of the nature of the length-invariant transport physics has lied in the way of perforating the variously sized pores accurately on the graphene in its unsupported, self-sustaining configuration. Researchers have recently found out a physical perforation method of freestanding graphene to investigate this length-invariant mass transport across graphene pores in the wide range of transport regimes from free molecular to continuum. Celebi, Buchheim et al. have applied the focussed ion beam (FIB) technique to drill well-defined pores with diameters ranging from sub-10 nm to 1000 nm, on freestanding double-layer graphene (as thick as approximately two C atoms).⁴⁵ Preparation of a myriad of similarly sized pores can facilitate the di-

rect atmospheric characterization of the gas transport rate across, for example, pores smaller than the gas mean free paths. With this technical breakthrough, they verified that the effusion mechanism dominates transport in the free molecular regime, whereas in the continuum flow regime of larger pores, a modified Sampson’s formula describes the non-Fickian dynamics. Furthermore, a transport minimum at Knudsen number around the unity, often observed for finitely thick channels and ascribable to gas-and-pore-wall friction, was unobserved for the graphene pore, confirming the unique transport mechanism across the 2D pore. Gas permselectivity is scaled to the inverse square root of molar mass, just as predicted by Graham’s law of effusion.

Despite the theoretical and experimental investigations that revealed many findings on the gas separation behavior and the transport mechanism across porous graphene membranes of various pore sizes, still, important questions remain unanswered. Particularly for graphene membranes with few-nm to sub-nm pores, a unified picture of selectivity and permeance remains to be established considering the interplay of molecular-level interactions among the membrane, permeating gas, and other gas species. The effect of surface diffusion may cause a deviation from ever-larger selectivity for ever-smaller pores as predicted for H_2 - N_2 separation for the subnanometric pores. Figure 1 shows a comparative analysis of the H_2 - N_2 separation factor for pores of various sizes and sources. The separation factor predictions vary rather largely up to two orders of magnitude, also conflicting with one another for the transport favoring species: i.e., hydrogen-selective or nitrogen-selective. This uncertainty needs clarification about the true separation factor of pores near 1 nanometer in size. Furthermore, the membrane-based gas separation application demands the actual molecular sieving selectivity of CVD-grown defective graphene in the practical mixture separation process. Along with this reasoning, the challenge of scaling up the membrane area needs to be taken up, as practical membranes will require membrane areas ranging from meters to even thousands of meters, although this argument remains

3. Status Quo of Graphene Membrane Studies

to be further discussed in the community. For subnanometric pores, the self-healing phenomenon can pose a great challenge to the membranes' lifetime.⁴⁶ Here, effective approaches for pore edge stabilization by functionalization or other means need to be established.^{47,48} Eventually, porous graphene membranes need to compete with other types of gas separation membranes such as zeolites, carbon molecular sieves, carbon nanotube membranes, graphene oxide, metal-organic frameworks, and others.⁴⁹ Chemical stability, mechanical strength, temperature as well as pressure requirements, and appropriate support material need to be investigated to find the best-suited material for a targeted gas separation application.

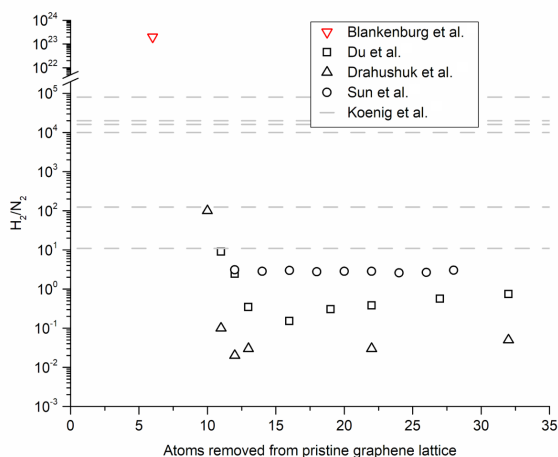


Figure 3.1: Gas Selectivity vs. Pore Size. H_2-N_2 selectivity values from various simulations and experiment, with respect to graphene pore size (number of C atoms removed from a graphene crystal). A strong disagreement exists among simulations for pores with size equivalence to more than ten C atoms. Symbols represent the corresponding study (inverted triangle²⁴, square²⁶, triangle²⁹, circle³⁰, line³⁶); colours represent chemical group at the pore edge. Black and red represent no and hydrogen functionalization, respectively. Grey represents unknown functionalization.

3.2 Liquid Transport

Liquid transport across porous graphene membranes is of interest not only for the fundamental understanding of transport phenomena but also for various applications potentially encompassing from filtration and desalination to biomedical engineering processes such as dialysis and DNA sequencing.

Water Transport across Porous Graphene Membranes

The transport of water across graphene membranes was investigated in Suk and Aluru's MD simulation that considered 0.75-nm-wide and 2.75-nm-wide pores on graphene, and the results were compared to the state-of-the-art water transport through carbon nanotubes (CNT).^{50,51} A very small (0.8 nm) pore of graphene can transport water slightly slower rate than a similarly wide CNT conduit can do, which is related to the frequency of water dipole rearrangement during the passage. For both graphene- and CNT pores, water molecules take a single-file configuration in transporting in these tiny pores. However, water molecules in the 0.8-nm-wide CNT keep a single dipole orientation most of the time during the passage, while water dipoles in the graphene pore can frequently alternate in a rather random orientation. This fluctuation in the dipole orientation requires energy, and thus transport in the subnanometric graphene pores can take a slower rate than the water conduction across CNT with a similar diameter. Across 2.75-nm-wide pores, on the contrary, the simulation resulted in water transport rates to be faster for graphene pores than CNT. Unlike a pluglike profile in CNT, a velocity profile of the water flow takes reportedly⁵¹ a parabolic one in the graphene pores. A follow-up simulation investigated water transport across graphene pores with various diameters from subnanometre to 4 nm diameter and tried to see if it can be modeled with a continuum dynamics theory: an ad-

3. Status Quo of Graphene Membrane Studies

justed Hagen-Poiseuille (HP) equation.⁵²

Instead of the membrane length (0.54 nm), a pore-diameter-dependent hydrodynamic membrane length is utilized with accounting for entry and exit pressure losses, which occur before and after the pore. Besides, regarding a total flow enhancement, the authors observed an increase in slip length that competes with an increase in water viscosity for nanometric pores. According to the authors' claim, it is a layered configuration of water H-bond network in front of and behind the graphene nanopore that can lead to a decrease in the cross-pore water diffusion coefficient, ultimately increasing the water viscosity during the passage. The layering may thus reduce the probability of a water molecule to transmit from one water layer into another, thus resulting in increased water viscosity.

Another study focusing on water transport across graphyne, a related structure to porous graphene, has found out an even stronger increase in the water viscosity that is inversely proportional to the sixth power of the graphyne pore characteristic length and attributed to attractive forces stemming from the Lennard-Jones potential that induces stronger H-bond orientation within the first few water layers directly over the membrane surface.⁵³ Even though the earlier report by Suk and Aluru⁵² showed qualitative results of water viscosity in nanoconfining graphene pores as well, quantitative scaling differs between these two studies, which demands further investigation for the exactly scaling and mechanism and also for the validity of the water viscosity alteration hypothesis itself.

The effect of pore functional group, which had been excluded in the previous study, has been taken into account by Cohen-Tanugi and Grossman for pore sizes in the subnanometric regime possibly suited for desalination.⁵⁴ Hydrogenated and hydroxylated pores were compared.

It was found out that hydrogenated pores transport water significantly less than the hydroxylated pores for comparable open pore area. They attributed this finding to less H-bonding chance between transporting water molecules and the hydrogenated pore edge such that the water

molecules transfer across the pore in a more ordered manner. This picture can be interpreted as an entropic barrier imposing an (activation) energy penalty for the water passage across the subnanometric pores of graphene.

Water transport across graphene pores in the continuum pore-size regime has been probed experimentally by Celebi, Buchheim et al., who prepared precise pores sizes from 50 nm to 1000 nm via FIB drilling on freestanding graphene.⁴⁵ They demonstrated that the unique transport properties of a double-layer CVD graphene membrane could not be described accurately by the HP formalism, but instead the transport physics follows the model of proposed by Sampson. They were able to demonstrate that resistance to water permeation across the pore is accurately described by considering the entrance resistance alone, while pore passage resistance is negligible, a conclusion in agreement with Sampson's formula. Mathematically, the pore-size scaling of the cross-2D-opening transport follows the third power of the pore diameter instead of the fourth power as the HP formalism demands.

Figure 3.2 shows measured, simulated, and analytical predictions of the per-pore-permeance of water across nanopores in porous 2D barriers. Sampson's theory can be seen to describe transport accurately for all pore sizes, while H-P equation significantly deviates from experimental values for any pore larger than a few nanometers.

3.3 Ionic Transport

The study of the transport of ionic solute across nanoporous graphene membranes is relevant in a plethora of technologies such as desalination, biomedical applications, batteries, and fuel cells.

Therefore, significant efforts have been made to understand and control ionic solute passage or rejection with nanoporous graphene membranes.

The first computational study in 2008 considered the transport of ion

3. Status Quo of Graphene Membrane Studies

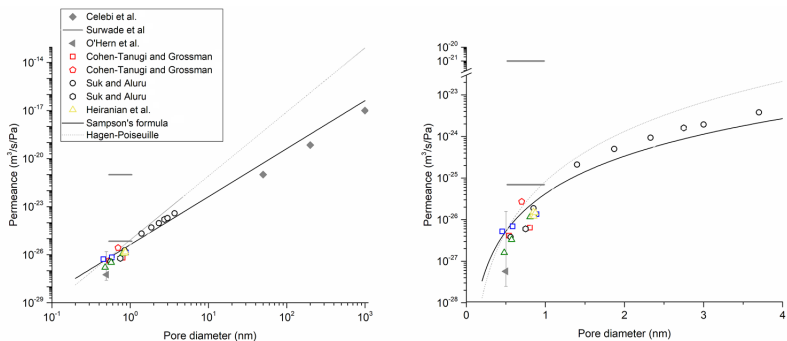


Figure 3.2: Per-pore-permeance as function of pore diameter of various simulation and experimental data. Sampson's formula is accurate for all pore diameters contrary to Hagen-Poiseuille formalism. Symbols represent the corresponding study (diamond⁴⁵, line⁵⁵, tilted triangle⁵⁶, square⁵⁴, pentagon⁵⁷, circle⁵², hexagon¹², triangle⁵⁸); colours represent chemical group at the pore edge. Black and red represent no and hydrogen functionalization, respectively. Grey represents unknown functionalization. Dark red represents molybdenum edge atoms and green mixtures of molybdenum or sulphur atoms. Green and dark yellow represent Mo only and Mo-S-mixed pore edge atoms in MoS_2 . The solid black line is Sampson's model^{18,19}, dashed line is Hagen-Poiseuille model. Water density of 1 g/cm^3 is assumed unless the respective study provides more information.

solute across two distinct subnanometric graphene pores, one with a hydrogen-terminated edge and the other having an edge terminated with fluorine (F) and nitrogen (N).¹³ Based on an electronegativity argument, the hydrogenated pore is expected to be slightly positively charged, while the F-N functionalization would cause negative charges to face to the pore center. Under an external electric field, the F-N functionalized pores show cation-selective transport, and the hydrogenated pores are anion-selective. Transport of various ions shows transmission rates consistent with the hydration radii of the ions considered (Li^+ , Na^+ , K^+ , F^- , Cl^- , Br^-), indicating possible size selectivity.

Electrostatic attraction determines whether the respective ion-pore combination enters and passes a given pore, while the transport efficiency (or rate) depends on the size and the energy penalty associated with the hydration shell of each ion. Consequently, this study revealed

the potential of a subnanometric graphene pore to act as an ion gator. A later study has extended the analysis to larger pores up to 2 nm in diameter and thus simplified it by ruling out the size selectivity.⁵⁹ Still, the authors observed ion-selective transport in these sub-2-nm pores if the pore edge is charged properly. Negative charges will usher cations while impeding the passage of anions, in agreement with the previous study. This behavior is reminiscent of the Donnan exclusion theory in which counterions have a higher concentration within the membrane than in solution due to electrostatic interaction between ion and pore charges. Interestingly, the ion selectivity trend still maintains even though the Debye screening length is much smaller than the pore diameter (0.3 nm), raising a question that calls for additional investigations.

Analyzing the ion transport across non-functionalized, uncharged pores with sub-5-nm diameters, Suk and Aluru have looked into ion conductance and mobility through MD simulation.⁶⁰ They reported physical chemical aspects of aqueous ion solutions within these pores. In detail, they found out that the number of water molecules within the first hydration shell of K^+ and Cl^- ions remains constant for pore sizes up to 1 nm. Smaller pores show a reduced coordination number that is attributed to steric exclusion and dehydration effects. However, the coordination number reduces merely slightly, indicating that a passing ion can compose its hydration shell from water molecules of both sides of the atomically thin graphene membrane. Simultaneously, the pore conductance decreases due to both causes: lowered concentration of ions within the pore and reduced ion mobility near the pore. The lowered concentration originates from a combination of steric hindrance and hydration energy penalty, while the ion mobility is reduced for ever-smaller pores for impeded ion diffusion. The impeded ion diffusion is attributed to the water layering configuration on both sides of the pore as reported in the previous simulation.¹²

These diameter-dependent concentration and mobility collaborate to deviate the nanopore's ion conductance from the value predicted on the basis of the bulk properties if the pore diameter approaches a sub-

3. Status Quo of Graphene Membrane Studies

nanometric dimension. For pores smaller than 9 nm in diameter, the continuum model description becomes erroneous such that their empirically derived diameter-dependent properties should be applied for an accurate description of graphene pore conductance.

Selective ion passage across subnanometric graphene pores can also help understand biological ion channels, as shown by He et al.'s MD simulation.⁶¹ By mimicking biological ion channels by way of attaching carbonyl or carboxylate groups to the pore edge, it is possible to achieve preferential K^+ transport over Na^+ as is seen in biological ion channels under applied bias. Under applied voltage bias, K^+ is coordinated by one carbonyl group more than Na^+ and thus is selectively transported, as the experienced passage barrier of K^+ is smaller than Na^+ . Furthermore, Na^+ is observed to bind more strongly to carboxyl groups than K^+ leading to preferential Na^+ passage over K^+ in the smallest pore at low voltage since the bound Na^+ blocks K^+ . Na^+ is transported by a knock-on mechanism and due to stronger Na^+ interaction with the pore-edge functional groups, it is more likely to replace a Na^+ with a new Na^+ rather than a K^+ . Therefore, Na^+ selectivity can result. At high voltage, however, Na^+ cannot block the pore anymore, since the carboxyl group reacts to the larger electric field by swinging out of the graphene plane. Then, K^+ ions are not blocked from passage anymore, and since Na^+ is attracted strongly to the pore edge, its permeation rate decreases.

Graphene's potential to selectively transport ions also raises the question about complete ion rejection that would imply a membrane feasible for desalination applications. Cohen-Tanugi and Grossman have delved into this question by means of MD simulation for various subnanometric pores functionalized with OH- or H+. ⁵⁴ For effective pore diameters above 0.55 nm, the pores lose their rejection capability, but below that threshold selectivity up to 100 % can be achieved. At a given pore size, hydroxylated pores show lower rejection of salt ions, possibly attributable to the H bond between hydroxyl groups and hydration-shell water; the free energy barrier could be lowered if water molecules from an ion hydration shell could be replaced by a hydroxyl

functional group at the pore edge during the passage, a mechanism the hydrogenated pore is missing. Interestingly, the subnanometric graphene pores lose the ion rejection capability as pressure increases. The authors hypothesized that the larger the effective volume of an ion hydration shell, the more sensitive the graphene pore to a pressure increase; however, facilitated dehydration of salt ions during passage at higher pressures may also explain this observation. Furthermore, the simulation conditions render water in the compressible regime, affecting the salt hydration layer. Still, linear extrapolation of salt rejection of a 0.8-nm-wide pore to practical pressures (e.g., 5 MPa) results in nearly 100 % salt rejection, which raises the question of how salt rejection and pore size are related at lower pressures and the possibility of desalination with pores larger than stated in this study.

Apart from graphene, other 2D materials give a similar promise to high permeation due to their thinness. An MD study of water desalination across nanopores in monolayer molybdenum disulfide (MoS_2) has, in fact, revealed 70 % higher permeance than that across graphene pores.⁵⁸

The unique structure of MoS_2 allowed for a comparison of three different pores with Mo-only, S-only, or a mixture of those atoms to be located at the pore interior. A pore with Mo edge atoms shows the fastest transport, while pure S atoms are the slowest transporters of water. A difference between these pores is that Mo pores have an hour-glass cross-section due to the atomic structure, while S pores do not have this geometry. The authors contribute the fast flow to this hour-glass geometry and furthermore to the hydrophilicity of the Mo sites. However, the application of the concept of hydrophilicity and hydrophobicity at the atomic level is questionable, as the hydrophilicity of materials at the macroscale can change significantly under nanoconfinement or structuring. Although the authors agree with Cohen-Tanugi and Grossman in that faster permeating pores reject fewer ions, their simulation shows around 95 % rejection for both MoS_2 and non-functionalized graphene, while Cohen-Tanugi and Grossman have reported merely 40 % rejection for similar pore sizes

3. Status Quo of Graphene Membrane Studies

and pressures.⁵⁴

Such a remarkable difference demands further investigation of the true rejection capability of atomically thin membranes for given pore size, pressure, and chemical functionalization. The authors further extended the analysis to other transition metal dichalcogenides to observe that mainly the metal component dominates permeation and salt rejection capabilities.

The first experimental characterization of ionic transport across nanoporous graphene was published in 2010 by Garaaj et al.⁶² They showed the nanopore conductance of CVD graphene to be almost linearly increasing with diameter. From their conductance measurements with various pore diameters, it was possible to extract the effective insulating membrane thickness to be 0.6 nm, a value that is confirmed by DNA translocation measurements with a 5-nm-wide pore and matches well with the theoretical work of Suk and Aluru⁶⁰. Using the DNA translocation experiments, they could show sub-nanometre resolution of graphene for DNA discrimination, rendering atomically thin porous graphene a promising candidate for DNA sequencing application.

Extending the analysis of the ion conductance to pores up to 2 nm, Jain et al. have characterized a current-voltage behavior across intrinsic defects of CVD graphene, in resemblance to biological ion channels.⁶³ A Nernst-Planck model incorporating electrostatic and steric interaction of a graphene pore of variable diameter and charge with a single ion could allow extracting transport properties of the pores. Linearity between current and voltage is attributed to uncharged pores with diameters above the hydrated diameters for the ions such that a charge-neutral pore with pore size larger than the hydrated ion radius cannot impose steric hindrance on the passing ion. Voltage-activated behavior could be attributed to uncharged nanopores that sterically hinder the hydrated ion from passing. The nonlinear current increase above a certain threshold voltage can originate from increased ion dehydration due to the higher electric-field driving force. At smaller

electric fields, the dehydration barrier strongly impedes ion passage leading to small currents. The presence of charge at the pore mouth may alter the transport in two possible ways: a charge that is positioned symmetrically could result in the current-saturation behavior by imposing electrostatic repulsion to passing ions, while an asymmetric placement of the charge at the pore mouth yet out of the pore plane could produce a rectified current-voltage characteristic. Here, the asymmetric placement may couple the perceived near-pore electric potential to the direction in which an ion permeates, causing an asymmetric current-voltage behavior. In some cases, rapid current fluctuations are observed for samples that otherwise show voltage-activated behavior. This current fluctuation is attributed to protonation-deprotonation transition because of time-scale similarity and power spectra analogous to those obtained for the protonation-deprotonation transition. What is not clear, though, is the otherwise voltage-activated behaviour for these devices which was previously attributed to steric hindrance in the absence of charge, while protonation induces pore charge alteration. This seemingly conflicting behavior calls for further examination. Still, the remarkable similarity to transport in biological channels lends graphene nanopores eligibility as a model platform to mimic biological ion channels.

The smallest nanopore thus far probed for ionic transport is 0.3 nm in diameter perforated into single layer MoS_2 membranes.⁶⁴ Opening pores in MoS_2 by electrochemical means allowed for controlled fabrication of single pores in suspended MoS_2 . For a 0.6-nm-wide nanopore, current-voltage characteristics show negligible current below a certain threshold voltage upon which the current non-linearly increases. The voltage range in which current is suppressed depends on the pore size and the cation valence that passes through the pore. The nanoelectronics concept of Coulomb blockade is applied to ionic transport to explain the observed phenomena. This model dictates that an individual ion can block a nanopore to curb the other ions from passing it, yielding negligible current at a small bias. Increased voltage bias can release this blockade through a mechanism that augmented elec-

3. Status Quo of Graphene Membrane Studies

trostatic interaction between cations in the vicinity of the nanopore removes the cation from the pore eventually. Negative charges at a nanopore could cause cations to bind to it, resulting in current blockade. By changing the pore size, the authors argued dehydration energy penalty of ions to dominate the current blockade for sub-0.6-nm-wide MoS_2 nanopores while justifying an ohmic current-voltage behavior for super-1-nm-wide nanopores that are too large for a single ion to block them. Their observed current-voltage characteristics also resemble biological ion channels of dimensions similar to their nanopores.

These researchers have furthermore employed concentration-gradient-driven selective ion diffusion across an individual nanopore on monolayer MoS_2 to demonstrate a power generator.⁶⁵ With pores ranging from 2 to 25 nm, the selective ionic passage could be achieved, attributed to negative surface charge evidenced by conductance saturation at low concentration and increased conductance at higher pH. The surface charge is capable of screening anions due to significant Debye length (10 nm), resulting in a net positive current following the concentration gradient. The smaller the pore, the higher the ion selectivity of the nanopore, resulting in larger voltage generated at the expense of the smaller current. Similarly, lower selectivity of larger pore induces a lower voltage, yet at larger current, a trade-off that hints at an optimal nanopore size to maximize power generation. If having an average pore diameter of 10 nm at 30% areal porosity, a membrane that bears the nanopores may potentially generate as great a power density as 1 MW/m² thanks to efficient transport across the atomically thin membrane. However, the sub-additive ion-current increase may be expected as well for 2D porous membranes as has previously been observed for solid-state nanopores.⁶⁶

While the role of surface charge on MoS_2 that screens ion passage is based on the Debye layer thickness, Rollings et al. have probed selective ionic transport across graphene nanopores where the Debye layer is much smaller than the pore size.⁶⁷ For up to 50 nm in pore diameter, K^+ -to- Cl^- selectivity near almost 100 and relies on the solution/electrolyte pH suggesting a mechanism of protonation-

deprotonation of chemical moieties at the pore edge. A pH scan reveals that the graphene nanopore edge is negatively charged at neutral conditions. However, since the Debye screening length (1 nm) is much smaller than the pore diameter and charge screening alone from the pore edge cannot explain the observed selectivity, another mechanism for selectivity needs to be conceived. Ion selectivity of pores much larger than the Debye screening length is rationalized by negative surface charge of graphene that can attract a mobile cloud of screening cations. These mobile cations can diffuse along the graphene surface and cross around a pore edge, causing net ionic current to be cationic. This hypothesis is supported by conductance measurements at pH 8 and 2 that show higher transmembrane ion conductance at pH 8, indicating that more cations screen the negative surface charge of graphene than in the pH 2 case. Numerical solutions of Poisson-Nernst-Planck (PNP) equations for surface charge density of null and -0.6 C/m^2 confirm that results of the strong negative charge case agree with the measurements well. In comparison to Feng et al., Rollings et al. reported that approximately 10-fold more surface charge may cause the high selectivity steadily even at a pore diameter of 50 nm.⁶⁷ The origin of the surface charge is not fully understood but may be related to their sample preparation method involving voltage pulsing, given that other researchers are reporting much weaker selectivity at smaller pores.⁶⁸

Complete ion rejection across subnanometric pores of monolayer graphene has been reported by Surwade et al., implying the potential of graphene for a water desalination membrane.⁵⁵ Subnanometric pores could be created by O_2 plasma treatment, as evidenced by aberration-corrected scanning transmission electron microscopy. By contacting one side of the graphene membrane to deionized water at 40°C , they measured extremely high mass flux across the O_2 -plasma-treated graphene membrane, which is surprising and calls for further investigation of phase change in nanoconfinement. Subsequently, ionic current measurement of this membrane (0.5-1-s-long O_2 plasma treatment) obtained none to very low ion conductance, indicating ion rejection

3. Status Quo of Graphene Membrane Studies

and the potential as an effective desalination membrane. Repeating the initial permeation experiments with an ionic solution shows much slower water permeation and almost complete ion rejection for <1 s plasma treatment time. Osmotic water flow experiments further reveal the semipermeable nature of the membranes and their desalination capabilities. The osmotically driven water transport rate occurs exclusively in the liquid phase and matches well with theoretical predictions.

Any real membrane for liquid-phase separation applications is likely to be grown by CVD and of macroscopic size. Membranes prepared in this way often accompany intrinsic defects such as pinholes from graphene growth or ruptures from membrane fabrication. As was similarly probed for gas transport, O'Hern et al. have investigated transport across intrinsic defects of graphene over a macroscopic area of $O(10)$ mm.^{41,69} They find inhibited transport of TRMD (ca. 12 nm in size), while KCl, allura red, or TMAC are not significantly impacted compared with a bare substrate membrane of PCTE, when corrected for uncovered bare PCTE areas. This reveals the presence of intrinsic defects of 1-15 nm in size, as is confirmed by electron micrographs. Control over subnanometric pore sizes in a potentially scalable process has been achieved in a later work using energetic ion bombardment of CVD graphene first with subsequent wet chemical etching to grow defects into permeable pores.⁹ For a certain etching time, it was possible to demonstrate enhanced KCl transport compared with Allura red, supporting a size exclusion argument and indicating generation of pores larger than KCl (0.7 nm) but smaller than Allura red (1 nm). Since macroscopically grown CVD graphene often contains both intrinsic defects and ruptures originating in membrane handling, a two-stage strategy can be applied to seal membrane defects.⁵⁶ In the first stage, atomic layer deposition (ALD) of ca. 3.5-nm-thick hafnia (HfO_2) was applied targeted to close defects below 15 nm in size, after which interfacial polymerization (IP) of nylon-(6,6) was utilized for sealing larger defects that originate from ruptured graphene on a 200-nm-pored PCTE support. Subsequent etching by potassium permanganate can

create pores with an average value of 0.16 nm as analyzed by HRTEM with a small fraction of pores larger than the water van-der-Waals diameter and rarely salt permeable pores (>0.7 nm). Osmotic pressure experiments show water transport close to theoretical prediction and of a similar order of magnitude as polymeric membranes typically applied in reverse osmosis. Solute rejection was studied with NaCl, $MgSO_4$, Allura red, and dextran showing negative rejection of NaCl (0.7 nm), rejection of 70 % $MgSO_4$ (0.8 nm), 90 % Allura red (1 nm), 83 % dextran (3.7 nm). Negative NaCl rejection is equivalent to more NaCl transport of their graphene/PCTE composite in comparison to the bare composite according to the used rejection definition. This observation, along with the lower dextran rejection despite larger size requires further study and might be related to KCl permeability of nylon.⁷⁰ Further, the role of pores too small for IP sealing and too large for ALD sealing remains unclear.

To target applications properly, achievable salt rejection as a function of the pore diameter needs to be understood. Figure 3 shows various experimental and theoretical results for various nanopores. In general, pores below 0.5 nm are found to reject salts such as NaCl, however for pores slightly larger than this size, the rejection decreases and becomes inconsistent within a pore size. While some researchers predict over 98 % rejection of ca. 0.85 nm pores, others simulate down to a mere 30 % rejection at a given pore size. Differences in chemical functionalization of the pores, but also in simulation details may cause this deviation. Furthermore, experimental demonstration of NaCl rejection using CVD graphene remains to be achieved as the only experimentally available result shows the peculiar case of negative rejection that may be related to the experimental procedure and data evaluation of that work. (see figure 3.3)

In Summary, liquid and ion transports across graphene have shown a diverse behavior in both theory and experiment that strongly varies with pore size, charge, and transporting solutes. The demonstration of selectively passing cations over anions pave the way for efficient re-

3. Status Quo of Graphene Membrane Studies

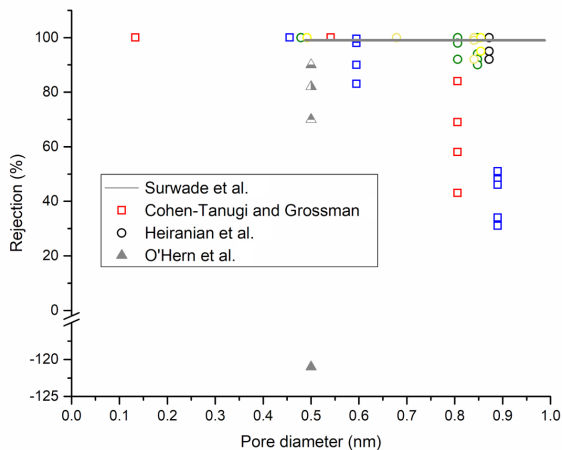


Figure 3.3: NaCl rejection of various pore size of 2D-nanopores. Unless specified differently, as function of pore diameter. Inconsistent ion rejection at a given pore size request further investigation. Symbols represent the corresponding study (line⁵⁵, square⁵⁴, circle⁵⁸, triangle⁵⁶); colours represent chemical group at the pore edge. Red, blue, black, and gray represent hydrogen, hydroxyl, no, and unknown functionalisation of graphene, respectively. Green, yellow and dark yellow represent Mo, S, or mixed pore edge atoms in MoS_2 . Partially filled triangles represent $MgSO_4$, allura red, and dextran molecules.

verse electro dialysis, and the demonstration of ion rejection is particularly important for the desalination applications. Anticipated are substantial efforts required in obtaining selective molecular flows across graphene membranes at square centimeter or larger scales, which calls for a breakthrough in the manufacturing process. On the other hand, applications that require only a micrometer-scale membrane dimension, such as DNA sequencing or chem-bio sensing, might have more readiness to market entrance.

3.4 Proton Transport

Miao et al. have used first-principles DFT simulations to study atomic hydrogen and proton transport through pristine graphene.⁷¹ Due to electron orbital overlap, repulsion forces are experienced by both hydrogen and proton. However, the energy barrier for the passage of physisorbed hydrogen is 2.46 eV compared with physisorbed protons experiencing only 1.41 eV. During the passage, the graphene hexagons expand and contract again, reflecting the strong interaction, similar to gas molecules passing through nanopores. This study demonstrates the principal possibility of hydrogen and proton passage through pristine graphene; however, the predicted energy barriers would be impractically high. On the other hand, the presence of defects such as double vacancies significantly reduces the energy barrier for passage. Experimentally, Hu et al. have investigated proton conductivity of mechanically exfoliated monocrystalline graphene, MoS_2 , $h - BN$, and multilayers of these with an applied electrical potential as the driving force.⁷² By coating different 2D crystals with NafionTM and measuring current-voltage characteristics in a humid atmosphere, they found unexpectedly high transport through graphene and $h - BN$ monolayers, while single-layer MoS_2 and bilayer graphene show no transport. The variation among proton conductivity is rationalized by variation in electron cloud density among the various materials and differences of $h - BN$ from graphene in stacking behavior; however, the fundamentals of the passage remain to be elucidated. Measuring proton conductivity at various temperatures allowed to extract the passage energy barrier that was determined to be 0.78 eV and 0.3 eV for graphene and $h - BN$ monolayers, respectively. Platinum sputter coating of the 2D crystal further decreased the passage barrier, leading to immense proton conductivity for $h - BN$. Further experiments of HCl conductivity measurements and mass spectroscopy verified the previously observed transport rates. The lower passage barrier compared with theoretical prediction requires further research.

Measuring aqueous proton transport across graphene in the absence

3. Status Quo of Graphene Membrane Studies

of an external electric field as the driving force has been reported by Achtyl et al.⁷³ Using alternating streams of acidic or basic solutions of the same strengths flowing over fused silica surface allowed them to probe protonation and deprotonation of silanol at the silica surface by the second harmonic generation technique. The measured second harmonic time trace is indistinguishable from bare fused silica compared with fused silica covered by monolayer graphene from CVD, indicating unimpeded proton transport across the graphene layer. The same holds true for up to 8 layers of graphene tested. SEM analysis shows macroscopic defects of 500 nm and larger in diameter to be widely spread such that it is unlikely to probe areas close to these defects by their 30- μm -wide laser spot. However, STEM analysis with atomic resolution reveals atomic-scale defects to be present statistically always within the laser spot. DFT simulations and ReaxFF reactive force field MD simulations are performed to predict the aqueous proton transport mechanism across graphene. They obtained 3.8 eV energy barrier for protons to pass through pristine graphene, which makes it an unlikely explanation of their experiments. However, for quadrivacancy atomic-scale defects with various pore functionalization, they find that hydroxylated pores can allow proton passage with a moderate energy barrier of 0.6 - 0.7 eV as these can form hydrogen bonds with the adjacent water layers such that protons can shuttle across the defects in a Grotthuss mechanism at room temperature. Due to the uncertainty of atomic defect density estimation, the authors state that other means of transport may yet be possible. Especially the reason for indistinguishable traces for even eight layers of graphene remains elusive.

In the same year, a second study measured proton transport across CVD graphene by covering glass capillaries with single-layer graphene and measuring current-voltage characteristics in the presence of an HCl concentration gradient.⁷⁴ Selective passage of protons over Cl^- anions is observable by a measurable net current with no voltage applied. The reversal potential, the external potential required to stop the net current, allows extracting the proton selectivity of the mem-

brane. While as-grown graphene shows only mild selectivity, depositing Al_2O_3 by ALD causes the total current across the graphene to decrease significantly, while at the same time the reversal potential, and thus the selectivity increases significantly. A reduction in total current and increase in reversal potential after ALD coating is interpreted by the authors as protons to transport through defects since the total current should be dependent on the defect size, which decreases by ALD coating and increased selectivity could be caused by the reduction in defect size, such that they become more selective toward protons compared to Cl^- .

A theoretical analysis to resolve the discrepancy of the graphene tunnelling barrier between previous MD simulation and experiments has been executed by Poltavsky et al.⁷⁵ They employed ab-initio MD Feynman-Kac path-integral simulations that treat the atomic nuclei quantum-mechanically instead of classically. For comparison, they carried out their simulation also by treating the nuclei classically and obtain similar transport barriers for proton as earlier studies. The quantum mechanical treatment of the nuclei, however, predicts a significantly lower energy barrier for thermal protons to pass through graphene (0.6 eV) and match with those determined experimentally (0.8 eV) much better than non-quantum-mechanical treatment of the nuclei. Thus, this theoretical study concludes favorably for the proton transport mechanism across pristine graphene.

Seel et al. have investigated proton and atomic hydrogen transport across pristine 2D materials, such as graphene, $h - BN$, MoS_2 , and others, by means of DFT to shed light on the question of proton transport through atomically thin 2D materials.⁷⁶ From their simulations, they find that system relaxation, that is, non-rigid 2D material atom positions is a significant factor determining the penetration barrier height. Protons passing graphene experience 1.38 eV energy barrier, while $h - BN$ only poses 0.11 eV energy barrier. Apart from slightly larger atomic bond lengths in $h - BN$ compared with graphene, the polarization of $h - BN$ is found to facilitate proton transport due to ionic bonding opportunities for protons arising during the passage.

3. Status Quo of Graphene Membrane Studies

Contrary to this result, MoS_2 is found to trap atomic hydrogen and protons in between the S-layers in a 1.56 eV-deep energy well. They investigated the effect of Pt for passage without observing different activation energy for passage. The presence of a quad-vacancy terminated by oxygen atoms reduces the passage barrier further to 1.1 eV, suggesting that experimentally observed proton transport across graphene stems from defects, while $h - BN$ allows the thermal protons passage. Zhang et al. have carried out ab-initio DFT to understand better the differences in permeance of hydrogen isotopes, as previously demonstrated by Lozada-Hidalgo et al.^{77,78} They compared graphene, $h - BN$, alpha-boron, as well as graphene with Stone-Wales (55-77) defects. Pristine graphene is predicted to have 1.5 eV passage barrier, while $h - BN$ only imposes 1 eV barrier, both in quantitative opposition to experimentally measured values. However, a ratio of hydrogen isotope separation e.g. proton/deuterium based on differences in passage barrier and Arrhenius rate constants amounts to 12, close to the experimentally obtained values. The same holds true for proton/tritium separation with predicted selectivity of 37, close to experimentally measured 30. They further probed the passage barrier of Stone-Wales defects, where specifically proton transport across heptagons is found to experience a lower energy barrier of 0.55 eV and increased proton/deuterium selectivity of 25, which is attributed to stronger interaction of protons with C-C bond connecting pentagons of the Stone-Wales defect. Furthermore, alpha-boron as a model system was investigated to yield only 0.2 eV of proton passage barrier. The differences in passage barrier to 2D materials is attributed to electron-density surfaces that reveal graphene, $h - BN$, and alpha-boron to have different effective pore sizes experienced by a passing proton, resulting in the difference in the passage barriers.

Another study extends the analysis of proton permeation across two-dimensional materials from graphene and $h - BN$ to other materials such as phosphorene or silicene.⁷⁹ In their DFT simulations, they furthermore distinguish the proton permeation barrier depending on the environment around the membrane. For vacuum, protons pass

through graphene and $h - BN$ with 1.2 eV and 0.6 eV energy barrier for adsorption with the subsequent passage. Changing the environment to aqueous solution is found to increase the proton penetration barriers to 3.3 eV and 3.0 eV for graphene and $h - BN$, respectively, such that the authors concluded proton passage to be unlikely at room-temperatures in an aqueous environment.

More effort to understand and resolve the mismatch between theoretical and experimental proton permeation barriers across graphene and $h - BN$ was done by means of DFT simulation.⁸⁰

Structural optimization of the proton-2D-crystal arrangement was found to increase the permeation barrier counterintuitively. This could be explained by the previously unstable configuration of the proton in vacuum over the 2D crystal. System relaxation leads to proton adsorption to the respective crystal lattice such that the system is in a more stable state. Other effects of mechanical strain or curvature reduce the barrier by 0.1 eV or less and thus being unable to explain the discrepancy. Further simulations of proton in aqueous phase also increases the permeation barrier to up to 5 eV for graphene in qualitative agreement with the previous study⁸⁰ of a higher barrier to solvated protons in comparison to vacuum permeation.

In a study performed by Tsetseris et al., DTF was applied to reveal details of the permeation process of atomic hydrogen, boron, nitrogen, and oxygen.⁸¹ With passage energy barriers of 4.2 eV, 5.5 eV, and 3.2 eV for hydrogen, oxygen, and nitrogen, respectively, it was confirmed that pristine graphene could be considered impermeable also for these atomic species.⁸¹ Interestingly, the passage barrier for atomic boron is only 1.3 eV. In general, three passageways for permeation of atomic species can be considered: direct passage through the center of the hexagonal rings without C-C bond breaking, adsorption, and passage involving breaking and reformation of C-C bonds, and more complex passages. Using minimum energy pathways, the authors determine all of the studied atomic species to predominantly undergo the second pathway involving breaking of C-C bonds by forming bonds with the passing atoms. Out of these, boron has a surprisingly low

3. Status Quo of Graphene Membrane Studies

energy barrier that may be overcome frequently at moderately high temperatures of around 200 °C. Experimentally, selective hydrogen isotope transport was demonstrated by means of a NafionTM coating of graphene or *h* – *BN* monolayer in a 100 % humidity atmosphere of either hydrogen-argon or deuterium-argon mixtures and then by performing current-voltage measurements and mass spectroscopy measurements.⁷⁸ The authors found out proton/deuterium selectivity of 10, which can be interpreted as 60 meV difference in passage energy barrier.

Interestingly, the selectivity is the same for graphene and for *h* – *BN*, even though the total barriers differ. This result implies intrinsic differences between protons and deuterons to cause the observed selectivity. Indeed, the differences in zero-point energy of protons bound to the oxygen of the SO₃⁻ group of NafionTM from those of deuterons matches the derived energy difference from the selectivity. This finding suggests that the difference in zero-point energy is responsible for the experimentally observed selectivity. Out of the differences in zero-point energy, a proton/tritium separation factor of 30 is expected.

In subsequent work, Lozada-Hidalgo et al. have demonstrated the electrochemical pumping approach for CVD graphene on a one-inch scale with 95 % macroscopic graphene coverage and a proton/deuteron separation factor of 8.⁸² Since graphene works as an electrode of the electrochemical pump, these macroscopic pinholes are not expected to reduce the separation factor significantly, validating the utility of the technology. The energy requirements are less than the currently best available technological option showing the highest current selectivity and may be reduced further by using *h* – *BN* and/or optimized operation conditions.

Despite these advances, the fundamental question about proton transport across pristine graphene persists, as can also be seen from Figure 4 showing the available results of the energy barrier for protons to pass graphene as a function of the number of missing carbon atoms from the lattice. An apparent mismatch between simulation and experiment can be observed. Particularly, the presence of atomic defects

with few atoms removed from the lattice is experimentally hard to rule out unambiguously.

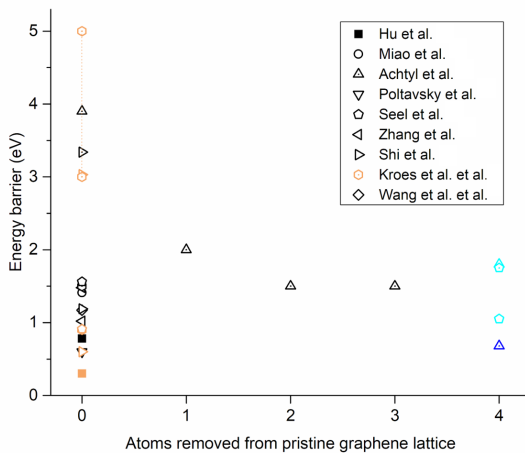


Figure 3.4: Energy barrier for proton passage across graphene and $h - BN$ for various atoms removed from the lattice. Strong variation between available data for non-porous graphene transport barrier requests for further study. Symbol shapes represent different studies (square⁷², circle⁷¹, triangle⁷³, reversed triangle⁷⁵, pentagon⁷⁶, tilted triangle⁷⁷, tilted triangle⁷⁹, hexagon⁸⁰, diamond⁸³). Filled and hollow symbols represent experimental and theoretical results respectively with black and brown representing graphene and $h - BN$ respectively. Dotted symbols represent aqueous environment. Blue and cyan represent graphene with hydroxyl and oxygen termination. Kroes et al. provide a range of the penetration barrier in between the limits shown in the graph

3.5 Discussion

Chemical species can transport across porous graphene or other two-dimensional membranes through various mechanisms depending on the phase and charge of each transporting species.

Simulations and experiments agree that pristine graphene is generally impermeable to gases, while nanometer-scale pores punctured on

3. Status Quo of Graphene Membrane Studies

graphene can provide transport pathway depending on the size comparison, physicochemical interaction, and orientation of transporting molecules with pores, on the geometry and chemical functionalization state of the pore, and the presence of non-permeating species. While the molecule-to-pore size ratio can primarily determine passage, a precise amount or rate of permeation of a gas species may be reliant on surface adsorption and diffusion or chemical affinities of the species around the pore, factors often regarded as secondary effects to porous membranes.

According to simulations, electron orbitals and the resulting electron probability density can effectively govern the interaction dimension between pore and molecule. From this finding, it is deduced that electron orbital overlap is strongly correlated with the energy barrier that molecules face in an attempt at pore passage. For a specific pore size near 1 nm (slightly beyond a molecular sieving regime), adsorption to and surface diffusion on the membrane surface are likely to dominate the gas transport mechanism. This prediction may have significant implications for membranes in practice as typical separation prediction based on molecular mass or kinetic diameter may not work for certain gas mixtures, possibly resulting in separation factors that belie those of molecular sieves, as exemplified by favorable permeation of unwanted species.

Pores in the size regime commensurate tightly with transporting molecular dimensions that are likely to separate a gas mixture via entropic gates that usher certain specifically oriented molecules. This approach may be proved useful in the separation of gas species that are close in kinetic diameter but disparate in adsorption orientation. An idealization taken in many simulations is membrane rigidity, whose insignificant influence on separation has been put into question. In this light, experimental validation of predicted phenomena can be critical to clarify our molecular-level understanding of gas transport and separation across porous 2D materials. Similarly, no experiment until today could reveal disparity in separation correlated to functional groups at the pore edge and their charge state. For molecules of very

similar kinetic diameters, the clear disparity in molecular interaction with pore-functional moieties promises to allow meaningful separation of an almost inseparable mixture with conventional membranes, such as N_2 from O_2 .

Experimentally, hermeticity and molecular-sieving-like large separation factors ($>10^4$ for a particular gas mixture) of mechanically exfoliated graphene have been established. Transport across exfoliated graphene with few pores is found time-variant originating possibly from dynamic switching of bond state of edge atoms of subnanometric pores.

Flow physics of large-area CVD-grown graphene does not follow continuum-mechanics-based channel-flow models such as Hagen-Poiseuille flow but instead complies with Sampson's formula, a solution of a low-Reynolds-number flow across a 2D disc, where resistance to flow comes exclusively from a pore entry event. For the same reason, no Knudsen minimum in the permeance is observed at Knudsen numbers near unity.

Regarding gas separation, a critical role of defects in graphene has been verified. Molecular sieving across defective graphene with subnanometric pores has been characterized in a single-gas permeance measurement followed by estimation of permselectivity. However, real applications demand sieving of gas mixtures, calling for methods to generate subnanometric defects in a facile, controllable, and scalable manner, with maintaining the ultimate permeance promise of graphene.

In order to apply the graphene- or 2D material based membranes to gas separation applications, there are a number of physical effects and technological aspects to take into account. Demonstration of gas mixture sieving across CVD graphene membranes perforated with scalable processes needs to be achieved to move CVD graphene membranes from laboratory to industry for applications such as air separation, CO_2 sequestration or other technologically relevant gas separations. Physical effects of charge and chemical functionalization of a pore remain to be investigated, and the predicted blockage of non-permeating species in ternary mixtures define both a scientifically interesting ques-

3. Status Quo of Graphene Membrane Studies

tion – for the exploration of new means of separation – and a practically important task if considering a fact that most gas separation applications deal with complex mixtures beyond binary one.

Regarding system design, both ultrahigh selectivity and permeance of membranes may at some point add negligible performance improvement to an entire gas separation system owing to such external effects as concentration polarization, retentate recycling limitations, and others. With 2D membranes offering ultimate permeation, it may be possible to reach the technologically meaningful limit of permeance. Given a proper way of producing large membranes with subnanometric pores, the same may hold true for selectivity. Then, these membranes can be considered as the ultimate membranes, since further permeance or selectivity improvement of the membrane may not necessarily lead to deterministic system improvements; an ultimately permeable separation membrane is not the limiting factor anymore.

Regarding liquid transport, Sampson's formula governs the transport across a 2D aperture as long as continuum fluid can be assumed around the 2D aperture, although frequently, the Hagen-Poiseuille formalism is misused for subnanometric pores because both theories lead to comparable predictions for channels with pores of aspect ratio close to unity. Variation of permeance for different 2D material such as MoS_2 has been theoretically predicted, though experimental confirmation is absent.

Pore-sizes below the limit of continuum assumption has been predicted to exemplify sub-continuum variation in fluid properties such as density, viscosity, or diffusivities for which experimental proof is still missing. Vapour transport studies across nanopores have so far been limited; however, interesting questions about fluid properties during phase change and vapor interaction with graphene or other 2D materials can be thought of due to similar experimental observations in neighboring fields.⁸⁴ The understanding of flow enhancement for CNT's and nanofluidic channels may be broadened by considering transport across 2D nanopores that are at the limit of thinness and could present an idealized system of the former fields.

Even though graphene has been proven as mechanically sturdy under applied pressure as simulation and previous mechanical characterization predicted, how the mechanical properties will alter if graphene is perforated remains a question.^{9,85} For use in practical applications, it will be necessary to probe the limits of mechanical strengths for various pore sizes, density, and other membrane parameters as has been predicted theoretically.⁸⁶

Ionic transport has been investigated rather thoroughly and theoretically where the conductance of 2D nanopores decreases strongly at the continuum-limit, due to non-continuum effects such as variation in ion mobility, concentration, or dehydration barriers for passage. Nanopores with different functional groups exhibit a strong ion-selective behavior and a possible inter-co-ion selectivity depending on interaction strengths with charged groups at the pore edge. For sufficiently small pores, desalination by reverse osmosis is predicted and experimentally shown using forward osmosis. Similar to pure liquid transport, distinct effects of the choice of 2D materials is predicted, although experimental proof is lacking. Experimentally shown, however, have been various ionic conductance phenomena of subnanometric pores such as Coulomb blockade or conductance similar to biological channels.

At large pore sizes, linear scaling of conductance with pore diameter is most accurate due to the 2D geometry of the pore. This scaling is in line with the liquid transport where the transport rate shows linear dependency on the pore size (e.g., Sampson's formula), in contrast to three-dimensional descriptions. Besides, molecular sieving using centimeter-sized graphene as well as nanofiltration of charged species is established.

The effect of surface charge has been proposed as a significant means for selective ion transport even in pores much larger than a Debye screening length, raising a question of how to tailor the surface- and pore charge in order to engineer ionic transport for various pore sizes. Variation in surface charge by voltage gating may offer a pathway to achieve ion selectivity for pores larger than the hydrated diameters of

3. Status Quo of Graphene Membrane Studies

the solutes to be rejected. For desalination applications, salt rejection by CVD grown graphene perforated with scalable processes remains to be demonstrated in order to position graphene as a potential candidate for future desalination membranes. Proton transport as a special case of ionic transport due to differences in the atomic configuration in solution has been experimentally shown and theoretically analyzed. However, the exact mechanism of transport remains disputed with some studies suggesting proton transport through pristine parts of graphene or $h - BN$, while others suggest defects to be the cause of the proton transport pathway. Here, more work is required to resolve the current issues and to enhance our understanding.

As an overarching goal, 2D membranes should be manufactured at length scales relevant to the respective application, which often involves square meters or even larger than that. To this end, synthesis and fabrication methods to yield nearly defect-free membranes need to be established. One of the most important operational challenges in membrane separation processes is clogging and fouling of the membrane surface such that the separation performance of the membrane deteriorates over time. 2D membranes might offer a unique advantage of reducing clogging and fouling exclusively to its surface compared with channel clogging and fouling in conventional membranes. Surface cleaning should be much less challenging, and thus 2D membranes may prove themselves to be practically beneficial for a long lifetime under chemically harsh conditions.

Chapter 4

Liquid transport at the Limit of Atomic Thinness

This section is published in parts as:

Jakob Buchheim, Karl-Philipp Schlichting, Roman M. Wyss, and Hyung Gyu Park. “*Assessing the Thickness-Permeation Paradigm in Nanoporous Membranes*” *ACS Nano*, **2018**, 13(1), 134-142
DOI:<https://doi.org/10.1021/acsnano.8b04875>

Jakob Buchheim and Karl-Philipp Schlichting contributed equally. Karl-Philipp Schlichting developed the experimental setup, performed the control experiments, membrane fabrication, found the membrane fouling model, and did ALD cross-sectional analyses.

Mass transport across nanometer-sized pores is of fundamental interest to many disciplines such as biology, medicine, physics, and engineering.^{87–89} Nanopore-based separation and filtration have seen a surge in membrane technology research due to the vast potential to reduce energy requirements over conventional technologies and to an impli-

4. *Liquid transport at the Limit of Atomic Thinness*

cation of a significantly decreased facility footprint.¹

Permeation through porous membranes is often limited by frictional losses related to molecule-wall interactions. Minimizing the energy requirement for permeation can, therefore, be achieved by reducing the thickness and lowering the transport resistance associated with it.⁴ Consequently, the use of thinner membranes is a core of current membrane research with permeation conventionally understood to be inversely proportional to thickness.^{4,90} Then, an ideal porous membrane is supposed to have a negligible thickness.

The discovery of mechanically stable 2D crystals like graphene has immediately triggered computational simulation for ion,¹³ water,¹² and gas transport¹⁴ through such ultimately thin membranes. Researchers have predicted that nanoporous 2D materials, such as porous graphene, pose unique flow physics for gases and liquids. Originated from the infinitesimal thickness, the ultimate permeation of gases and liquids could be observed, rendering 2D membranes as a potentially efficient membrane material for filtration and separation.⁴⁵ Various membrane architectures that employ porous graphene are conceived for fields such as desalination, ultrafiltration, and membrane distillation.^{54–56,68,91}

Infinitesimal thickness, however, comes at the expense of in-operando mechanical stress and susceptibility for defects, altogether impairing the membrane performance.^{70,92} Indeed, independent stacking of graphene layers has been shown to exponentially decrease defective areas of membranes, giving strong motivation to increase the membrane thickness.⁴¹ Thus, a trade-off emerges such that optimizing overall membrane performance requires a detailed understanding of the governing transport mechanisms of membranes of various thicknesses. As the membrane thins down to nearly a 2D layer, the inverse proportionality between mass flux and thickness is prone to breaking down because of a shift in the transport mechanism. The comprehensive understanding of this channel-to-orifice transition has so far been hampered by a lack of a well-controllable characterization system.

Characterization of liquid permeation across single nanopores requires

the determination of flow rates that are undetectable using conventional flow meters, and state-of-the-art flow measurement approaches conversely involve significant experimental efforts and sophistication.⁹³ Therefore, typical permeation studies today employ a method of simultaneous permeation across a multitude of pores, which often invoke significant uncertainties in pore number and pore size distributions.^{56,69} To overcome these uncertainties, a direct perforation technique such as focused ion beam (FIB) milling has proven itself to be instrumental by demonstrating well-defined pore geometries and pore numbers.⁴⁵

We manufacture nano-to-microporous graphene membranes (PGMs) by FIB with narrow pore size distributions and precisely defined pore numbers. This well-controlled system enables the characterization of pressurized flows of liquids of various viscosities through pores with diameters spanning almost three orders of magnitude from sub-10 nm up to 1000 nm. Permeation is found to be limited by entrance resistance stemming from viscous dissipation within the fluid near the pore entrance. This resistance needs to be overcome by any porous structure and thus provides an upper bound to permeation.

To gradually adjust the thickness of the atomically thin PGMs, we employ atomic layer deposition (ALD). Obtained thickness variation from sub-1 to 90 nm allows the investigation of the transition from orifice to channel transport. Understanding this transition enables us to identify an ideal permeation thickness for a given pore size, thereby facilitating reduced defects and enhanced mechanical stability. Furthermore, the permeation upper bound can be utilized as a benchmark for comparing various porous materials for their potential as fast transporting membrane materials, before optimizing other parameters such as porosity or support structures.

4.1 Graphene Membrane Manufacturing

Graphene Transfer

Porous graphene membranes are prepared by transferring two single-layer graphene samples synthesized by chemical vapor deposition (CVD) onto a custom-made silicon nitride (Si_3N_4) frame (**Figure 4.1**).⁴⁵ In brief, single-layer graphene is synthesized using low-pressure chemical vapor deposition (LPCVD) on 25 μm copper (Cu) foil (ALPHA AESAR 13382). A thin-film poly(methyl methacrylate) (PMMA) (50 k, Allresist Inc.) protective layer is spin-coated on the graphene/Cu composite, after which it is floating-etched in ammonium persulfate solution (0.5 M, Sigma-Aldrich) to remove the Cu foil. After rinsing in DI water, the PMMA/graphene composite is fished out by another graphene/Cu composite such that a DLG sandwiched between PMMA and Cu foil results. After repeated Cu foil etching, the PMMA/DLG composite is fished out by custom-made silicon nitride (Si_3N_4) chips, having defined arrays of 4 μm diameter holes of 150 nm thick Si_3N_4 membranes. Thermal annealing at 400 °C using 900 sccm H_2 and 100 sccm Ar is applied to remove the PMMA protective layer.

Serial Pore Fabrication

Double-layer graphene (DLG) is perforated by applying FIB milling using 30 kV and 1.1 pA to create circular pores with precisely defined diameters between 6.2 ± 1.1 nm and 1020 ± 2 nm with pore numbers ranging between 10 and 10^6 and areal porosities between 0.1 % and 10 % on a graphene area of $\approx 1000 \mu\text{m}^2$ (**Figure 4.2**).

4.1. Graphene Membrane Manufacturing

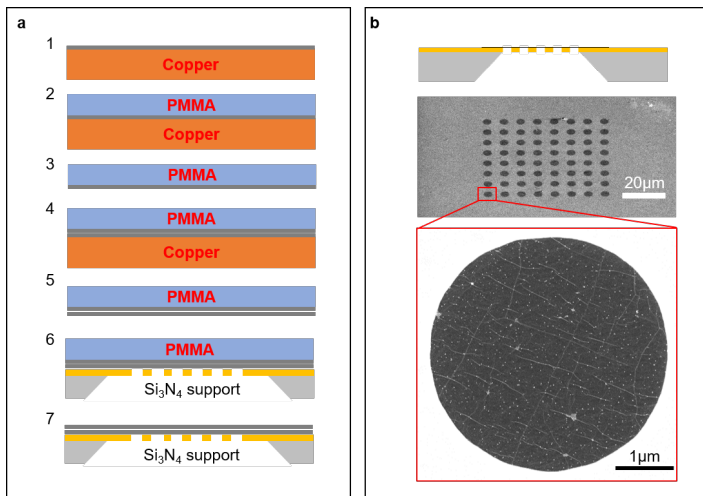


Figure 4.1: **a** Membrane manufacturing processes starting from single layer CVD graphene on Cu foil (1), spin coating a protective polymeric layer for transfer (2), etching Cu (3), adding a second single layer CVD graphene on Cu below the PMMA/SLG composite to obtain DLG (4), repeated Cu etching (5), followed by transfer to the porous silicon nitride chip (6), and thermal removal of the polymer layer (7). **b** Successfully transferred graphene on silicon nitride frame with tilted-view SEM images of the porous array and a high magnification image of one frame hole showing the freestanding graphene membrane.

Membrane Characterization

The total graphene membrane areas are small enough to allow SEM imaging of the entire graphene membrane area with down to 5 nm resolution to detect any defects. This approach enables the detection of possible leakage pathways from pinholes and ruptures in the graphene membrane. We occasionally used platinum deposition prior to permeation experiments to seal individual defects.

Pore sizes were measured by extracting the open area of multiple pores from SEM micrographs (**Figure 4.3**). Typically, ≈ 4 pixel/nm resolution was chosen. The extracted area is then converted into an equivalent diameter of a circle. The pore sizes obtained from direct FIB drilling show very narrow distributions such that the mean pore

4. Liquid transport at the Limit of Atomic Thinness

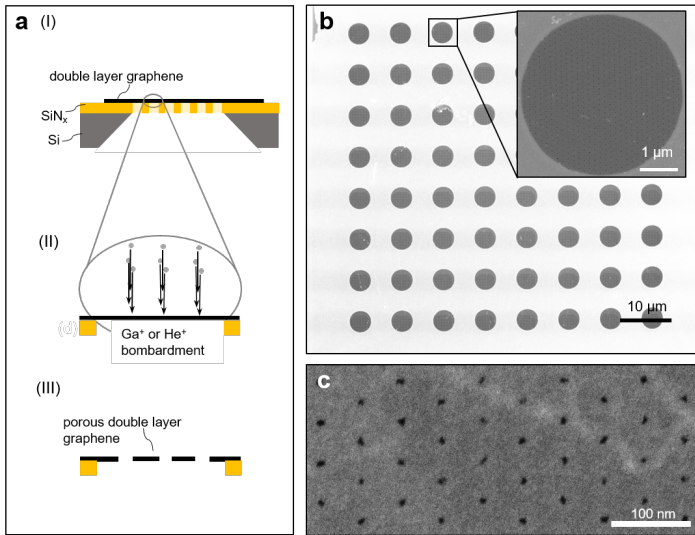


Figure 4.2: **a** Freestanding DLG (I) is exposed to energetic ion irradiation (II) to create a porous membrane (III). **b** Exemplary SEM image of patterned graphene nanopore arrays of the full membrane area. Zoom-in image of an individual silicon nitride hole covered by porous graphene. **c** High-magnification SEM image of the smallest achieved nanopores in graphene with circular pores evenly spaced.

size obtained from SEM micrograph analysis may be directly related to the mass transport. This well-controllable method prohibits any trans-PGM transport pathways other than those artificially created by FIB.

One may suggest weighting the pore size distribution by the diameter cubed, as permeation follows this scaling. In such a way, the pore size would represent an equivalent pore size that a membrane with uniform pore size and same pore number as the considered membrane would have (Table 4.1). Other works have shown routes on how to account for distributions' effects on mass permeation across pores.¹ The effect of pore size distribution is largest for the smallest pores, as the standard deviation of the distribution becomes comparatively larger for smaller pores. The permeation predictions for a weighted

4.1. Graphene Membrane Manufacturing

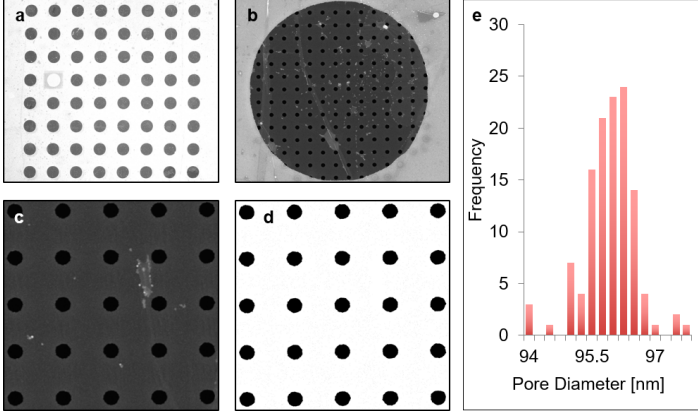


Figure 4.3: **a** Exemplary membrane with one hole sealed by platinum deposition. **b** Hole patterned with ≈ 100 nm pores. **c** High-magnification image for pore size quantification. **d** ImageJ binarized image using thresholding. **e** Resulting pore size distribution of the membrane.

diameter equivalent $Q(d_{avg}^3)$ and by accounting for distribution effects (DE), $Q(DE)$, show negligible differences compared to the permeation prediction based on the average pore size, Q_{avg} . This comparison validates using the average pore size directly without further need of modeling.

Table 4.1: Pore size bounds for membranes used in this chapter with measured corresponding standard deviations, σ . The flow rate predictions for, both, the largest and the smallest pore sizes with measured standard deviations differ only minorly. Therefore, a simple average of the pore size determination is sufficient to attribute to the flow measurements.

d_{avg} [nm]	1019.5	8.5	6.1
σ [nm]	1.8	1.3	0.9
$Q(d_{avg})$ [10^{-23} m ³ /s/Pa]	4.65×10^6	2.72	1.01
$Q(d_{avg}^3)$ [10^{-23} m ³ /s/Pa]	4.65×10^6	2.89	1.07
$Q(DE)$ [10^{-23} m ³ /s/Pa]	4.65×10^6	2.73	0.98

The well-controlled and narrow distributions of pore diameter enabled in this manner lead to the precise determination of the mass transport

4. Liquid transport at the Limit of Atomic Thinness

across freestanding PGM of a given pore size.

Membrane Permeation Preparation

After graphene synthesis, transfer and patterning, and SEM characterization, membrane fabrication is complete. However, we experienced sheared-off membranes from the support after measurement (**Figure 4.4 a**). The membrane lifts off the support structure, exposing the bare Si_3N_4 holes or graphene from the vicinity is washed onto the membrane area covering the drilled pores in the graphene membrane. To overcome the shear-off, we employed directed platinum deposition using FIB resulting in attachment of the graphene membrane to the support when immersed in liquid (**Figure 4.4 b**). First, graphene that surrounds the membrane area can be removed by sputtering a high dose of Ga^+ ions onto the vicinity (orange shading (**Figure 4.4 b**) of the freestanding graphene, which removes graphene as well as contamination outside the active graphene membrane. Next, to ensure the integration between perforated graphene and the holey support, additional deposition of material (*e.g.*, Pt) around the active membrane area is applied to stitch the graphene onto the support, thereby successfully preventing the membrane disintegration caused by the graphene being washed off the support structure on all samples tested.

In addition to ion dose sputtering around the active membrane area, the support chip is macroscopically cleaned by swiping the surrounding of the graphene membrane area using acetone drenched wipes. The setup is cleaned prior to permeation measurements. The fixture and tubing are rinsed three times using IPA with subsequent distilled DI-water rinsing followed by nitrogen gun drying.

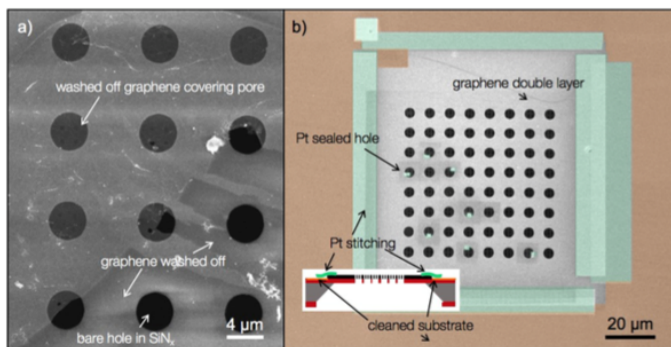


Figure 4.4: Need of Pt stitching. **a** Post-flow analysis of a graphene membrane reveals a partially washed off graphene membrane **b** Colorized SEM image of a graphene membrane, stitched with Pt deposition (green) to the supporting frame (gold) and locally Pt-sealed ruptures in the graphene membranes. Inset shows a crosssectional schematic. The support frame is cleaned using 30 kV Ga^+ ion irradiation to clean the surface. This Figure is also shown in Jakob Buchheims dissertation⁹⁴

4.2 Liquid Permeation Measurements

4.2.1 Experimental Setup

In order to precisely quantify the permeation, a custom-build setup was developed (**Figure 4.5a**). Liquid permeation was measured in a through-flow mode. The membrane carrying the Si_3N_4 chip is clamped with O-rings in a custom-built fixture. The feed side of the membrane is connected to a liquid reservoir and a pressure port. The permeate side of the Si_3N_4 support is mounted to a nanoport (IDEX Health & Science LLC) transparent tubing to prevent leakage.

Upon application of pressure to the feed liquid reservoir using compressed nitrogen, water permeation is observed by tracking the position of the water/air interface within the permeate side tubing using a camera (Canon EOS 750D) (**Figure 4.5b**). Deionized water was obtained from Millipore (Merck) and subsequently distilled to increase purity and reduce contamination. Ethylene glycol, ethanol, and di-

4. Liquid transport at the Limit of Atomic Thinness

ethylene glycol were purchased from Sigma-Aldrich and used without further purification.

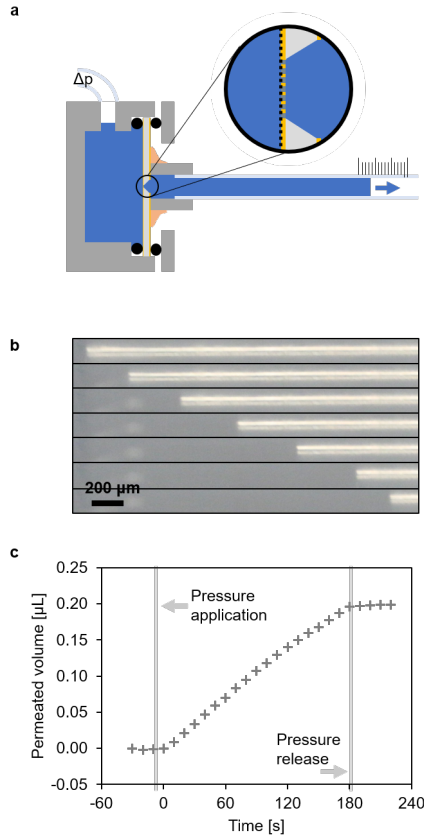


Figure 4.5: Measurement principle, raw data, and evaluation. **a** Custom-build through-flow permeation setup with pressurized water passing across the supported graphene membranes and change in permeate meniscus position allows observation of the transport. **b** Experimental observation of permeation over time display the water-air interface to move along the permeate tubing over time. **c** Quantitative evaluation of permeated volume over permeation time, where the slope indicates the flow rate.

After establishing that the precise manufacturing of nanopore arrays and their quantification allows a description of flow for a single pore

4.2. Liquid Permeation Measurements

size, several uncertainties regarding flow measurement need to be analyzed individually.

While the total volume displaced as a function of time is measured, the permeation across the graphene nanopores can only be precisely quantified if all the volume movement across the nanopores can be attributed to the pores. Furthermore, it must be confirmed that the graphene nanopores are the largest resistance to flow, such that the externally applied pressure drop can be safely assumed to occur directly at the membrane. To test this, we compared the measured volume displacement rates of various graphene membranes with the volume displacement rate for only the silicon nitride frame (**Figure 4.6**). Permeation experiments using the silicon nitride support structure show per-pore-permeation on the order of $1 \times 10^{-15} \text{ m}^3/\text{s}/\text{Pa}$ across the $4 \mu\text{m}$ holes (**Figure 4.6a**).

To account for the fact that most of the membranes have multiple graphene nanopores in the freestanding graphene membrane, we computed the ratio of the flow resistance of the graphene measurements to that of the support frame (**Figure 4.6b**) for exemplary samples with pore sizes spanning all orders of magnitude studied. Based on the series resistance representation of transport

$$R_{total} = R_{graphene} + R_{support} \quad (4.1)$$

The graphene membrane resistance is approximated as

$$R_{graphene} = R_{total} \left(1 - \frac{R_{support}}{R_{total}}\right) \approx R_{total} \quad (4.2)$$

For all membranes measured, the support resistance stayed below 1.5% of the total resistance, such that all pressure drop effectively occurs across the graphene membranes (**Figure 4.6 b**).

4. Liquid transport at the Limit of Atomic Thinness

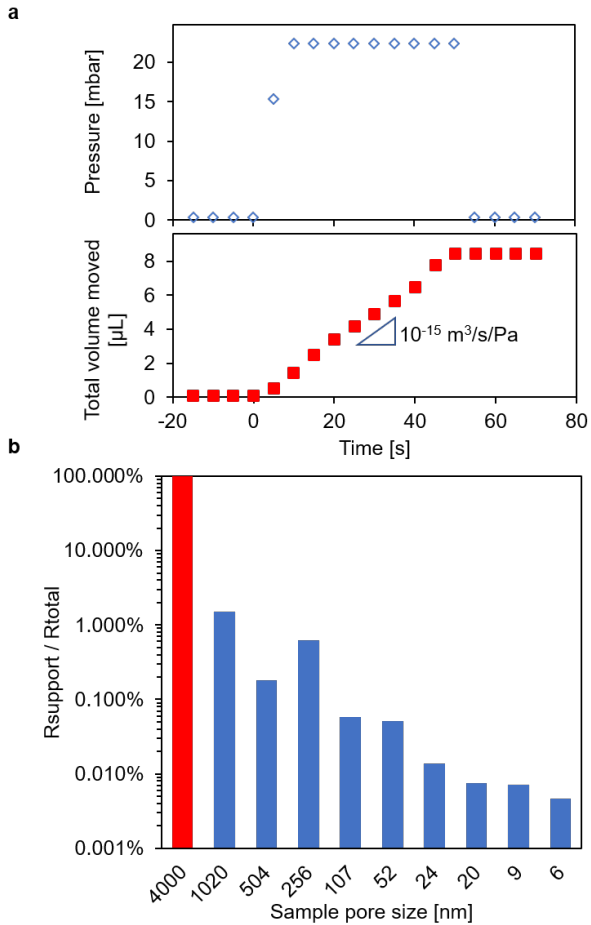


Figure 4.6: Positive control experiments and quantification. **a** Pressure as function of time together with the corresponding permeated volume as function of time for a $4 \mu\text{m}$ control experiment consisting of the support structure alone. Permeation of $1 \times 10^{-15} \text{ m}^3/\text{s}/\text{Pa}$ is almost two orders higher than for a typical measurement. **b** Permeation resistance of the support structure compared to the total resistance for various measured membranes. Red shows the support structure alone. Blue show the contribution of support to total resistance for typical membranes. Typically, the contribution is around 1 % or lower.

4.2. Liquid Permeation Measurements

Next, as a negative control, a non-porous graphene membrane was mounted into the setup to test for potential volume displacement due to graphene bending, but also silicon nitride frame bending (**Figure 4.7**).

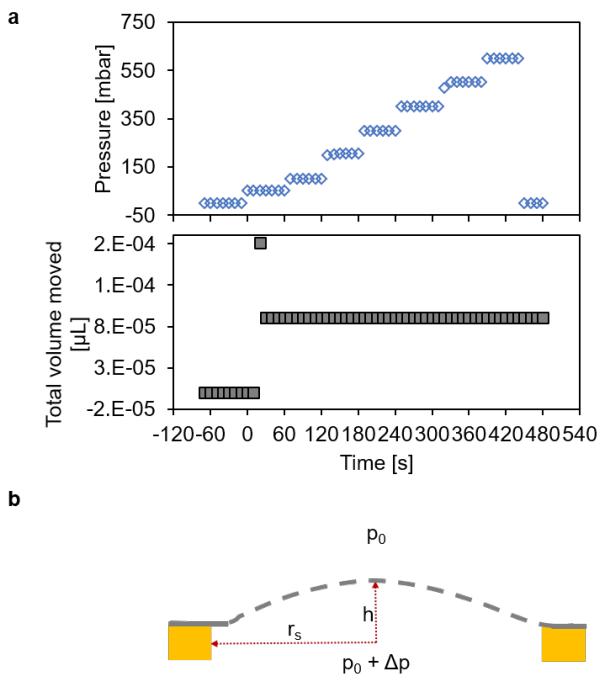


Figure 4.7: Negative control experiments and quantification. **a** Control experiment using unpatterned DLG membrane. Pressure as function of time and corresponding water movement as function of time. No permeation can be measured, even for 600 mbar of applied pressure. **b** Schematic of a porous graphene membrane that bulges with maximum displacement, h , due to an effective pressure drop, Δp , across it.

Thus, the system and Si_3N_4 support frame is designed in such a way that the pressure drop occurs almost exclusively across the graphene membranes, and leakage is negligible down to the experimental resolution limit of 13 pL/s.

Without external pressure forcing across the membrane, no move-

4. Liquid transport at the Limit of Atomic Thinness

ment of the liquid meniscus in the capillary is detected, confirming the measured permeation to stem from the externally applied pressure (**Figure 4.7a, 4.5c**).

The system was designed such that the pressure-drop across components other than the graphene is negligible.

Resolution Limit and Negative Controls

The accuracy of the liquid flow measurement depends on the precision of determining the liquid meniscus position inside the capillary tubing. The meniscus position is given by the resolution of the digital image and is usually adjusted to $\lambda_p = 1175$ pixel/mm. Using the inner cross-section area of the capillary ($A_{ca} = 0.051 \text{ mm}^2$) one can estimate the minimal detectable volume change to be 130 pL corresponding to 13 pL/s for image acquisition every 10 s for a typical experiment. We chose pore numbers high enough to resolve all permeation accurately to quantify the water permeation for all pore sizes considered.

A liquid meniscus movement due to evaporation of the water from the upstream meniscus could not be observed. The latter can be estimated by $dQ/dt = D_{H_2O}/R/T \times M_{H_2O}/\rho_{H_2O} \times P_{sat}/L \times A_{ca}$ which equals to ≈ 0.3 pL/s at 25 °C using $D_{H_2O} = 0.242 \text{ cm}^2\text{s}^{-1}$, $P_{sat} = 3.2$ kPA and a capillary length $L = 0.3$ m. The evaporation is far below the detectable range.

To ensure all measured meniscus movement to stem from permeation across the FIB drilled pores, we performed control experiments using a non-porous graphene membrane. We measured the change of meniscus position over time for various pressures (**Figure 4.7**). Within the resolution of our camera, we could not detect any movement of the meniscus for pressures up to 600 mbar. No permeation experiments were carried out above this pressure.

Consequently, possible bending of graphene or SiN_x frame lies below the detection limit of our experiment. As confirmed by the positive control experiments, the external pressure drop is held only by the

4.2. Liquid Permeation Measurements

porous double layer of graphene such that the membrane has to withstand the associated mechanical stress. The total force F_p , which is applied to the graphene during such an experiment, can be calculated by a force balance eq. 4.3 of the pressure force acting on the freestanding graphene area.

$$F = \pi r^2 \Delta p \quad (4.3)$$

Using two bar pressure difference, a pressure well above the used experimental ones, and the respective hole radius, r , of the support structure opening one yield $F \approx 2.5 \times 10^{-6}$ N for the $2r_s = 4 \mu\text{m}$ support holes.

One can calculate the amount of elastic deformation of the double-layer graphene membrane by use of the membrane shell theory (**Figure 4.7 b**). The basic assumption is that the membrane structure cannot support any bending moment. This assumption leads to a very simple situation where the thin membrane is loaded by only in-plane stresses, which are constant over the cross-section of the structure.

The bulging (deflection h from the flat membrane) caused by a uniform pressure load on the membrane can be calculated by (assuming $t_g \ll r_s$ and $h \ll r_s$):

$$h = \left(\frac{3(1 - \nu)\Delta p r^4}{8Et_g} \right)^{1/3} \quad (4.4)$$

where Δp is the applied pressure, r_s the membrane radius, Et_g the two-dimensional (2D) elastic modulus with t_g being the membrane thickness, and ν the Poisson ratio of graphene, respectively.² Inserting typical values for the double layer of polycrystalline CVD graphene

4. Liquid transport at the Limit of Atomic Thinness

($Et_g = 2 \times 10^{55} \text{ Nm}^{-3}$, $\nu = 0.3$, $\Delta p = 60 \text{ kPa}$, $r_s = 2 \mu\text{m}$) a maximal deflection $h \approx 91 \text{ nm}$ (the maximum differential pressure applied for the negative control experiments). This estimation leads to a volume displacement well below the detection limit ($O(10^{-3})\text{pL}$). This calculated deflection is slightly higher than the deflection of single-crystalline graphene monolayer flakes measured at low pressures by AFM¹¹, attributable to the lower Young's modulus of poly-crystalline CVD graphene.⁹⁵

Note that the patterned pores can further weaken the elastic response of the graphene membrane. This effect can be easily accounted for by including the notion of membrane porosity, κ , with which to decrease the 2D elastic modulus: $Et_g(\text{porous}) = (1 - \kappa)Et_g$. The graphene membranes reported here have a typical areal porosity of 0.1% to 10%, and therefore the changes of the elastic modulus would be minor.

4.2.2 Nonlinear Permeation

Despite the significant reduction of the contamination level during the water permeation measurement, still, the graphene membranes tested exhibit nonlinear flow rate even in the course of a few minutes of permeation measurement (**Figure 4.8**). Calculating the initial flow rate $Q_0 = dV/dt$ during the first minute after applying the feed pressure of 253 mbar of a membrane of 100.1 nm wide pores (porous graphene membrane coated with additional 40 ALD cycles of TiO_2), one obtains $Q = 0.589 \mu\text{Lmin}^{-1}$. After 20 min of permeation the final flow rate Q_f reduced to $0.0214 \mu\text{Lmin}^{-1}$ which corresponds to only $Q_f/Q_0 \approx 3.6\%$ of permeance left (**Figure 4.9 a**).

4.2. Liquid Permeation Measurements

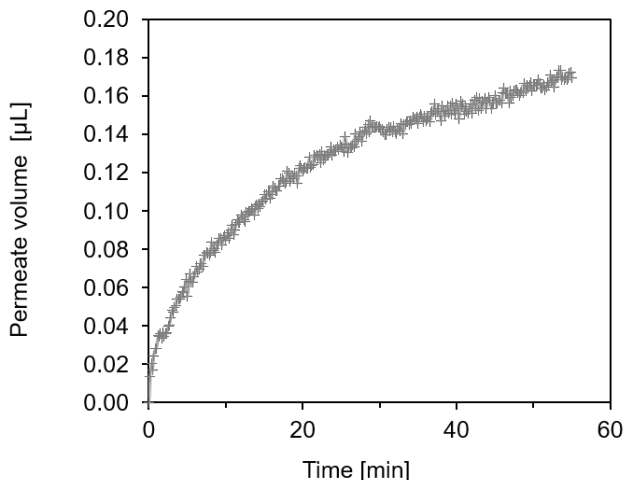


Figure 4.8: Typical, nonlinear permeation curve. Over time the rate of permeation decreases as exemplified by sublinear volume displacement over time. Transport across the membrane becomes slower.

4.2.3 Post Flow Membrane Evaluation

After drying, SEM micrographs show that the active membrane surface is partly covered by particles and other contaminants that block the pores of the graphene membrane (**Figure 4.9**). Interestingly the permeance loss agrees well with the pore area reduction experienced by the graphene membrane. Comparing the open pore area, A_{m_f} , after the water permeation experiment (highlighted red area (**Figure 4.9**)) to the area, A_{m_i} , before the experiment (highlighted red area (**Figure 4.9 b**)) one finds a similar reduction of the open pore area: $A_{m_f}/A_{m_i} \approx 7\%$. This agreement indicates that the nonlinear permeation behavior of water through the graphene membrane is a result of the loss in the permeable area due to the physical fouling of the membrane, which hampers the determination of the intrinsic (or initial) permeation performance of the graphene membrane. We also observe fouling of membranes after drying despite showing linear permeation

4. Liquid transport at the Limit of Atomic Thinness

during the experiment, which we attribute to post-flow fouling during the drying process.

Most of the liquid permeation experiments do not show linear permeation but display a sublinear behavior with a decreasing flow rate over time at constant pressure (**Figure 4.8**). Scanning electron micrographs (SEM) of the pore area of the membranes after the permeation experiment show significant contamination of the membrane surface and display blocked pores (**Figure 4.9**). Therefore, we attribute the flow rate decrease to a change of the active membrane area (total open pore area) caused by fouling during the through-flow permeation experiments. The fact that fouling never stopped despite using de-ionized (DI) water and cleansing the setup thoroughly suggests that the source of contamination lies at the graphene membrane surface and trace contaminants within our fluid system.

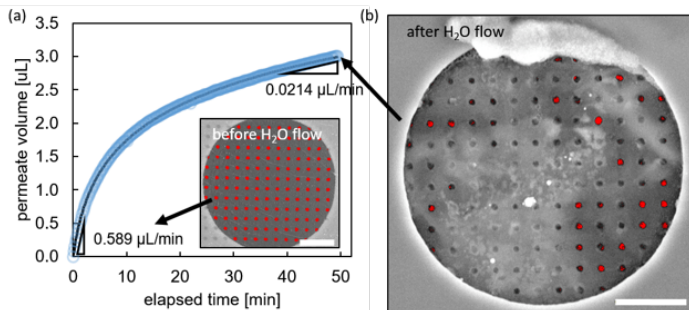


Figure 4.9: Membrane fouling leads to permeance decay. **a** A 20 min permeation experiment of water across 100 nm graphene pores shows a gradual reduction in flow rate (slope of aw data (blue circles)), with the fouling model (solid line) accurately capturing the behavior. The inset shows the ImageJ analysis of the membrane before flow, with red circles showing the open graphene pores. **b** After the flow experiment, the same graphene membrane shows a contaminated surface with most of the pores covered with adsorbates and only little remaining open pore area (red). The ratio of initial to final flow rate corresponds to the ratio of initial open area to post-flow open pore area. This Figure is also shown in the dissertation of Jakob Buchheim.⁹⁴

Fouling Modeling

Fouling is an omnipresent phenomenon in membrane technology due to the blocking of transmembrane pathways by contamination. As atomically thin graphene pores have no internal wall, all the fouling would occur on the membrane surface. We thus hypothesize the intermediate fouling model to describe the fouling behavior:

$$V(t) = \frac{A_0}{kc_c} \ln(1 + k_c j \Delta p t) \quad (4.5)$$

with the total permeated volume, $V(t)$; the initial membrane area, A_0 ; the contaminant characteristic surface area per mol, k ; the contaminant molar concentration, c_c ; the intrinsic membrane permeance, j ; pressure drop, Δp ; and the duration of permeation, t .^{96,97}

Based on graphene's geometry of negligible internal pore walls, the intermediate fouling model is considered. It assumes the graphene membrane to only foul at the surface. Two assumptions of the intermediate fouling model lead to a precise description of membrane permeation loss.^{4,90} The assumptions are: first - the feed water contains a constant concentration, c_c , of contaminants; and second - the membrane incremental areal reduction is proportional to the incremental amount of contaminants washed towards the membrane that may either block a fraction of the membrane or settle on top of previous contamination and thus not contribute to further fouling. The areal reduction stems from the probability of a contaminant to settle on an unfouled fraction. Opposed to the complete fouling model, this deposition is random with respect to the entire membrane area, fouled or unfouled. Therefore, the reduced membrane area reduction is given by the ratio of the current membrane area over the initial unfouled membrane area. The time-dependent flow rate $Q(t) = A(t)j\Delta p$ can be derived.

The incremental change of area in a finite time interval is described

4. Liquid transport at the Limit of Atomic Thinness

by

$$\Delta A = kc_c V(t) \Delta t \quad (4.6)$$

Random deposition on the entire membrane surface is mathematically expressed as

$$A(t + \Delta t) = A(t) - \Delta A(A(t)/A_0) \quad (4.7)$$

This yields the time-dependent area

$$dA/dt = -\frac{kc_c j \Delta p}{A_0} A(t)^2 \quad (4.8)$$

Which can be solved, inserted into the flow rate equation, and integrated once more to obtain the prediction of permeated volume over time

$$V(t) = \frac{A_0}{kc_c} \ln(1 + kc_c j \Delta p t) \quad (4.9)$$

Where $V(t)$ the permeated volume, A_0 the initial pore size, k area per mol contaminant, c_c molar concentration of the contaminant, j the membrane permeance, Δp the applied pressure, and t the time since onset of pressure. From this analysis, it follows that the flow rate at time t normalized by the initial flow rate is equal to the open area at time t normalized by the initial open area

4.2. Liquid Permeation Measurements

$$\frac{Q(t)}{Q_0} = \frac{A(t)}{A_0} = \frac{1}{1 + kc_cj\Delta pt} \quad (4.10)$$

Obtaining k and c_c from the model fit, it is possible to predict the time when the initial flow rate has decreased to a certain threshold value. We define the membrane half-life as the time when the flow rate is reduced to 50 % of its initial value (**Figure 4.10**).

Comparison of the residual errors from model fits among the intermediate, standard, and complete fouling models confirm the intermediate fouling model to be superior (**Figure 4.10 b**). Another possibility to compare the applicability of the different models is to compare their ability to predict the temporal permeation behavior when fitting merely one part of the measurement to the model, such that the remainder is a model prediction of permeation, based on the initial permeation fit. The intermediate fouling model clearly can most accurately predict the permeation for different times of initial fitting compared to the standard fouling or the complete fouling models (**Figure 4.10 a**).

Indeed, the intermediate fouling model precisely fits and predicts the time evolution of water permeation across porous graphene (**Figure 4.10**). Therefore, the membrane fouling mechanism of the porous graphene appears to be random depositions on the membrane surface in the absence of interpore fouling. The intrinsic membrane permeance in its pristine state is used to calculate the here-reported per-pore permeation of porous graphene membranes (**Figure 4.11**).

Furthermore, the model allows the extraction of the remaining open area of the membrane after a certain duration of the measurement. The relatively prominent fouling can be qualitatively understood by considering that the permeance is exceptionally high - at least one order of magnitude higher than that of commercial membranes of similar

4. Liquid transport at the Limit of Atomic Thinness

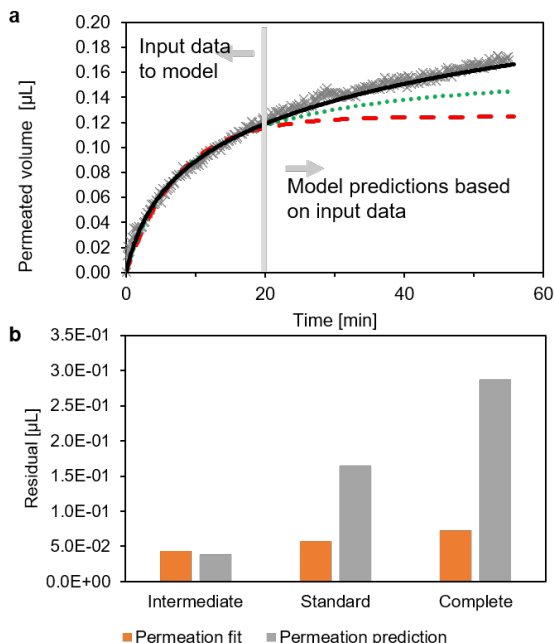


Figure 4.10: Comparing different fouling models. **a** Predicting the permeation behavior by using the first twenty minutes of measurement to fit the different models. Black, solid: intermediate fouling model; green, dotted: standard fouling model; red, dashed: complete clogging model. **b** Residual error between model fit and experimental data for 20 min of permeation from **a**. The intermediate model is superior to the standard and complete fouling models. Using the extracted model parameters to predict the permeation of the remainder of the measurement and then calculating the resulting residuals exemplifies the capability of the intermediate model to predict the permeation behavior well, while the other two models are significantly less accurate.

pore sizes. Each 2D pore permeates liquids at a significantly higher rate than any commercial membrane material, and therefore, it is not surprising to observe such a membrane fouling event. Based on the mechanistic understanding of the fouling, we conceive an approach preventing the self-contamination through conformal passivation of the porous graphene membrane to trap intrinsic contaminants on the surface thus reduce graphene fouling.

4.2. Liquid Permeation Measurements

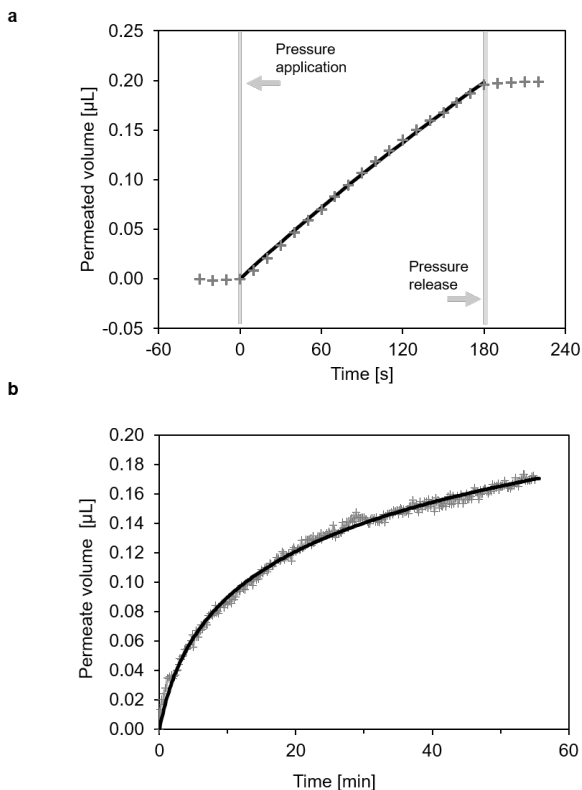


Figure 4.11: Pemeance extraction from permeation experiments. **a** Previous permeation example with close-to-zero fouling during experiment and corresponding model fit. **b** Long-term experiment shows significant permeance reduction over time and the fouling model to precisely describe the observed behavior.

Atomic Layer Deposition for Fouling Reduction

Atomic layer deposition (ALD) is utilized to deposit thin film titania (TiO_2) on the graphene membranes at 120°C (Oxford ALD) using $\text{Ti}(\text{OC}_3\text{H}_7)_4$ and O_3 as the two precursors. ALD can provide conformal passivation, which is potentially beneficial to keep the permeability of the membrane during operation. We employ ALD by titania

4. Liquid transport at the Limit of Atomic Thinness

(TiO_2) that is chemically stable in water, easy to manipulate, and inexpensive. Depositing 150 cycles of TiO_2 onto a PGM having 40 nm wide pores, we created a coated porous graphene membrane (c-PGM) with 24 nm wide pores (Methods section, SI). For the initial 40 s of permeation, we observe a similar permeation behavior between this coated membrane and a pristine PGM with 20 nm wide pores and similar per-pore permeances ($1.2 \times 10^{-22} \text{ m}^3(\text{sPa})^{-1}$ for PGM with 20 nm wide pores; $2.3 \times 10^{-22} \text{ m}^3(\text{sPa})^{-1}$ for c-PGM with 24 nm wide pores), whereas significantly reduced permeate is observed for the pristine (non-coated) membrane afterward (**Figure 4.12 a**). The permeation rates confirm this observation, where the ALD-coated membrane shows ca. 400 % higher per-pore permeation after 5 min in comparison to the pristine counterpart (**Figure 4.12**). Since the difference in pore size can only account for 70 % difference of permeation, the ALD-coated membrane indeed shows significantly less fouling. While the titania layer suppresses the fouling, we do not observe an alteration of the initial flow rate to similarly-sized pristine graphene membrane, which supports our assumption of negligible effects of pore edge chemistry for >5 nm wide pores.

Using the fouling model, the time τ until the initial membrane area has reduced to a certain fraction, f , can be predicted

$$f = \frac{A(t)}{A_0} = \frac{1}{1 + kc_cj\Delta p t} \quad (4.11)$$

$$\tau = \frac{1 - f}{fkccj\Delta p} \quad (4.12)$$

We define the membrane half-life as the time when the initial area has reduced to 50 % (**Figure 4.12 b**).

4.2. Liquid Permeation Measurements

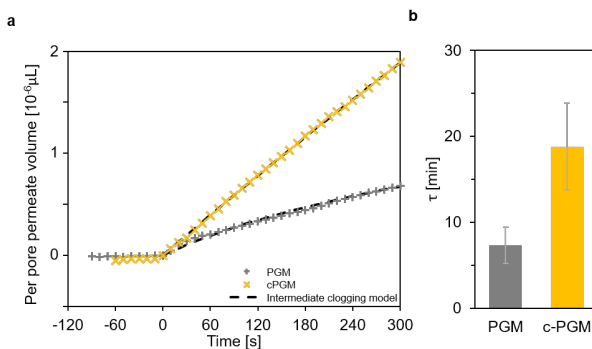


Figure 4.12: Comparing permeation over time of ALD-coated with non-coated membranes. **a** Experiment to two similarly sized ≈ 25 nm membranes with different coatings. The ALD-coated membrane displays nearly linear permeance over 5 min while the non-coated graphene membrane shows significant permeance decay within the first minute of flow across the membrane. **b** Extracted membrane half-life from various permeation experiments and fouling model applications. The average membrane half-life for throughflow experiments can be increased by a factor of almost 3 when performing ALD coating of the membranes.

$$\tau_{1/2} = \frac{1}{kc_c j \Delta p} \quad (4.13)$$

The reduced fouling increases the membrane lifetime, as demonstrated by comparing when the initial flow rate has reduced to one-half of its initial value. Comparison of the membrane half-life of PGM and c-PGM demonstrates that the ALD coating can effectively reduce membrane fouling and proves an effective strategy to increase membrane half-life by more than a factor of 2 (**Figure 4.12 b**).

ALD Coating To Change Pore Geometry

We further investigate the aspects of the ALD coating of PGM to precisely control the pore geometry by shrinking the pores and thickening the membrane (Methods section in the SI). ALD coating enables a shift of the average pore size of graphene membranes with little effect on the pore size distribution (**Figure 4.15**). The standard deviation of less

4. Liquid transport at the Limit of Atomic Thinness

than 3% of the respective average pore size confirms the precise fabrication by FIB and subsequent uniform coating of the pore rim, which is also qualitatively supported by the SEM images (**Figure 4.15**). We performed ALD with increasing cycle numbers for different pore sizes to study the deposition rates within graphene pores (**Figure 4.16**). TiO_2 nucleated immediately on the pore rim in the initial deposition cycles (**Figure 4.14**). Continued deposition formed a uniform coating in the graphene pore region. All pore sizes have reduced after the total cycle numbers, and we observe a trend of higher pore shrink rates for smaller pores. Interestingly, the 1000 and 500 nm graphene pores increase in size after the initial 50 cycles of ALD coating before starting to shrink for higher cycle numbers (**Figure 4.16**).

4.2.4 Atomic Layer Deposition to Change Pore Size & Membrane Thickness

We characterized the pore shrinkage for samples of various pore sizes to study the dependence of radial shrinkage rate of FIB milled pores for different pore sizes. SEM images were taken for each step with a resolution of approx 4 pixel/nm to precisely capture changes in pore size. We observed the radial deposition rate to increase for small pore diameters (**Figure 4.13**).

Large pores in graphene (500 nm to 1000 nm) show low radial deposition rates of 0.2 Angstrom/cycle, while small pores (20 nm on average) show rates of approx 0.1 Angstrom/cycle. Graphene pores between 500 nm and 1000 nm initial diameter show increase in pore size after the first 50 cycles. After 50 cycles of ALD, the pore diameters decreased with deposition cycle at a rate of ≈ 0.5 Angstrom/cycle, still smaller than the rate of small pores. We observe initial pore growth only for the largest pores, while sub-200-nm-wide pores decrease within the first 50 ALD cycles (**Figure 4.13**).

The initial deposition occurs mostly on defective sites, such as the

4.2. Liquid Permeation Measurements

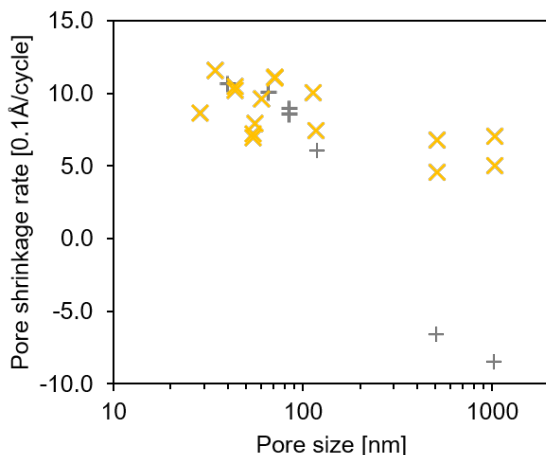


Figure 4.13: Pore shrinkage rate for various pore sizes. Smaller pores show larger shrinkage rates. Grey, pluses: initially uncoated graphene; gold, crosses: ALD coated graphene. Uncoated 500 nm and 1000 nm show negative pore shrinkage for the first 50 cycles. After 50 cycles ALD, the shrinkage rates stabilize near 0.5 nm/cycle.

pore edges, pore vicinity, and grain boundaries (**Figure 4.14**), in line with previous reports.⁹⁸ This observation is in line with our observation of preferential coating of the pore edge region, which consists of highly defective graphene caused by the FIB based patterning process (**Figure 4.14**).

The non-metallic precursor ozone could increase the graphene defect number as demonstrated for prolonged exposure of graphene to ozone at elevated temperatures.⁹⁹ We believe potential damage from ozone during the ALD process to be negligible to the membrane performance of ALD coated membranes as the defected sites serve as nucleation regions to the ALD layer and therefore would facilitate uniform coating of the graphene membrane. Furthermore, high-resolution STEM imaging of a few-cycle ALD deposition shows that no nucleation can be observed within graphene grains (**Figure 4.13**), suggesting pristine graphene to stay either unaffected or will immediately nucleate the ALD layer in the ozone exposure conditions used in our work.

4. Liquid transport at the Limit of Atomic Thinness

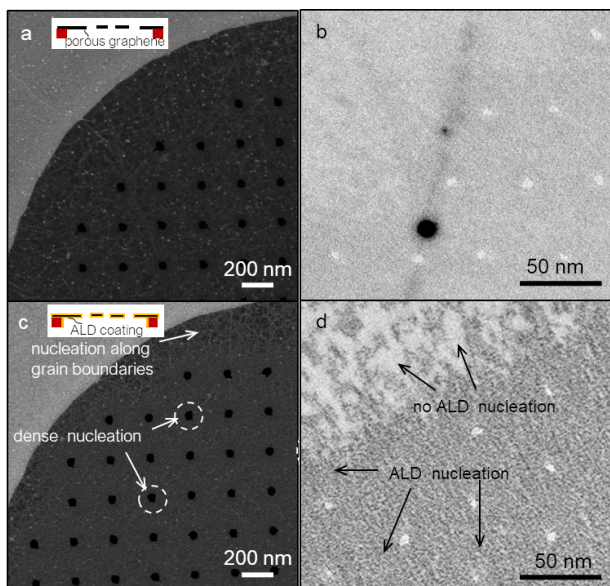


Figure 4.14: ALD nucleation locations. **a** Freestanding porous graphene with ≈ 50 nm pores before ALD coating. **b** Scanning electron micrograph (transmission electrons) of ≈ 6 nm pores before ALD coating. **c** The graphene membranes after 20 cycles of TiO_2 displays changes in its surface and different contrast, when using the same SEM imaging conditions as in **a**. **d** Scanning electron micrograph (transmission electrons) of the membrane above after 18 cycles of TiO_2 deposition displays significant ALD nucleation within the patterned graphene pore array. This Figures is also shown in the dissertation of Jakob Buchheim.⁹⁴

Cross-sectional images were obtained for ALD-coated graphene membranes after 625 cycles to obtain sufficient membrane thickness for precise SEM characterization.

The opening angles of thick porous ALD coated membranes were extracted using cross-sectional electron microscopy images (**Figure 4.17**). Upon extensive coating, an hourglass pore geometry emerges from homogeneous deposition around the pore rim, as schematically depicted (**Figure 4.18**).

SEM in tilted view reveals constricting pore geometries after extensive (625 cycles) ALD coating (**Figure 4.17**). Cross-sectional SEM images

4.2. Liquid Permeation Measurements

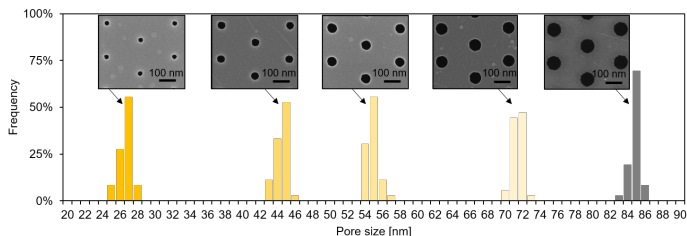


Figure 4.15: Influence of ALD coating on pore size distribution. Starting with ≈ 85 nm pores and narrow distribution, consecutive cycles of ALD coating homogeneously reduce the pore sizes down to ≈ 25 nm average pore size without increasing the distribution width notable. Due to the homogeneous deposition, while the pore size reduced from 85 nm to 25 nm, the membrane thickness increased to almost 100 nm.

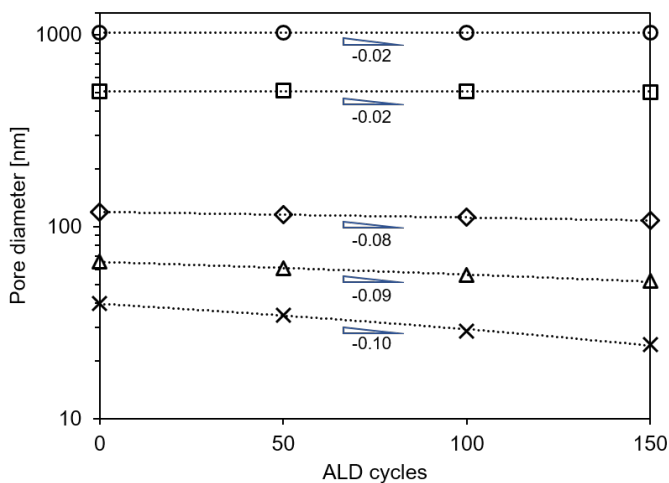


Figure 4.16: Detailed pore shrinkage quantification. Smaller graphene pores show higher shrinkage rates compared to larger graphene pores.

confirm the geometry to be an hourglass, a nanopore shape found in nature, e.g., in aquaporins.¹⁰⁰ The hourglass geometry emerges during coating because of homogeneous deposition around the pore edge. The resulting thickness (94 nm) of the membrane allows the inference

4. Liquid transport at the Limit of Atomic Thinness

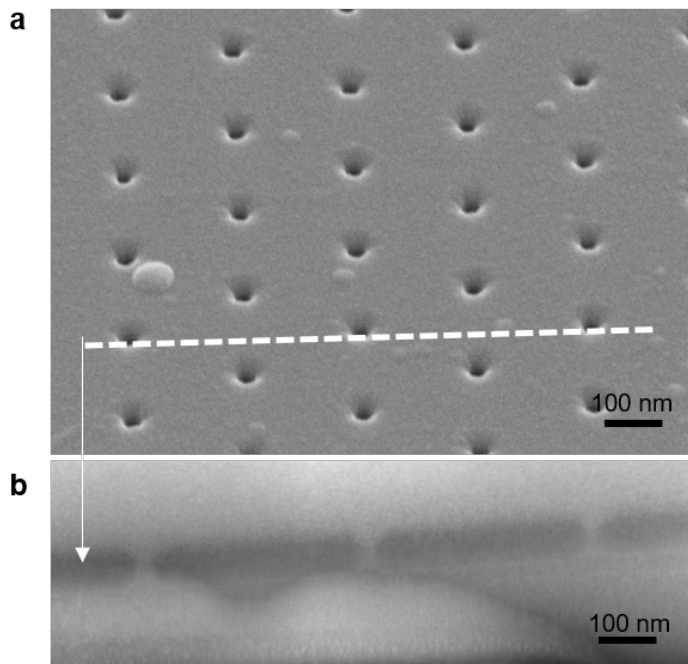


Figure 4.17: Birds-eye perspective of ALD coated graphene membrane. **a** The pores are ≈ 25 nm pores and have a funnel-like geometry. **b** Cross-section of the ALD coated membrane confirm symmetry, funnel-like geometry and ≈ 90 nm homogeneous membrane thickness.

of a lateral deposition rate of 0.75 nm/cycle that is used to calculate the thickness of other coated membranes. The developed understanding of the ALD rate enables the creation of pores with precisely defined dimensions using a specific number of ALD cycles applied. This approach allowed fabrication of ALD coated porous membranes with pore sizes ranging from 7 to 500 nm for transport characterization.

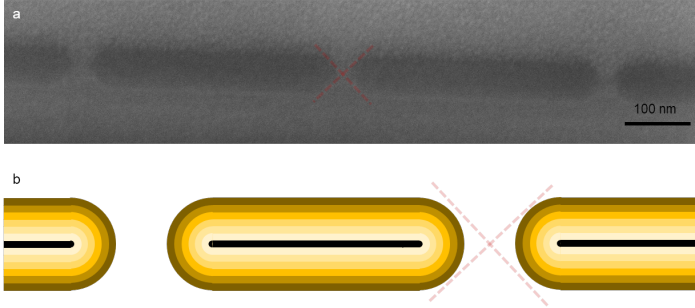


Figure 4.18: Membrane cross section and ALD deposition mechanism. **a** Cross-sectional electron microscopy image showing hourglass shaped nanopores with ca. 45° opening angle (dashed cross). **b** Schematic of ALD process layer by layer homogeneous deposition leads to hour-glass-shaped nanopores. Dashed red cross indicates approximate opening angle of the nanopores.

4.3 No-Slip, Continuum Permeation

4.3.1 Pore Size Scaling

Having established a precise membrane fabrication, measurement, and evaluation of liquid permeation, we examine parameters of viscous flow across an infinitesimally thin aperture. As hypothesized previously,⁴⁵ the continuum model derived from a no-slip Stokes flow through an infinitely thin aperture proposed by Sampson^{18,19} should apply.

$$Q = \frac{r^3}{3\mu} \Delta P \quad (4.14)$$

The solution of the Stokes flow, Q , across an infinitesimally thin orifice assuming no-slip at the pore edge depends on the pore radius, r ; the dynamic viscosity, μ ; and the pressure drop, Δp , across the membrane. Pore array effects, which can be significant for ionic transport,

4. *Liquid transport at the Limit of Atomic Thinness*

are negligible for liquid permeation for the porosities employed in this study.^{44,66,101}

The effects of pore edge chemistry that have been predicted to affect the permeation behavior for sub-nm pores are considered negligible in this work since the smallest diameter in this study is least one order of magnitude larger.^{54,58} Notably, the model lacks the transport length dependence, and consequently, the permeation is independent of the gradient of the driving force, unlike macroscopic mass and energy transfer. The entrance resistance for a viscous fluid in front of a pore is attributed to viscous dissipation associated with rearrangement of the streamlines in entering the pore and upon exiting into the downstream reservoir.¹⁰² Universally applied to all porous membranes, this resistance, or Sampson’s model, can offer an upper bound for pressure-driven viscous flows through any porous system.^{103,104}

Unlike a three-dimensional continuum flow, the Stokes flow across an orifice follows cubic scaling in the pore radius. The cubic scaling is indeed observed for our porous graphene samples with pore sizes between 6.1 and 1000 nm (**Figure 4.19**).

Notably, the per-pore permeation values obtained in this study display slightly higher values than in our previous report⁴⁵, likely because of improved experimental precision and preparation. Suk and Aluru have predicted that cubic scaling in r may hold for pore sizes even smaller than 6.1 nm.⁵²

4.3.2 Pressure Scaling

We normalize the permeation across a graphene pore by r^3 to obtain a universal pressure scaling for a given viscosity. We confirm linear scaling of transport with applied pressure, Δp , for both DI water as well as diethylene-glycol (Di-EG) with their viscosities spanning almost two orders of magnitude (**Figure 4.20**).

4.3. No-Slip, Continuum Permeation

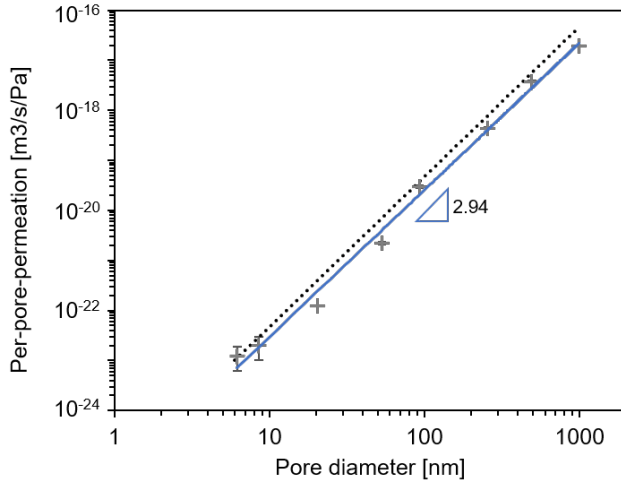


Figure 4.19: Pore diameter - permeance scaling. The per-pore-permeance increases with cubic proportionality to the pore diameter, albeit staying below the predictions of Sampson

4.3.3 Viscosity Scaling

The general scaling of permeation with viscosity shows inverse proportionality for fluid viscosities spanning almost two orders of magnitude (methanol, 580 μ Pas; and Di-EG, 36 500 μ Pas) (**Figure 4.21**).

Consequently, Sampson’s model is well-suited to describe permeation across atomically thin porous membranes. As mentioned above, mass transport is independent of the gradient of the driving force, unlike the macroscopic expectation in mass transfer.

Because of the infinitesimal thickness assumed in the derivation of Sampson’s model, it can be interpreted as a general upper bound of no-slip, continuum permeation across a pore of a given size over a wide angel of viscosities, pore sizes, and pressure. Since it is derived for infinitesimally thin apertures, a question arises at what thickness

4. Liquid transport at the Limit of Atomic Thinness

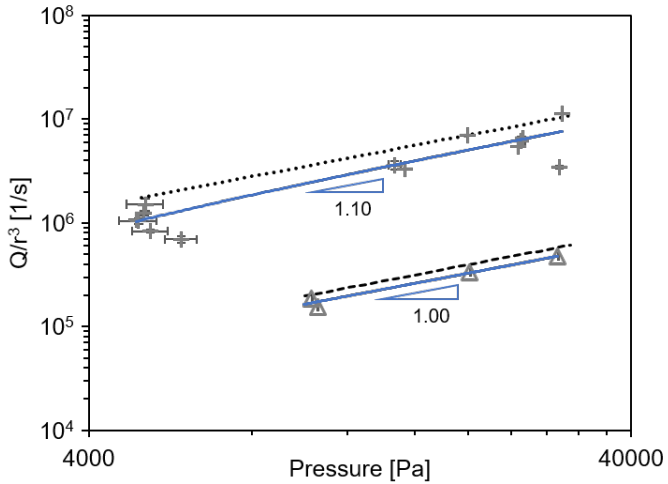


Figure 4.20: Pressure - permeance scaling. The permeance is proportional to the applied pressure to drive the flow.

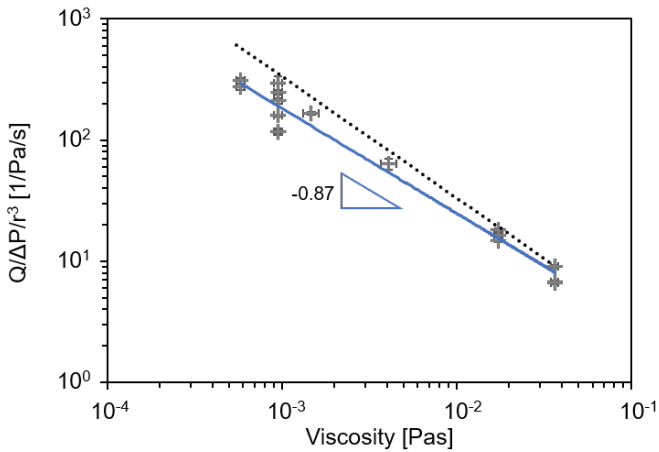


Figure 4.21: Fluid viscosity - permeance scaling. The permeance is inversely proportional to the viscosity.

or aspect ratio a membrane can indeed be approximated as infinitesimally thin.

In fact, for nanoporous membranes, many endeavors are exerted to cut the membrane thickness, which is rationalized by the assumption of the inverse proportionality of permeation with passage length. For this assumption to be valid, however, transport must be passage-limited or dominated by channel permeation resistance, which does not hold for infinitesimally short pores.

4.3.4 Rational Definition of Infinitesimal Thickness.

Given the importance of the membrane thickness reduction to permeation enhancement, it should be well-understood at what thickness the permeation becomes dominated by the entrance resistance such that a further reduction in thickness only marginally speeds up the permeation. The classical channel flow formalism of Hagen-Poiseuille predicts infinite permeation for channels with aspect ratios approaching zero. A model developed by Dagan et al., combining Hagen-Poiseuille and Sampson solutions as series resistances to permeation, predicts the transition from entrance-limited flow to passage-limited flow when the pore aspect ratio L/r is varied.²⁰

$$Q = \frac{r^3}{3\mu} \Delta p \left[1 + \frac{8}{3\pi} \frac{L}{r} \right]^{-1} \quad (4.15)$$

Permeation of specific pore size and pressure consequently scales nonlinearly with the aspect ratio of the channel within the framework of continuum description of the flow. We demonstrate the permeation dependency as a function of the membrane aspect ratio, varying over four orders of magnitude using pore sizes between 8 and 1020 nm and

4. Liquid transport at the Limit of Atomic Thinness

thicknesses between sub-1 nm (DLG) and 94 nm (625 cycles ALD on DLG) (**Figure 4.22**).

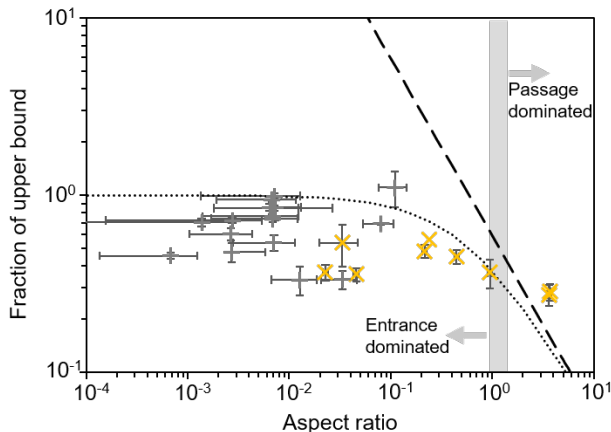


Figure 4.22: Challenging the membrane thinness paradigm. Per-pore-permeance normalized by the prediction of Sampson for various aspect ratio (L/r) membranes. Solid line: Hagen-Poiseuille equation prediction, conventionally adduced to motivate the pursuit of thinner membranes. Dashed line: Dagan's model²⁰ combining entrance (Sampson) and passage (Hagen-Poiseuille) resistances. Crosses: ALD-coated graphene membranes. Pluses: graphene membranes. For membrane aspect below one, the entrance resistance starts to dominate permeation, such that further reduction in membrane thickness, or aspect ratio, becomes less and less important as flow does not increase significantly.

Measured viscous permeation is normalized by the theoretical upper bound across infinitesimally thin pores provided by Sampson's model. A two-order-of-magnitude decrease in membrane thickness from an aspect ratio of 0.01 to 1 yield only a marginal increase in permeation within a factor of unity, disobeying inverse proportionality to thickness. Membranes with aspect ratios lower than unity will thus not yield in substantial permeation increase for further reduction of the membrane thickness, as predicted by a theoretical shift in permeation mechanism.

Instead, the focus of membrane design should shift toward other pa-

rameters such as porosity, mechanical stability, and support structure engineering because of an onset of scaling disparity between mechanical stress and permeation.^{86,92}

Flow Resistance Comparison

Classic Hagen-Poiseuille equation can be derived from Navier-Stokes equations assuming no-slip, laminar, viscous flow of a Newtonian fluid with fully developed parabolic velocity profile in a circular channel. The pressure forcing to drive the flow is balanced by wall shear stresses along the perimeter of the channel over the length of the channel in a steady flow. Integrating the obtained velocity profile from the force balance gives the volumetric flow rate for a given pressure drop

$$Q = \frac{\pi R^4}{8\mu} \frac{\Delta p}{L} \quad (4.16)$$

The flow resistance can be expressed as

$$\frac{\Delta p}{Q} = \frac{8\mu L}{\pi R^4} \quad (4.17)$$

The flow resistance for entry into an infinitesimally thin aperture, as derived from Stokes flow by Sampson, can be expressed as

$$\frac{\Delta p}{Q} = \frac{3\mu}{R^3} \quad (4.18)$$

Stokes flow assumes zero Reynolds number, which we here approximate with Reynolds numbers well below 1 for all membranes. Passage

4. *Liquid transport at the Limit of Atomic Thinness*

across a pore of finite length can thus be modeled as a series resistance of entry and passage events.^{20,101}

$$\frac{\Delta p}{Q} = \frac{3\mu}{R^3} + \frac{8\mu L}{\pi R^4} \quad (4.19)$$

A transition from access to passage dominated transport occurs when both resistances equal. The respective aspect ratio can be obtained as

$$\frac{L}{R} = \frac{3\pi}{8} \approx 1.18 \quad (4.20)$$

Therefore, for any membrane thinner than 1.18 its pore size, access resistance begins to dominate total transport resistance with vanishing membrane thickness dependence due to the inferior passage resistance.

Thin Film Stress and Permeation Scaling Comparison

Stress within a thin film can be expressed as

$$\sigma = \frac{\Delta p R}{2L} \quad (4.21)$$

With L being the film thickness.⁹²

Consequently, it is linearly dependent on the membrane aspect ratio. As shown in this work, however, permeation plateaus for aspect ratios below unity, such that the scaling laws for permeation and stress differ (equation 4.21). For thin membranes, thin-film stress could be

4.3. No-Slip, Continuum Permeation

reduced significantly by thickening an initially atomically thin membrane to aspect ratio around unity, while permeation remains largely unaffected. In such a way, overall membrane performance can be improved.

In view of permeation, an aspect ratio of unity can effectively be considered as reasonably close to an infinitesimally thin pore. Permeation is governed by entrance resistance, and a further reduction in the comparably small passage resistance will merely lead to an insignificant permeation increase. While it is clear that the size of the solute determines the maximum pore size of a membrane, our results suggest that the solute size also defines the optimal thickness (*via* pore size) for near-ultimate permeation at enhanced mechanical strength and reduced defects. Assuming straight pores, membrane thicknesses for reverse-osmosis, nanofiltration, ultrafiltration, and microfiltration on the order of 1, 10, 10^2 , and 10^3 nm, respectively, will permeate reasonably close to an infinitesimally thin membrane.

Interestingly, permeation across pores with aspect ratios above unity exceeds a corresponding prediction by Hagen-Poiseuille formalism (**Figure 4.22**). We attribute this enhancement to the hourglass-shaped cross-sectional geometry that our pores possess upon extensive ALD coating (**Figure 4.17**). The opening angle of these membranes is extracted from SEM cross-sectional images of 45° , and the permeation can thus be compared to a theoretical prediction for such a geometry.¹⁰⁵ For a viscous channel flow across an hourglass geometry, permeation is predicted to be 20 % that of Sampson's model, which matches well with the experimentally measured ones (here, 29 % and 28 % for each membrane, respectively). Furthermore, this prediction is for an infinitely thick pore with 45° opening angle, indicating that a further increase of membrane thickness will not reduce permeation if the opening angle is kept constant.¹⁰⁵ Thus, the pore cross-sectional geometry affects the permeation of ultrathin membranes and serves as a parameter to be considered in nanoporous membrane design.

4.3.5 Upper Bound for Viscous Permeation through Pores

As the entrance resistance of Sampson's model contains no thickness dependence, mass transport is independent of the pressure gradient, unlike conventional modes of transport. Such entrance-resistance-dominated and gradient-independent transport has also been observed for ionic conductance across thin nanopores and is predicted for diffusion across infinitely thin apertures.^{62,66,106}

Since it is universal for any pore, Sampson's model may serve as a benchmark for permeation across porous materials. Our measurements show an invariance of the viscous permeation through porous membranes for aspect ratios up to unity (**Figure 4.22**). These membranes are not thick enough to contribute notable wall shear forces to the fluid, but the viscous dissipation for low-aspect-ratio membranes occurs mainly in the bulk fluid around the pore entrance, as shown theoretically before.^{102,103} Comparison to single-layer graphene membrane simulations as well as experiments with down to sub-1 nm pore sizes have shown scattered permeation near the theoretical upper bound.^{45,52,55–57,107} This finding suggests the applicability of the entrance-dominated flow even down to the limit of the continuum regime.

Reported experimental permeation data of numerous high flux membranes, like carbon nanotube (CNT) membranes^{50,93,112,116}, porous nanocrystalline silicon (pnc-Si)¹⁰⁸, and carbon nanomembranes (CNMs)¹⁰⁹, confirm that Sampson's theory yields a valid estimation of the upper bound for pressure-driven flow across any porous material (**Figure 4.23**). The reported permeation data for CNTs are scattered around the Sampson line supporting the hypothesis that most viscous dissipation occurs at the entrance around the nanotube pore but not inside the confinement, such that permeation across CNTs is limited by entrance resistance.^{103,110}

Permeation across commercial polycarbonate track-etched membranes and boron nitride nanotubes, which have been shown to have a negligi-

4.3. No-Slip, Continuum Permeation

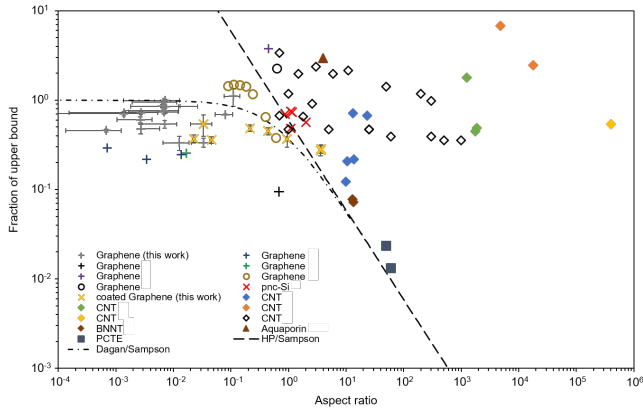


Figure 4.23: Permeation comparison of various membrane materials normalized by the upper bound of entrance resistance. Experiment and simulation of graphene [Pluses: gray (this work), blue⁴⁵, green¹⁰⁷, purple⁵⁵, and black⁵⁶; brown triangles⁵² and black circles⁵⁷] range near the upper bound with aspect ratios below one. Single-layer graphene with sub-1 nm pores is reported both above and below the upper bound (purple and black pluses, black and brown circles). c-PGMs (this work, gold crosses), pnc-Si membranes (red¹⁰⁸ cross), and carbon nanomembranes (gray circles)¹⁰⁹ do not surpass the theoretical upper bound. Carbon nanotubes are scattered around the upper bound, with invariance to aspect ratio (black diamonds¹¹⁰, blue diamonds⁹³, green diamonds⁵⁰, orange diamonds¹¹¹, yellow diamonds¹¹²). Conventional PCTE membranes (gray squares) and boron nitride nanotubes (brown diamonds⁹³) range near the classic Hagen-Poiseuille prediction. Aquaporin transport (brown triangles^{110,113–115}) ranges above the upper bound, possibly due to non-continuum and pore geometry effects.^{100,102}

ble slip, falls on the prediction by Hagen-Poiseuille formulation.⁹³ An extensive molecular dynamics simulation of transport across CNTs, including entrance effects for various aspect ratios, follows the upper bound with a mild decrease at high aspect ratios due to nonzero friction within the CNT channels.¹¹⁰ Furthermore, transport across biological channels such as aquaporins lies within the reasonable expectation of the upper bound.^{110,113–115}

It is important to note that Sampson’s theory is not a strict upper bound for permeation since the numerical prefactor ($1/3$ used in this work, based on the original formulation) has been predicted differently in various works.^{102,110} In addition, effects like slip at the pore entry and cone-shaped entrance geometries, as presented above and reported

4. *Liquid transport at the Limit of Atomic Thinness*

elsewhere, have the ability to decrease dissipation in the entrance region theoretically and therefore to enhance the flow with respect to Sampson's theory.^{52,102}

Similarly, molecular-sized confinements could advance the permeation rate beyond continuum limits.^{117,118} Notably, CNT membranes are reported to have very high flow enhancements considering three-dimensional flow theory, which accounts for their thickness.^{50,93,111,112}

The effect of flow enhancement is generally attributed to high slip lengths inside the pore caused by the pore wall properties of high curvature graphitic surfaces¹¹⁹ or special phonon coupling of CNT to the liquid.¹²⁰ However, upon a comparison of the permeation of these high flux membranes with thin membranes (aspect ratio ≈ 1), the permeation rate of fluid is not significantly enhanced, which indicates that even very special no-slip material surface membranes cannot significantly reduce the pore entrance resistance.

Consequently, even high-slip pore wall membranes cannot exceed the here-reported permeation rates of the thin porous graphene membranes because, in both cases, flow is governed mainly by viscous dissipation near the pore entrance. Thus, improving membrane permeance for these entrance-dominated materials should be addressed by increasing the pore density¹⁰⁹ and reducing support structure resistance. Enhancing per-pore permeation further requires engineering of the pore entrance properties toward reduced viscous dissipation in front of the pore.

4.4 Discussion

In conclusion, we demonstrated the combination of FIB and ALD as a set of technologies to investigate liquid permeation with high precision across nanoporous graphene and ultrathin ALD-coated membranes. Detailed permeation characterizations allowed the probing of the fouling mechanism of nanoporous graphene membranes, and ALD

has proven as an effective protection strategy to increase the membrane operation lifetime.

The transport of liquids across an infinitely thin orifice follows the relation described by Sampson's model for various fluids and pores as small as 6 nm. Permeation across such pores is independent of membrane thickness and governed by entrance resistance. Any viscous fluid must overcome this pore entrance resistance, which consequently serves as the upper bound to viscous flow for any pore. Application of ALD coating allowed facile alteration of membrane thickness to investigate the paradigm of inverse proportionality between permeation and membrane thickness. Our results demonstrate this paradigm as inapplicable for pores of aspect ratios below one. For these membranes, transport is dominated by entrance resistance such that order-of-magnitude reduction of aspect ratios below one does not significantly increase permeation.

Our report enhances the understanding of flow physics through porous materials employed across various fields and for nanoporous membrane architectures designed for applications ranging from reverse osmosis to microfiltration. The shift of the transport mechanism from passage- to entrance-dominated permeation at pore aspect ratios close to unity marks the border as a practical approximation of infinitesimal thickness. The effect of pore cross-sectional geometry observed in ALD-coated graphene membranes, moreover, enriches the detailed understanding of viscous permeation across nanopores, where hourglass-shaped pores show enhanced transport over straight pores in line with previous findings.

Nanoporous membranes can, therefore, be designed in a rational way to optimize the permeation-thickness trade-off for given pore size, achieving ultimate permeation and minimized defects while maintaining mechanical strength *via* thickness optimization and pore geometry engineering. The entrance-resistance-limited transport is shown to apply to various reported high-flux materials, suggesting a general upper bound to permeation across a nanopore.

Chapter 5

Scalable Manufacturing of Nanoporous Graphene Membranes

This section is published in parts as:

Karl-Philipp Schlichting and Dimos Poulikakos. “*Selective Etching of Graphene Nanopores: From Molecular Sieving to Extreme Permeance*” *ACS Applied Materials & Interfaces*, **2020**, 12(32), 36468-36477, DOI:<https://doi.org/acsami.0c07277>

5.1 State of Graphene Membrane Manufacturing

Separating gases using membranes promises substantial energy savings over phase change based processes.¹ To harvest this potential,

5. Scalable Manufacturing of Nanoporous Graphene Membranes

transport across the membranes should be maximized for high process throughput at a small device footprint, while maintaining required selectivity.

Graphene is a promising novel membrane material due to its atomic thickness. Impermeability in its pristine state, however, requires that nanopores are introduced to create a functional membrane.¹¹ Pioneering studies predicted the potential of graphene nanopores for gas separation, ion rejection, and water permeation.^{12–14} Experimentally, exfoliated graphene membranes demonstrated exceedingly high selectivities.³⁶

Since the demonstration of graphene's potential for separation, substantial efforts were expended to develop methods for controllably perforating graphene and to study the gas transport mechanisms. Focused ion beam drilling of pores down to 7 nm diameter showed a transition from collective to effusive flow approaching Knudsen selectivity.⁴⁵ Pores with sub-nm dimensions demonstrated gas selectivities in the molecular sieving regime well above Knudsen selectivity.^{40,121–123} Despite such important results, various phenomena such as pore chemistry^{27,30,31,124,125}, molecular orientation^{14,125}, as well as surface transport^{26,33,125,126}, are predicted to influence transport across graphene nanopores with vastly differing permeance and selectivities at a given pore size.^{127,128} These facts necessitate new experimental efforts both for verification and realization purposes.^{29,30,129,130}

The experimental study of the gas transport mechanisms is impaired by a lack of suitable manufacturing pathways allowing controlled pore formation and pore size expansion from sub-nm to larger diameters. Pores can be introduced either serially or in parallel into the graphene crystal. The high number of pores required for practical membranes renders serial perforation unrealistic with required pore densities exceeding $1 \times 10^{14} \text{ m}^{-2}$ to overcome the permeance of polymeric membranes.¹²⁹ In parallel processes, pores are either created bottom-up during graphene synthesis or top-down after synthesis. Currently, bottom-up processes are limited by membrane areas of tens of nanometers in lateral dimension^{131,132} or pore size above tens of nanome-

5.2. Selective Nanopore Etching for Graphene Membranes

ters.^{133,134}

On the other hand, top-down methods, if based on particles^{134,135}, cannot create pores small enough for attractive gas selectivity, or utilize non-selective plasma or ozone etching that randomly create defects into pristine graphene preventing independent control of pore number and size.^{36,40,122}

Other previous approaches to expand pore sizes rely on wet chemical etching and were limited to pore sizes below 2 nm with increasing pore number density for prolonged etching time, created contaminations from the etchants on the membrane surface, and faced the drawback of membrane ruptures due to capillary forces after drying the membrane from the liquid etching approach.⁵⁶ Despite progress toward high permeance and selectivity, processes with independent control of pore density and size are still sought for in order to optimize membrane permeance and selectivity independently.⁴⁰ Additionally, the ability to expand membrane pore size without changing the pore number density is required to enable investigation of gas transport mechanism across a broad spectrum of pore sizes. Ultimately, such processes can result in a universal graphene membrane fabrication platform that can address pore densities and sizes required by various separation applications.

5.2 Selective Nanopore Etching for Graphene Membranes

We present a dry, facile, and scalable graphene perforation approach using a two-step process with independent control of pore densities and pore sizes. Energetic ion irradiation of double-layer graphene membranes creates sub-nm defects acting as nucleation centers for pores. Subsequent etching using oxygen gas selectively enlarges these defects into pores with narrow size distributions, enabling pore size control via etching duration. These membranes possess mean diameters ranging from sub-nm to ≈ 5 nm. The membranes display gas sieving with

5. Scalable Manufacturing of Nanoporous Graphene Membranes

unprecedented permeances, up to three orders of magnitude higher permeance than state-of-the-art membranes at similar selectivity.

Furthermore, we apply the selective pore expansion strategy to study gas transport mechanisms when expanding the pore size and find surface flow, pore chemistry, and momentum transfer to influence gas separation when transitioning from molecular sieving to effusion. The scale of fabrication is determined by the size of the graphene CVD sample, the size of the ion irradiation area, and the size of the oxygen annealing chamber, all of which are commercially available up to 4" in size. Therefore, defect nucleation by energetic ions and parallel pore expansion method by selective oxygen etching are both scalable and pave way toward membranes sized for separation applications ranging from gas separation and desalination, to nano- and ultrafiltration.

Porous graphene membrane fabrication proceeds from freestanding double-layer graphene (DLG) spanned over custom-made silicon nitride frames (**Figure 5.1 a**).

In the first step, defects are introduced into DLG to define nucleation centers for the pores. Here, unfocussed, high-energy ion irradiation is utilized, creating atomically small defects into single and few layers of graphene (**Figure 5.1 b**).^{68,136–138} The DLG is defective after irradiation. In the second step, annealing the samples in oxygen at elevated temperatures selectively etches and enlarges the defects into nanopores without etching pristine graphene (**Figure 5.1 d,e**).

Single-layer graphene (SLG) grown by chemical vapor deposition (CVD) was purchased (GrapheneA) and transferred using an adaption of the well-known polymer-based technique.¹³⁹ Here, instead of using Poly(methyl methacrylate), another polymer, namely Poly-(phthalaldehyde) (PPA) was used (AllResist GmbH). PPA sublimates during heating instead of melting, which is beneficial for approaching a more atomically clean surface. PPA solution (7 wt % in anisole) is spun (4000 rpm, 40 s) on the graphene surface and cured for 2 min on a 100 °C hotplate. Subsequently, a double layer of graphene is transferred as described elsewhere.¹³⁹

5.2. Selective Nanopore Etching for Graphene Membranes

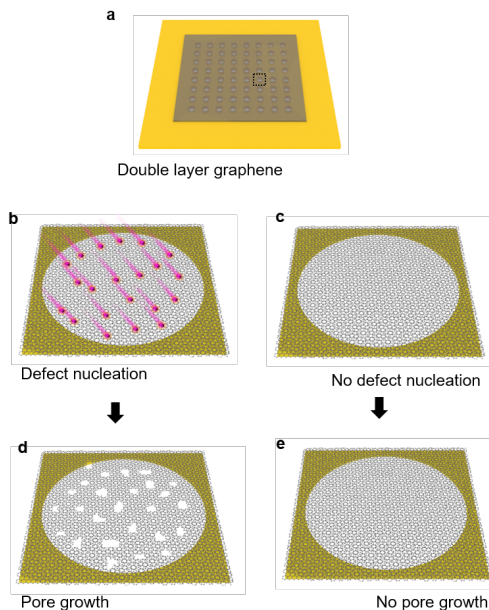


Figure 5.1: Principle of membrane fabrication. **a** DLG is transferred to a porous silicon nitride frame. **b** Irradiation with energetic ions nucleates defects in selected regions of the DLG membrane. **c,d** Selective etching in oxygen gas enlarges the defects by design from ion irradiation into pores (**d**), while pristine DLG remains unaffected (**e**).

In brief, after spin coating PPA onto the SLG/Cu composite, the sample is subsequently floated on a solution of ammonium persulfate (0.5 M, Sigma Aldrich) to remove the copper foil. After dissolving the copper foil is dissolved, the floating PPA/SLG is transferred onto a de-ionized (DI) water surface for rinsing. Next, the floating PPA/SLG composite is fished out by a second SLG/Cu to create a double layer graphene on copper. The etching in APS and rinsing in DI is repeated, and the PPA/DLG composite is fished out and dried on a custom made Si_3N_4 -chip containing arrays of 64 holes of 4 μm or 6 μm diameter resulting in freestanding DLG membranes.

Using DLG instead of SLG increases the transfer yield of membranes and additionally reduces leakage pathways through intrinsic defects

5. Scalable Manufacturing of Nanoporous Graphene Membranes

within the graphene.^{121,122} Notably, for fishing the PPA/Gr composite from a water bath, a non-polished SiO_2 wafer is used, which has been exposed to O_2 plasma (600 W, 1 min) to render it hydrophilic. This enables the PPA/Gr composite to float on a thin water layer and reduces both contamination and mechanical disintegration of the composite during transfer. After thermal removal (Lindberg blue tube furnace; 400 °C, 1 bar, 900 sccm H_2 , 100 sccm Ar , 2 h) of the PPA layer from the DLG/ Si_3N_4 frame composite, the samples are annealed for 30 min at 4 mbar in 500 °C H_2/Ar (50/50) atmosphere (AS-One, AnnealSys). The vacuum annealing step is done directly before any further membrane processing to minimize potential surface adsorbates.

5.2.1 Selective Etching Conditions

The binding energy of carbon atoms at lattice edges is substantially reduced such that chemical etching at the edges can occur while the pristine lattice remains unaffected.¹³⁸ Suspended graphene etches more regularly at lower oxygen pressures, which is additionally beneficial for selective etching.^{140,141} We, therefore, chose the lower pressure limit of our system (1 mbar) to study the temperature effect on selective etching using two hours of etching duration (**Figure 5.3**). Nanopores in graphene appear as black spots in the scanning electron microscopy (SEM) images (**Figure 5.1 d, e**), while graphene is grey and intrinsic particle residues from fabrication appear bright. While the particles could not be completely removed in fabrication development, they were not negatively affected by membrane fabrication. Each sample consists of two regions: one ion irradiated region and one control region without ion irradiation. For temperatures of 250 °C or less, we rarely observe pores after etching in both regions (**Figure 5.2,5.3**). Etching at 300 °C creates a high density of nanopores within the ion-irradiated region, while the control region remains non-porous. At 350 °C, the pore density in the ion region decreases, and the pore size distribution broadens. Furthermore, the control region exhibits nanopores with

5.2. *Selective Nanopore Etching for Graphene Membranes*

a similar density as the ion region, revealing etch selectivity loss. At 400 °C, the graphene is burnt off uncontrollably in both regions, marking the effective upper bound for the temperature parameter window (**Figure 5.3**).

5. Scalable Manufacturing of Nanoporous Graphene Membranes

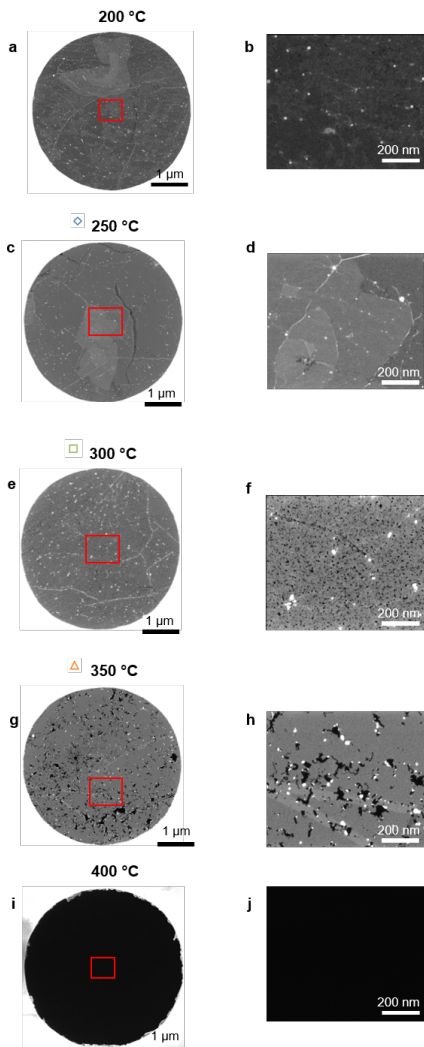


Figure 5.2: Identification of selective etching temperature. **a, b** DLG post ion irradiation and 2 h oxygen etching at 200 °C largely non-porous. Red box marks region of higher magnification image in image to the right. **c, d** oxygen etching at 200 °C: graphene stays largely non-porous. **e, f** DLG post ions and 2 h oxygen etching at 300 °C show highly porous DLG with uniform pore density and size across membrane. **g, h** DLG post ions and 2 h etching at 350 °C show highly porous DLG with non-uniform pore density and size across membrane. Etching of defective graphene 400 °C leads to complete etching of freestanding DLG (**i, j**).

5.2. *Selective Nanopore Etching for Graphene Membranes*

Aside from investigating the pore creation in ion irradiated regions, each sample contained a region without ion irradiation as control. Their comparison allowed investigation for defect creation in pristine DLG for potential non-selective graphene etching. Temperatures below 300 °C rarely show detectable pores after 2 h etching at 1 mbar O_2 (**Figure 5.3**). At 350 °C, pores emerge within the control regions, revealing non-selective etching of graphene. Increasing the temperature to 400 °C, leads to marked etching of the control region with large pinholes and ruptures emerging. The temperatures to achieve selective graphene etching are consequently below 350 °C in order to prevent uncontrolled pore introduction in pristine graphene areas.

5. Scalable Manufacturing of Nanoporous Graphene Membranes

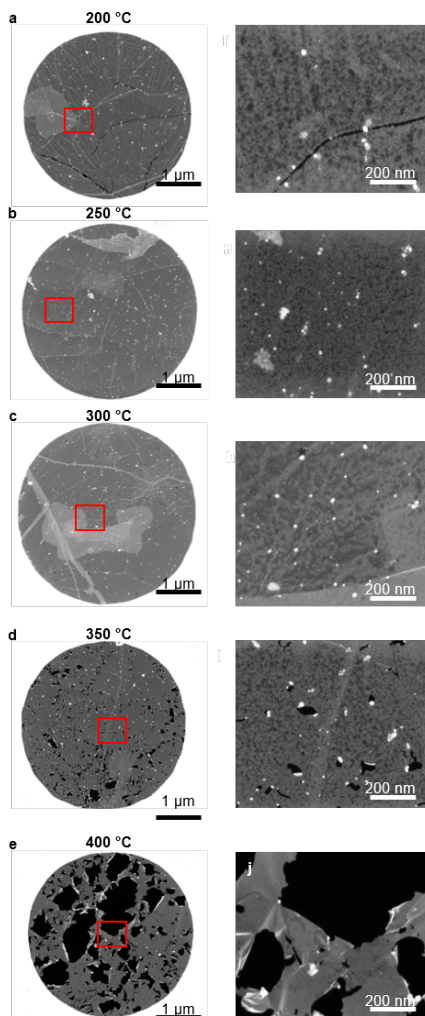


Figure 5.3: Selective etching control experiments. Control regions without ion irradiation after 2 h etching at different temperatures, with magnified region to the right of it. Temperatures of 200 °C (a), 250 °C (b), 300 °C (c), 350 °C (d), and 400 °C (e) were tested. For etching temperatures of 300 °C and below no pores are detectable. At higher temperatures (350 °C and 400 °C) DLG becomes porous indicating etching of pristine DLG and thus loss of selective etching conditions

5.2. Selective Nanopore Etching for Graphene Membranes

Analysis of the pore densities shows not only significantly lower pore densities for control regions below 300 °C, but also that the pores introduced for temperatures of 350 °C or higher are significantly larger in average diameter and standard deviation, reducing feasibility for membrane applications.

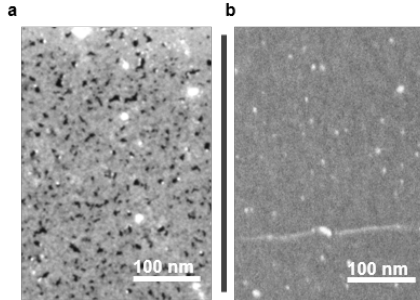


Figure 5.4: Selective etching comparison. **a** SEM image of DLG after ion irradiation and 2 h oxygen etching shows highly porous DLG with pores in random locations according to the ion irradiation. **b** The same sample after oxygen etching, however, without prior ion irradiation shows no pores.

5. Scalable Manufacturing of Nanoporous Graphene Membranes

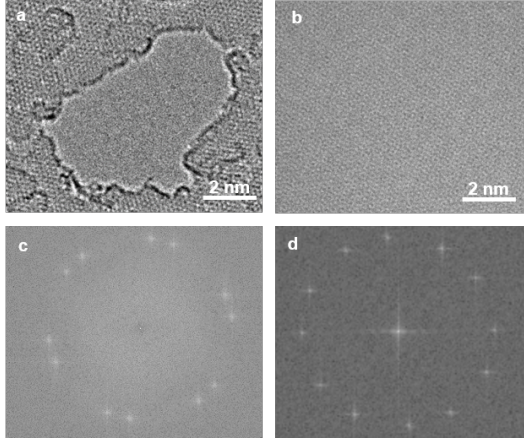


Figure 5.5: TEM analysis. **a** TEM image of a single nanopore etched into graphene during 2 h of selective oxygen etching reveals a crystalline graphene structure at the pore edge. **b** DLG after 2 h selective oxygen etching without prior defect nucleation. DLG is unaffected and stays pristine with absence of atomically small defects. **c** Fourier transform of the TEM image (**a**) shows diffraction pattern of pristine DLG structure without amorphous regions. (**d**) Fourier transform of (**b**) shows typical diffraction pattern of DLG without amorphous regions.

5.2.2 Pore size quantification

ImageJ open source software was used for pore size evaluation (**Figure 5.6**).¹⁴² The pores were detected by thresholding to obtain the number of pores, N_p , in the imaged membrane area, A_{img} . The pore number density, n_p , was obtained from the total number of detected pores and the total imaged area according to

$$n_p = \frac{\Sigma N_p}{\Sigma A_{img}} \quad (5.1)$$

The pore size distribution was obtained by calculating the equivalent diameter, d_{pore} , of each pore with area, A_{pore} ,

$$d_{pore} = 2\sqrt{\frac{A_{pore}}{\pi}} \quad (5.2)$$

5.2. Selective Nanopore Etching for Graphene Membranes

and counting the occurrences of certain pore size intervals in a histogram. A log-normal fit of the detected pore diameters describes the distribution of pores most accurately, in line with a parallel growth mechanism.

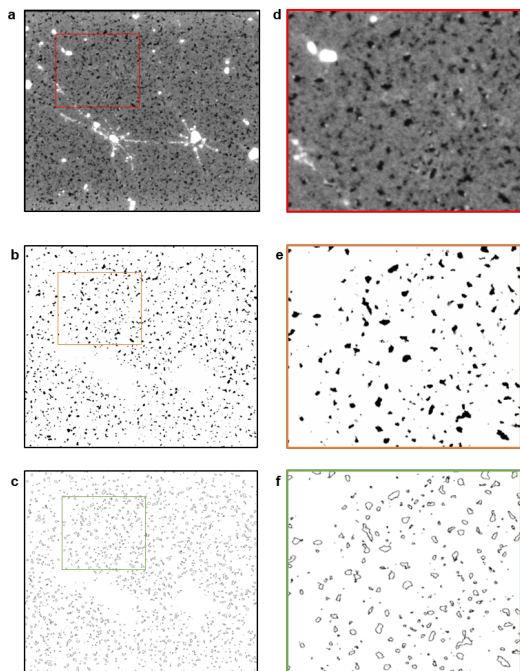


Figure 5.6: Pore size quantification. **a** Example of SEM image showing a sample of a membrane. Boxes are magnified views of the image to their left for better visibility. **b** Thresholded image of pores detected in **a**. **c** Pore circumferences detected from ImageJ algorithm.

Quantitative pore size analysis reveals log-normal distributions (**Figure 5.8**). Etching temperatures of 250 °C and below show few pores and 350 °C etching temperatures result in broad pore size distributions with more pores of larger diameter. Etching at 300 °C, yields the highest number of small pores and the narrowest pore size distributions.

5. Scalable Manufacturing of Nanoporous Graphene Membranes

These observations identify 300 °C and 1 mbar as the optimal conditions for selective oxygen etching to fabricate nanoporous graphene membranes with narrow pore size distributions. Comparing the pore densities of both regions further underpins 300 °C as the optimal temperature for highest etch selectivity (**Figure 5.11**). Under these conditions, defects nucleated by ion irradiation are selectively expanded in size to increase the pore diameter *via* oxygen etching time. Etching only at the defects allows predefining the membrane permeance in the first step via ion dose to control pore number density and then controlling the membrane pore size, which will determine the membrane selectivity.

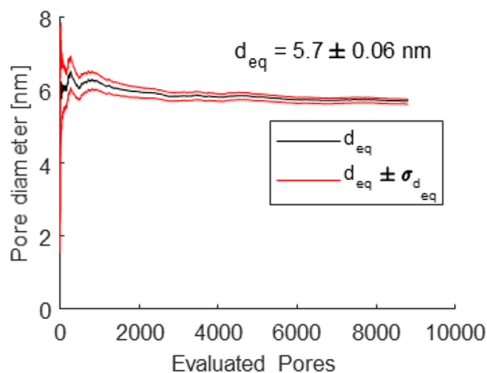


Figure 5.7: Evolution of the equivalent pore diameter as function of evaluated nanopores. After a few hundred evaluated pores, the mean diameter does not change significantly anymore and only the uncertainty interval regarding the true mean of the distribution becomes marginally narrower with increasing pore number evaluation.

5.2. Selective Nanopore Etching for Graphene Membranes

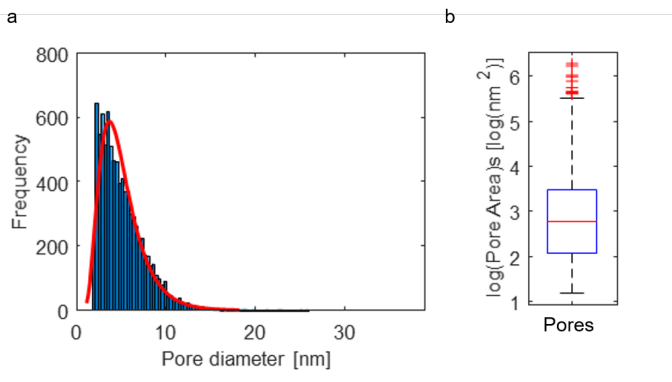


Figure 5.8: Pore size distribution. **a** Count of measured pore diameters and corresponding log-normal fit (red line) without any notable outliers of larger pores from the distribution. **b** Boxplot of the logarithm of pore area with a fraction of the open area that is outside the 999 percentile of the log-normal distribution. For this sample, the total open area of outliers (red pluses) from the log-normal fit, corresponds to 1.62% of the total open area of pores from within the log-normal distribution.

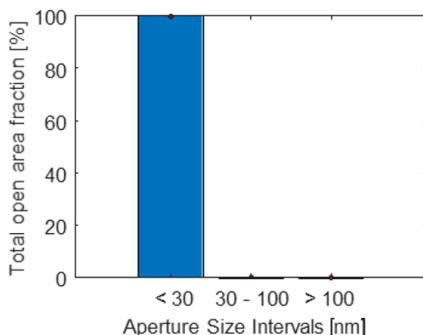


Figure 5.9: Exemplary open area contribution of nanopores (< 30 nm), pinholes (30 nm – 100 nm) and ruptures (> 100 nm) to total open area of the membrane. For effusive transport, the total contribution to flow is proportional to the areas. All membranes considered had > 80% contribution from the pores introduced by design.

Transmission electron microscopy (TEM) images were obtained with

5. Scalable Manufacturing of Nanoporous Graphene Membranes

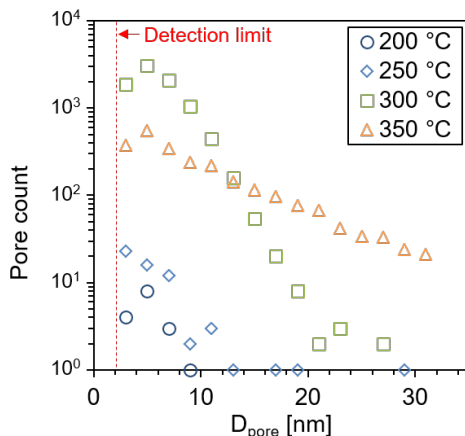


Figure 5.10: Pore Size distribution comparisons. Pore size distributions for pores larger than the detection limit (red dashed line). Etching below 300 °C results in very low pore density opposed to 300 °C etching. Etching at 350 °C results in lower density of small pores compared to 300 °C etching and significantly more pores of larger diameters. Pore size distributions are log-normally distributed with 300 °C etching showing the steepest decay of pore count for larger pores. These membranes show the narrowest pore size distributions and pore size cut-offs

80 kV acceleration (FEI Gatan Grand ARM) without prior treatment to avoid potential changes in the membrane surface.

Transmission electron microscopy (TEM) was used to analyze the surface of the membranes exposed to different processing steps at the atomic level (**Figure 5.5**). Within the regions of a TEM sample, almost no defects at the atomic level could be found in untreated DLG (**Figure 5.5 a**). Upon ion irradiation, atomically small defects appear (**Figure 5.5 b**). The samples after ion irradiation and two-hour annealing show nanopores of ≈ 5 nm lateral dimensions, but at the same time, many atomically small lattice disorders (**Figure 5.5 c**) are found, opposite to a control sample, which was not ion-irradiated but only etched for two hours (**Figure 5.5 d**). This further confirms the applied etching conditions do not etch pristine graphene and further do not turn every atomic defect into a nanopore, contributing to

5.2. Selective Nanopore Etching for Graphene Membranes

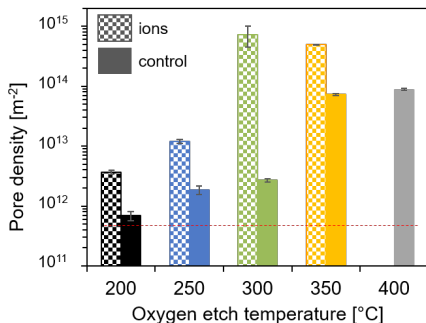


Figure 5.11: Pore density comparison. Comparison of pore density obtained in ion irradiated regions (patterned bars) compared to control regions (solid bars) without ion irradiation at various etching temperatures. The pore density of membranes etched at 300 $^{\circ}\text{C}$ is highest while also the pore density in the control region stays very low compared to etching at higher temperatures. The etch selectivity for membranes etched at 300 $^{\circ}\text{C}$ is the highest, while simultaneously displaying narrow pore size distribution at high pore density

the offset between ion density and pore density.

Based on the experimental observation of exclusive pore expansion in ion irradiated graphene regions for our identified annealing conditions, we conclude the pore expansion mechanism to begin at atomic defects nucleated by ion impact, upon which carbon atoms are removed from the DLG lattice in a two-step oxidation mechanism (**Figure 5.13**).¹⁴¹ Upon annealing in oxygen at the optimized conditions for selective etching, carbon edge atoms react with the available oxygen in the atmosphere and gradually expand the pore size over time with potentially carbonyl groups at the edge.¹⁴¹

Higher magnification TEM images confirm the observations of atomically small defect introduction from ion irradiation with atomic lattice irregularities in the graphene with spatial dimensions well below one nanometer in size (**Figure 5.14**). DLG before and after oxygen etching without ion irradiation remains free of observable atomically small defects, further confirming defects to be necessary for pore expansion

5. Scalable Manufacturing of Nanoporous Graphene Membranes

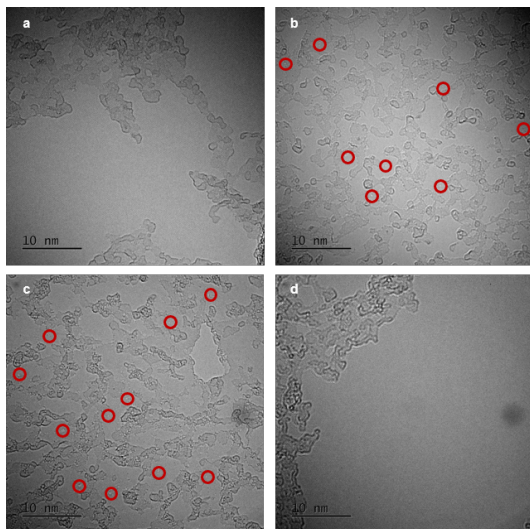


Figure 5.12: TEM images of differently treated membranes. **a** DLG without atomic scale defects of lattice irregularities, however, partly covered with polymeric residues from transfer. **b** ion irradiated DLG. Red circles indicate atomically small defects. **c** ion irradiated DLG after two hours oxygen etching. Red circles indicate atomically small defects that did not grow into a nanopore such as one seen the in the top right of that image. **d** Control sample etched for two hours in oxygen without prior ion irradiation. No atomically small defects are found.

and the selective nature of the etching conditions that only remove carbon atoms from the edge and not from pristine graphene.

All membranes were imaged in an SEM (FEI Helios 450) at various magnifications to rule out potential ruptures, pinholes, or defects other than the nanopores from membrane manufacturing before measurement. The total membrane area was small enough to rule out ruptures with equivalent diameters larger than (50 nm), while pinholes and defects down to 10 nm diameter were statistically accounted for or ruled out by sampling the membrane area using higher magnification SEM micrographs. Pore size and density evaluations were carried out by ImageJ analysis

5.2. Selective Nanopore Etching for Graphene Membranes

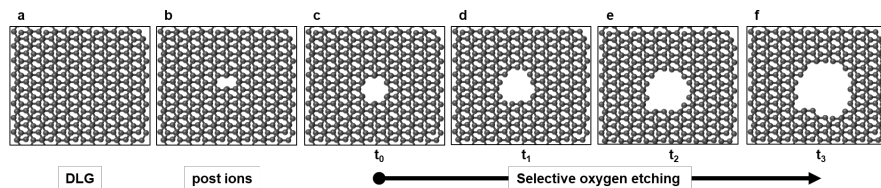


Figure 5.13: Pore formation schematic. A-B stacked double layer graphene (a) becomes defective upon ion impact with few atoms removed from the carbon lattice (b). During exposure to the selective oxygen etching conditions, edge atoms of graphene can react with oxygen to CO and CO_2 and thus gradually expand the pore size with prolonged etching time (c – f).

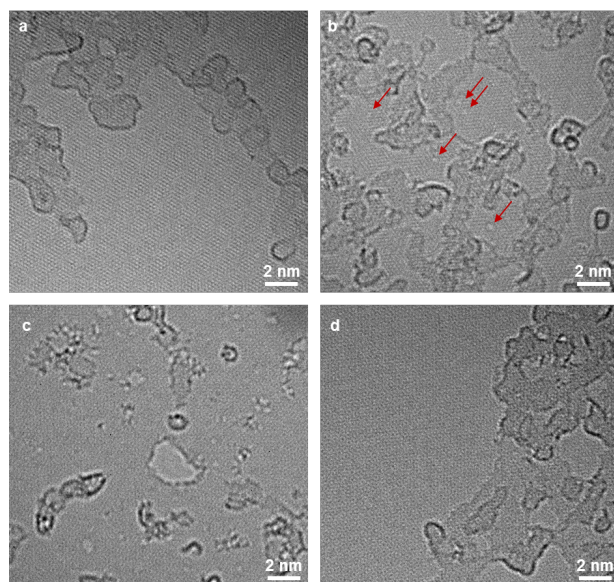


Figure 5.14: Additional TEM images of differently treated membranes. **a** DLG without atomic scale defects of lattice irregularities. **b** Ion irradiated DLG. Red arrows indicate atomically small defects. **c** Ion irradiated DLG after two hours oxygen etching. A ≈ 4 nm diameter nanopore has formed. **d** Control sample etched for two hours in oxygen without prior ion irradiation. No atomically small defects are found.

5. Scalable Manufacturing of Nanoporous Graphene Membranes

Each membrane was imaged by SEM in the following set of magnifications: 3500, 25000, 150000 and images were analyzed using ImageJ (**Figure 5.6**).¹⁴² The lowest magnification allowed imaging of the entire membrane area and ruling out ruptures down to a detection limit at this magnification of around 100 nm feature size. If such large ruptures were detected, they were sealed using local electron-beam-assisted platinum deposition in the focused ion beam (FIB) tool. The next higher magnification allowed detection of pinholes down to 30 nm in size; however, it was not feasible to image the complete membrane at this magnification level. Defects above the 30 nm threshold were analyzed, and their density and average size were used to estimate their total number and the total open area in the full membrane. Similarly, for the highest magnifications, the pores were detected down to a threshold of 2 nm equivalent diameter. With this approach, it is possible to compare the three different magnifications' total open area contributions. To reduce the uncertainty in the transport analysis of a certain pore size, only membranes with at least 80 % open area contribution from pores quantified in the highest magnification mode were used for 2 h etched membranes, while we sealed all observable defects and pinholes in membranes processed with shorter etching times.

5.2.3 Pore Density Control

Aside from the pore size control, a general fabrication platform also requires pore density control to enable porosity engineering for a given separation application. We chose ion irradiation to create nucleation centers for pores to expand during the dry oxygen etching process. Ion irradiation creates atomically small defects into 2D materials and thus serves as a method to generate the smallest defects.^{56,136,143} We studied atomic defect introduction using Raman spectroscopy to track increasing atomic-scale disorder within the material.^{144–146} Raman spectroscopy was performed using Renishaw inVia confocal Raman spectroscope.

5.2. Selective Nanopore Etching for Graphene Membranes

After optimizing the process parameters for selective graphene etching, defect creation by ion irradiation can be investigated further. Ions colliding with carbon atoms of graphene transfer momentum and if the displacement energy of $\approx 22 \text{ eV}$ ¹⁴⁷ is overcome, defects are created. Based on the ion conditions used in our study, atomic scale defects were expected and confirmed by TEM **Figure 5.12**.^{136,137,139} Raman spectroscopy provides insights about the atomic structure of graphene and its defects.^{144–146}

The Raman spectra of DLG membranes confirm low defect density (**Figure 5.15**). Gradually increasing the ion irradiation dose increases the D-peak intensity ($\approx 1350 \text{ cm}^{-1}$) compared to the G-peak intensity ($\approx 1580 \text{ cm}^{-1}$) since ions introduce defects into the crystal lattice. Two-hour etching at 300°C , 1 mbar expands the defects into nanopores (**Figure 5.15**). The Raman spectra after 2 h oxygen etching remain unaffected compared to bare ion irradiation confirming absence of additional defect introduction during etching.

The pore density increases linearly with the ion density confirming ion irradiation applicable for controlling pore density with up to 10^{15} m^{-2} pores (**Figure 5.16 a**). The average pore diameter of $5.5 \pm 1.3 \text{ nm}$ based on 19 samples is independent of ion dose (**Figure 5.16 b**). The high ion dose required to generate one nanopore agrees with recent studies of atomic scale irradiation damage in two-dimensional materials¹⁴³ and may originate from a combination of low sputter yield¹³⁸ and pore sizes below the detection limit.^{136,143}

The ability to independently tune the pore size of the membranes from the number of pores is the foundation for optimized membrane performance because the pore size determines membrane selectivity and the pore number the permeance. In this manner, two-dimensional porous membranes do not need to balance permeance and selectivity, as polymeric materials do, but instead, this trade-off can be circumvented, and performance can be maximized. With an average pore diameter of 5.5 nm after two-hour selective oxygen etching (5.11), and using a linear approximation, the pore growth rate is estimated to 0.046 nm/min. This low pore growth rate suggests short etching du-

5. Scalable Manufacturing of Nanoporous Graphene Membranes

rations capable of tuning pore sizes with angstrom-scale precision. If small enough, such pores may exhibit high selectivity for gas separation applications, while the permeance may be maximized independently by maximizing the number of pores. To obtain the highest permeance at a given pore size, we chose $5 \times 10^{17} \text{ m}^{-2}$ ion density. The resulting pore density of $\approx 5 \times 10^{14} \text{ m}^{-2}$ was the highest possible without creating larger ruptures into the freestanding graphene.

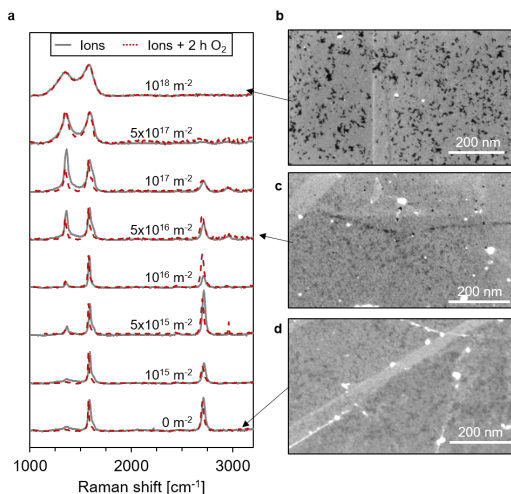


Figure 5.15: Controlling the pore density using the ion density. **a** Raman spectrum evolution for increasing ion irradiation dose before etching (grey) shows emergences of D-peak ($\approx 1350 \text{ cm}^{-1}$) due to atomic defects introduced into the material. Higher ion doses lead to loss of 2D peak intensity until DLG approaches a typical Raman spectrum of graphite. Raman spectra after oxidation (red, dashed lines) barely change compared to the ion only treatment. For intermediate ion doses, both, an increase in 2D intensity and decrease D intensity suggest an increase in lattice crystallinity. Post 2 h oxygen etching SEM images reveal increasing pore number density for increasing ion density (b, c, d).

5.2. Selective Nanopore Etching for Graphene Membranes

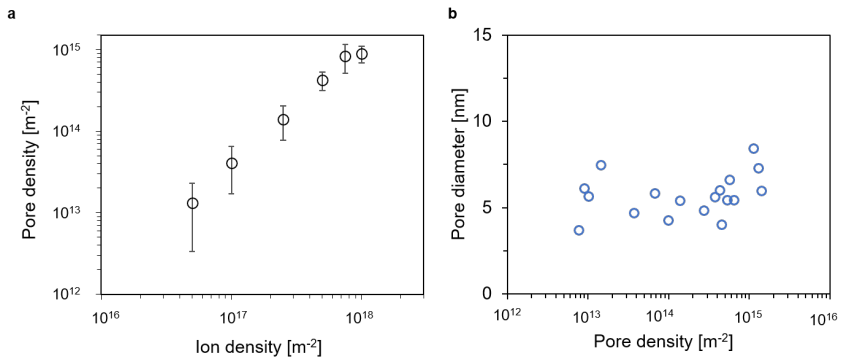


Figure 5.16: Pore density control. **a** Relationship between pore density after 2 h etching with pore density increasing linearly with ion density. **b** Average pore diameters of 2 h etched samples for various pore densities. The average pore size is decoupled from the pore density and thus independently controlled from the ion density.

Chapter 6

Gas Transport at the Limit of Atomic Thinness

This section is published in parts as:

Karl-Philipp Schlichting and Dimos Poulikakos. “*Selective Etching of Graphene Nanopores: From Molecular Sieving to Extreme Permeance*” *ACS Applied Materials & Interfaces*, **2020**, 12(32), 36468-36477, DOI:<https://doi.org/acsami.0c07277>

6.1 Gas Transport Characterization

The membrane fabrication approach is particularly interesting for the study of gas separation due to the inherent need for sub-nanometric pores, which is congruent with the approach of increasing pore size from the smallest possible to a few nanometers.

We developed a crossflow setup with various feed gases to study gas transport through the fabricated membranes and analyzed the perme-

6. Gas Transport at the Limit of Atomic Thinness

ation using a calibrated mass spectrometer.

6.1.1 Calibration

Gas permeation and mixture separation were analyzed using a mass spectrometer (MS) (Cirrus 2, MKS Instruments) and gases (Carbagas) with gas purities 5 or higher. The gas mixing and calibrations were carried out using mass flow controllers (MKS Instruments) in a custom build setup (**Figure 6.7**). The lower detection limit of the system was determined to be near 1 ppm. All experiments were carried out at signal-to-noise ratios above 5, and the relative error in the measurements due to signal variation, calibration, feed composition, and pressure was estimated employing error propagation to be less than 10 % for all permeance measurements and less than 20 % for all selectivity measurements (**Figures 6.4, 6.5**).

Gas permeation and separation experiments were carried out in a custom-made setup, with the membrane clamped into a custom-made fixture (**Figure 6.7**). All experiments were performed in crossflow conditions. The permeance Φ of gas i was calculated according to

$$\Phi_i = \frac{Q_{Ar}}{\Delta P_{tot} A_{mem}} \times \frac{C_{(i,permeate)}}{C_{(Ar,sweep)}} \quad (6.1)$$

With the sweep flow rate Q_{Ar} , the total pressure partial difference ΔP_{tot} of gas i , A_{mem} being the membrane area, and $C_{(i,perm)}$ the detected concentration of gas i in the permeate and the concentration of argon in the sweep gas $C_{(Ar,sweep)}$. Four feed gases (Carbagas, purity 5 or higher) were analyzed, and their flow rates were controlled using mass flow controllers (MFCs) (MKS Inst.). Two manometers, one at the feed side and one at the permeate side of the membrane, were used to measure the pressure difference across the membrane and

6.1. Gas Transport Characterization

toward the environment. The permeate gases were diluted and swept away in argon carrier gas, from which the mass spectrometer (MS) detected the composition (**Figure 6.2, 6.3**).

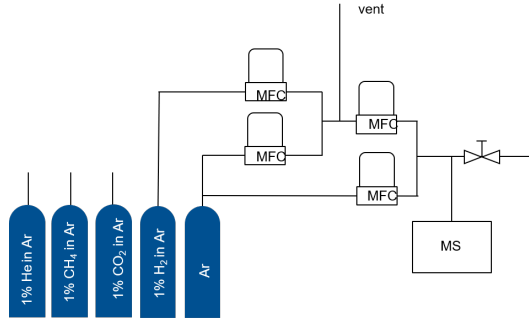


Figure 6.1: Setup calibration. The calibration setup always consists of one feed gas connected to a mass flow controller. The feed gases are diluted to 1 % in Argon. The gas of interest can be diluted twice subsequently allowing calibration from 1 % to 1 ppm. Various concentrations can thus be produced and the connected MS response is recorded to obtain calibration curves of all gases.

The MS was operated using the multiplier detector and was calibrated using pre-diluted gas mixtures with an adjusted configuration of the MFCs (**Figure 6.7**). The adjusted calibration allowed to control the composition sampled by the MS, enabling adjustment from 1×10^4 ppm down to 1 ppm within the control limits of the MFCs. All gas calibration curves show a power-law dependence ($C_{(i,perm)} = \alpha C_{(MS,detection)}^\beta$) of the detected signal in MS $C_{(MS,detection)}$ compared to the feed concentration. To avoid cross-detection effects, the mass-to-charge ratio peak of 15 was used for methane calibration and later detection in the experiments. All calibration experiments show very accurate regression statistics ($R^2 \geq 0.999$) and the exponents close to unity, showing linear behavior (**Figure 6.2, 6.3, Table 6.1**). The average discrepancy of the calibrated signal compared to the feed concentration is around 1 % for all single gases, which is within the uncertainty stemming from the mass flow controllers (Table 6.2).

6. Gas Transport at the Limit of Atomic Thinness

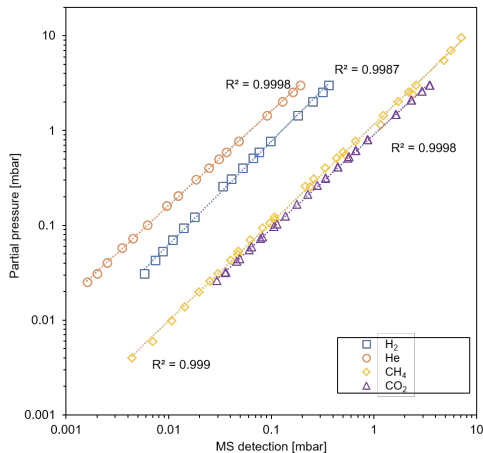


Figure 6.2: Calibration of single gases. Single gas calibration curve down to the detection limits of the MS system. He (orange circles), H_2 (blue squares), CH_4 (yellow diamonds), and CO_2 (purple triangles) follow a power law relation of detected MS signal and partial pressure of the respective gas fed into the MS

Furthermore, we investigated the possibility of interference of gas signal detection for gas mixture experiments, despite all experiments and calibrations being diluted to $\leq 1\%$ vol in argon flow on the permeate side (**Figure 6.3**). Indeed, the obtained curves overlap each other irrespective of the presence of another gas, as expected from the high dilution in Ar , the working principle of the MS and the use of mass-to-charge-ratio 15 for CH_4 calibration. The average relative errors and standard deviations for various mixtures compare to the single gas calibration stay below 10%, with only H_2 in H_2/He mixtures showing 23% average deviation. Given the accurate description of the gases using calibrations from single gas experiments, we decided to accept the higher deviation of the He in hydrogen mixtures and applied the single gas calibration curves for all experiments. The extracted calibration coefficients for each gas enable the calculation of the real permeate partial pressure for each gas from the signal detected by the MS. This allows the computation of mixture calibration factors as well

6.1. Gas Transport Characterization

as tracking individual permeances within mixtures of gases. All experiments were carried out within the calibrated concentration ranges.

	Gases				
	H_2	He	CH_4	CO_2	
α	9.41	15.95	1.15	0.90	
β	1.09	1.00	1.03	1.00	
R^2	0.999	1.000	0.999	1.000	

Table 6.1: R^2 values and calibration constants for single gases. Each calibration curve corresponds with high precision and negligible differences to the experimental points with $R^2 \geq 0.999$ for all gases. The close to unity exponents β reveal almost linear dependence of MS signal to gas partial pressure.

Gas 1	Gas 2				
	H_2	He	CH_4	CO_2	
H_2	-1 ± 5	8 ± 4	-4 ± 2	6 ± 2	
He	23 ± 9	-1 ± 2	–	–	
CH_4	-5 ± 6	–	1 ± 7	-1 ± 2	
CO_2	-2 ± 5	–	6 ± 2	-1 ± 2	

Table 6.2: Signal deviation in presence of other gases. Relative changes in calibration curves if other gases are present. These relative errors can be attributed to the MFC accuracies involved in dynamically mixing the gases.

The measurements of gas transport, as well as the quantification of the geometric membrane properties using SEM, are subject to measurement uncertainties. We incorporated the propagation of uncertainty toward the results using linear propagation of uncertainty according to equation 6.2.¹⁴⁸

$$\sigma_F^2 = \sum_{j=1}^N \left[\left(\frac{\partial F}{\partial x_j} \right)^2 \left(\frac{\sigma_{x_j}}{n_{x_j}} \right)^2 \right] \quad (6.2)$$

For SEM quantification, the uncertainties in measured pore areas and pore number counts per image, total membrane area, are considered.

6. Gas Transport at the Limit of Atomic Thinness

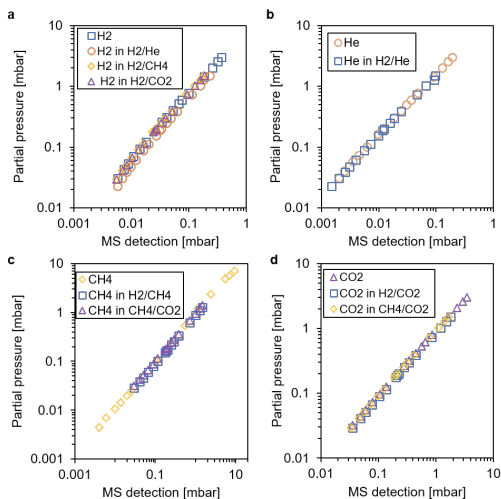


Figure 6.3: Mixture gas calibration. Calibration results in presence of other gases (at maximum 1%, as will be the case in real experiments due to sweep *Ar* dilution) show negligible to undetectable deviations compared to the single gas calibration curves in a. **a** H_2 single gas (blue squares), H_2 in H_2/He mix (orange circles), H_2 in H_2/CH_4 (yellow diamonds), H_2 in H_2/CO_2 (purple triangles). **b** He single gas (orange circles), and He in H_2/He mix (blue squares). **c** CH_4 single gas (yellow diamonds), CH_4 in H_2/CH_4 (blue squares), CH_4 in CH_4/CO_2 (purple triangles). **d** CO_2 single gas (purple triangles), CO_2 in H_2/CO_2 (blue squares), CO_2 in CH_4/CO_2 (yellow triangles). The differences are minute and negligible.

For MS quantification, the uncertainties from feed and sweep mass flow controllers, manometers, calibration constants (α and β), and MS raw signal are considered. The propagation of errors leads to less than 10 % relative error for permeance measurements and around 10 % relative error for calculation of mixture separation factors, with the largest contribution of uncertainty stemming from the calibration constants (**Figure 6.4, 6.5**). Variations in the detected signals from the MS or the feed flow rates and pressure conditions contribute less than 2 % relative error the uncertainty.

6.1. Gas Transport Characterization

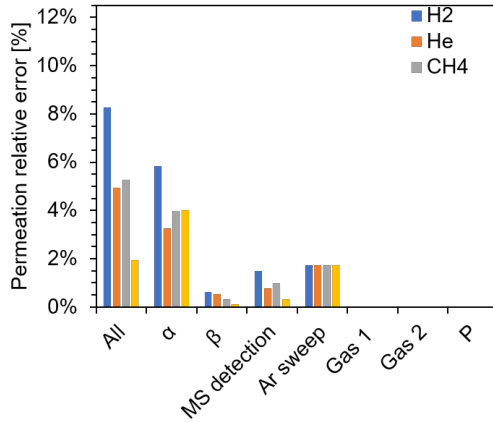


Figure 6.4: Error propagation permeance. Example of sensitivity analysis of factors influencing measurement uncertainty. The relative errors in permeation measurements are below 10 % of the measured value. The calibration factor α and the argon sweep flow rate contribute the most to measurement uncertainty with around 5 % and 2 %

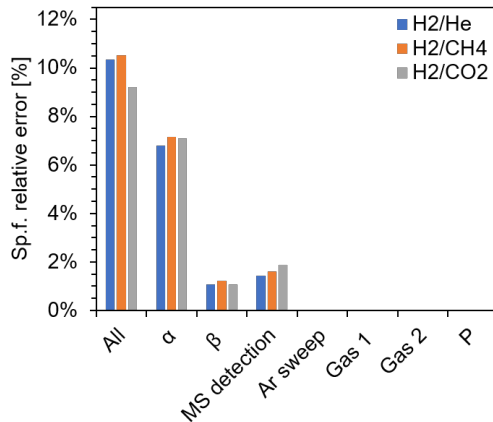


Figure 6.5: Error propagation analysis in separation factor. Mixture separation factor uncertainty is around 10 % of the measured value with the calibration factor α contributing the most

6. Gas Transport at the Limit of Atomic Thinness

6.1.2 Experimental Setup & Control Experiments

Gas permeation and separation experiments were carried out in a custom-made setup with the freestanding graphene membrane supported by a silicon nitride frame clamped into a custom-made fixture (**Figure 6.6 b**). All experiments were performed in cross-flow conditions where a single gas or a mixture of two gases was fed into the fixture and flown over the freestanding graphene membrane. Part of the feed flow is transported across the membrane, while most leaves again as retentate to reduce possible effects of concentration polarization. The bottom side of the membrane is exposed to an argon carrier sweep flow to dilute the membrane transport again to reduce concentration polarization, and the combined membrane transport and sweep flow exit the fixture as permeate stream and are subsequently analyzed in a calibrated mass spectrometer.

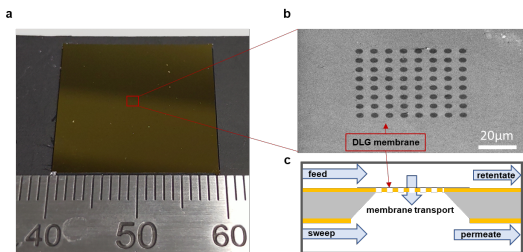


Figure 6.6: Membrane visualization and flow description. **a** The freestanding DLG graphene membranes are supported by a holey silicon nitride frame in a 2×2 cm chip. **b** Tiled view SEM image show the DLG membrane spanned over an array of 64 holes in the support nitride frame. **c** The schematic cross-sectional side view of the graphene membrane is supported by the holey frame with feed flow entering the fixture on the left and flowing over the membrane to leave as retentate. The bottom side of the membrane has argon sweep gas diluting the membrane transport and leaves the fixture as a permeate mixture, which is subsequently analyzed in a calibrated mass spectrometer.

The 150 nm thin support of holey Si_3N_4 with $4 \mu\text{m}$ or $6 \mu\text{m}$ hole arrays enable to attribute measured permeance to the graphene membranes exclusively.

6.1. Gas Transport Characterization

The experiments were carried out by sequentially exposing the membranes to flows of the individual gases or mixtures. At the end of a specific membrane measurement, the initial gas transport experiment was repeated to test for potential changes of the membrane during the experiment. Most membranes show less than 10 % differences in permeance even after 24 h of permeation experiments suggesting stable pore sizes and absence of membrane degradation during operation similar to other recently published studies (**Figure 6.8**).¹²¹

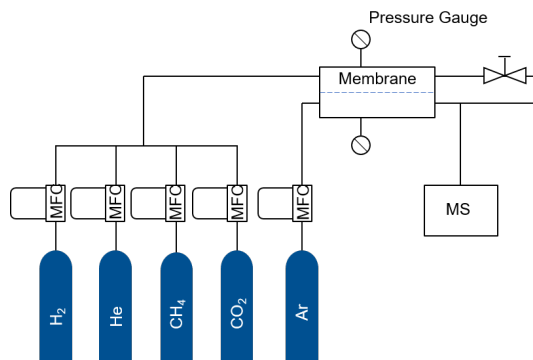


Figure 6.7: Measurements setup. Measurement setup for single and mixture gas permeation and separation analysis at various crossflow rates and feed gas pressures. Four gases (H_2 , He , CH_4 , CO_2) can be individually controlled via a mass flow controller and are flown across the membrane surface. The pressure relative to the environment is monitored with a manometer and the retentate line contains a needle valve for control of pressure drop across the membrane. Argon is flowing on the permeate side of the membrane sweeping the permeated feed gases toward the mass spectrometer.

The crossflow experiments were carried out varying the feed gas flow rate to detect potential influences on permeance and mixture separation factors stemming from the feed flow toward the membrane (**Figure 6.10**). Within the accuracy of our setup, no influence such as concentration polarization can be observed on either the permeance or the mixture selectivity.

6. Gas Transport at the Limit of Atomic Thinness

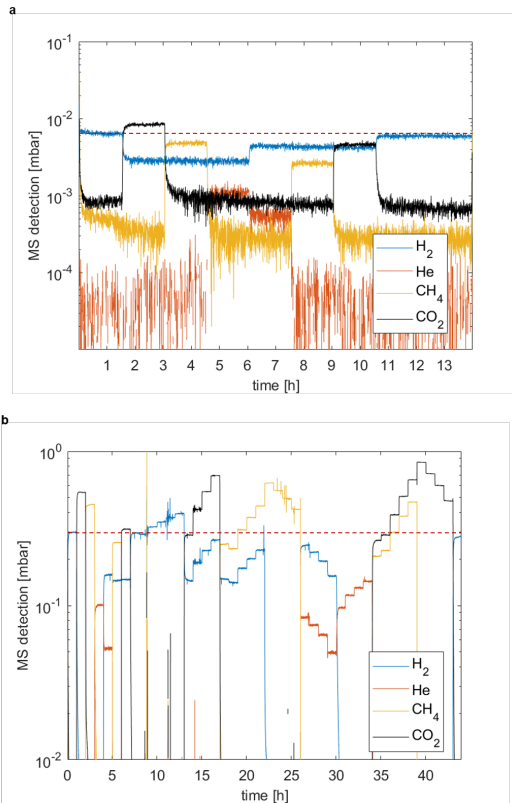


Figure 6.8: Exemplary MS signal of measurements. **a** Detected signal for a DLG membrane displaying stable permeation over 13 h permeation with initial hydrogen and final hydrogen signal deviating by less than 10 % (red dashed line). Baseline value for the different gases show high signal to noise ratio even for DLG membranes. **b** Detected signal for a two hours oxygen etched membrane during a pressure study series lasting 44 h. Again, initial hydrogen and final hydrogen signals deviate less than 10%.

6.2 Transport Analysis

6.2.1 Single Gas Transport

Despite using graphene with low defect density and stacking two layers independently, both of which reduce leakages and increase fabrication

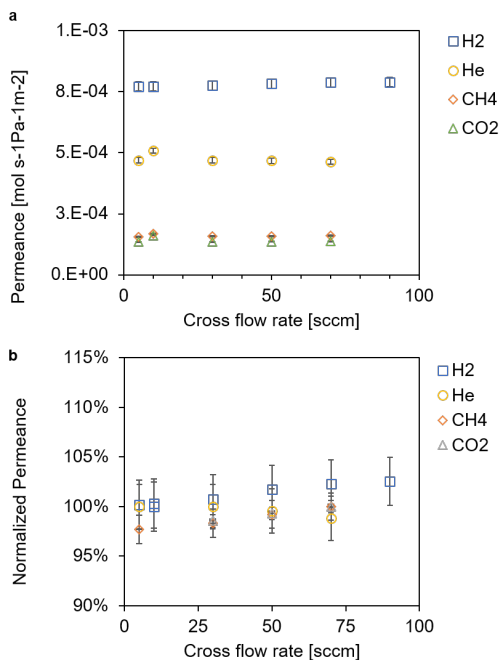


Figure 6.9: Cross flow experiments. **a** Single gas permeance as function of feed-flow rate. **b** Mixture selectivity as function of cross flow rate. Neither the permeances nor the mixture separation factors show a detectable dependence on the crossflow rate.

yield, the DLG membranes are permeable to gases (**Figure 6.12**). The total membrane available for permeation of gases consists of 64 circular holes of 4 μm diameter in the silicon nitride frame, giving a total freestanding graphene membrane area of around 800 μm^2 to probe gas transport. Control experiments using non-hole silicon nitride frames indeed show no measurable transport opposed to DLG, ruling out potential other transport pathways than the DLG itself.

Irradiating these membranes with ions increases their hydrogen permeance $\Phi(H_2)$, the molar flux normalized by the partial pressure difference, by less than a factor of two relative to DLG (before ion irradiation), revealing the ion-induced defects slightly permeable. This

6. Gas Transport at the Limit of Atomic Thinness

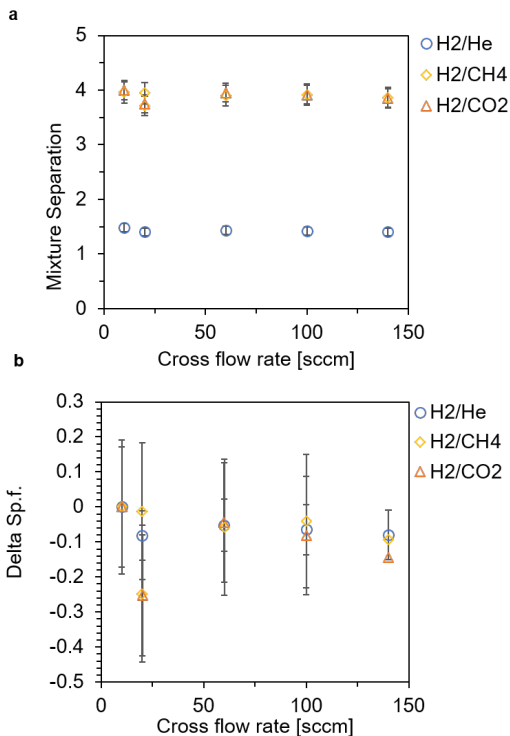


Figure 6.10: Mixture selectivity as function of cross flow rate. Neither the permeances nor the mixture separation factors show a detectable dependence on the crossflow rate.

also demonstrates ion irradiation alone to be insufficient as a tuning parameter to enhance membrane permeance, and this regarding both desired permeance levels and desired flexibility.

Subsequent 15 min etching of the membranes increases their hydrogen permeance around one order of magnitude by expanding the defects into pores with hydrogen permeances exceeding $10^{-4} \text{ mol s}^{-1} \text{ m}^{-2} \text{ Pa}^{-1}$. Etching for two hours leads to a further increase in hydrogen permeance to unprecedented levels ($> 1 \times 10^6 \text{ GPU}$) for a porous 2D mem-

branes with 5.5 ± 1.3 nm average diameter and $1.6 \pm 0.6\%$ membrane porosity. The permeation of CO_2 molecules per pore of these membranes is $21 \pm 6 \times 10^{-4} \text{ s}^{-1} \text{ Pa}^{-1}$, near the prediction of recent molecular dynamics simulations for a single 5 nm pore ($\approx 80 \times 10^{-4} \text{ s}^{-1} \text{ Pa}^{-1}$).¹³⁰ Control experiments of DLG merely exposed to two hours of etching reveals nearly constant permeance and thus further establishes the developed selective etching method to control pore number and pore size independently. The measurement of different gases sheds light on the permeation mechanism. Transport is in the free molecular flow regime with Knudsen numbers, the ratio of molecular mean free path to the pore diameter, typically $Kn > 10$.

Effusion, the model for molecular gas flow, J , across an infinitely thin aperture with area A , for transport driven by a partial pressure difference, P , was derived by Knudsen from the kinetic theory of gases assuming an ideal gas consisting of point particles without intermolecular forces²²

$$J = \frac{AP}{\sqrt{2\pi MRT}} \quad (6.3)$$

with the molecular weight M of the gas, the universal gas constant R , and temperature T . Comparing the permeance $\Phi = J/P$ for each gas, i , after ion irradiation and 15 min oxygen etching relative to the permeance of the same gas across the untreated DLG membrane Φ_{DLG} (i.e. $\Phi_{(i,ions)}/\Phi_{(i,DLG)}$ and $\Phi_{i,ions+15'}/\Phi_{(i,DLG)}$) enables studying the effect of ion irradiation and short oxygen etching (**Figure 6.13**). Based on effusion theory, the relative increase in permeance is independent of the gas molecule and equal to the ratio of available open area for passage:

$$\frac{\Phi_{ions}}{\Phi_{DLG}} = \frac{A_{ions}}{A_{DLG}} \quad (6.4)$$

6. Gas Transport at the Limit of Atomic Thinness

We measured the permeance of hydrogen, helium, methane, and carbon dioxide across membranes before and after ion irradiation at room temperature and 1 bar partial pressure difference. The relative increase in permeance upon ion irradiation is different for each gas, ruling out effusive transport. Instead, the assumption of point particles in effusion theory may not hold as the molecules have different kinetic diameters, which is expected for similarly-sized pores. Such sub-nm-sized defects are also known to occur for single-layer graphene (SLG) with the used ion conditions in this study.¹³⁶

Treatment of DLG with ions leads to a preferential increase in *He* permeance compared to hydrogen and carbon dioxide (CO_2). This is a signature of the molecular size selectivity of the created defects toward the different gas molecules' kinetic diameters. Thus, the created defects are mostly smaller than the kinetic diameter of CO_2 (0.33 nm).

Surprisingly, CH_4 permeance increases consistently more than that of CO_2 upon ion irradiation, despite CH_4 having a larger kinetic diameter d_{kin} ($d_{kin}(CH_4) = 0.38$ nm; $d_{kin}(CO_2) = 0.33$ nm).⁴⁰ Here another mechanism of transport reduces the passage barrier of CH_4 relative to CO_2 . Different chemical interaction at the pore edge may cause different interaction with the molecules, a topic subject to intense theoretical investigation and debate.^{25,27,30,31,124,127,127,128} The defects may become functionalized with oxygenated functional groups due to exposure to ambient air between treatment and gas measurement. Due to their different charge distribution within the molecules, hydrogen atoms of methane could come closer to the pore edge functional group than oxygen atoms of CO_2 , if the pore functional group is negatively charged.^{31,124}

Molecular dynamics simulations indeed predicted preferential passage of CH_4 over CO_2 for sub-nm pores with negatively charged pore rims.¹²⁷ Hence, pores in graphene may pose smaller permeation barriers for methane compared to CO_2 .

Subsequent 15 min etching increases the relative gas permeances significantly. Hydrogen permeance increases almost one order of magnitude, while Helium permeance increases six-fold. Furthermore, methane increases five-fold and CO_2 merely three-fold. Consequently, transport remains non-effusive, and the dimensions of the pores are near the kinetic diameters of the molecules. This is in line with absence of detectable pores using SEM imaging (**Figure 6.11**). Despite having a larger kinetic diameter, molecules containing hydrogen atoms (H_2 , CH_4) exhibit enhanced permeation compared to the respective next smaller molecule without hydrogen atoms (He , CO_2), further indicating chemical affinity to affect permeation. Thus, the pores after 15 min etching, sieve CO_2 from hydrogen and helium, and the data implies that the energy barrier for methane is reduced as a result of pore edge chemistry.

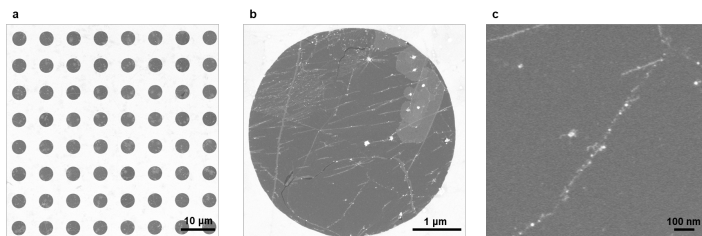


Figure 6.11: SEM images of ions and 15 min selective oxygen etching do not display detectable pores, requiring pore sizes below the detection limit of $\approx 3nm$ equivalent diameter.

The permselectivities of the membranes for different treatments can thus be constructed (**Figure 6.14**). DLG indeed shows molecular sieving characteristics with permselectivities significantly above the Knudsen diffusion limits (H_2/He : 1.41, H_2/CH_4 : 2.83, H_2/CO_2 : 4.69) for H_2/CH_4 and H_2/CO_2 gas pairs, with permselectivities of ≈ 7.5 for H_2/CH_4 , obtained from the square root of the inverse ratio of the molecular weights from effusion theory.

While permselectivity of H_2/CH_4 decreases upon ion irradiation, it increases for He/CO_2 despite CH_4 having a larger kinetic diameter

6. Gas Transport at the Limit of Atomic Thinness

than CO_2 . This highlights the importance of pore chemistry on the molecular passage for sub-nm pores. Etching for 15 min further increases the permselectivity of H_2/CH_4 and H_2/CO_2 pairs. For ion irradiation followed by 15 min selective oxygen etching, the membranes display H_2/CH_4 permselectivity above 6 at hydrogen permeance of above 1×10^{-4} mol/s/Pa/m².

Increasing the H_2/CO_2 permselectivity from ≈ 4 to ≈ 7 upon pore expansion by 15 min selective oxygen etching reveals the enhanced contribution of transport through pores that permeate hydrogen but not carbon dioxide and thus increase the permselectivity. The increase in permselectivity upon 15 min of oxygen etching to molecular sieving values reveals further the pore size increment within these 15 min to be larger than the kinetic diameter of helium and hydrogen, but smaller than the kinetic diameter of carbon dioxide. Therefore, ion irradiation to nucleate defects followed by 15 min oxygen etching leads to an expansion of defects into permeable pores with angstrom-scale precision in pore size increment. Consequently, the selective oxygen etching increases the membrane permeance by one order of magnitude and simultaneously increases the permselectivity well within the molecular sieving regime. The increase in permselectivity above the Knudsen diffusion limit supports the developed oxygen etching technique capable of tuning the pore size near the size differences of the studied molecules with angstrom-scale precision.

Etching the graphene edges in an oxygen-containing atmosphere can introduce carbonyl groups during the etching process and locally introduce strong electric fields due to variation in charge distribution.^{122,124,141} This chemical functionalization was theoretically predicted to affect molecular permeation via energy barriers for permeation, adsorption at the pore edge, and graphene surface due to altered electrostatics.^{31,34,124,149} We thus conclude that the stronger enhancement of permeation of methane over carbon dioxide may stem from the preferential interaction of methane molecules with oxygen-functionalized pores due to favorable electrostatic attraction compared to carbon dioxide.

Etching duration of two hours causes a reduction of permselectivity of all gas pairs due to a substantial increase of effusive transport contribution, as expected for pores roughly ten times in diameter as the gas molecules.

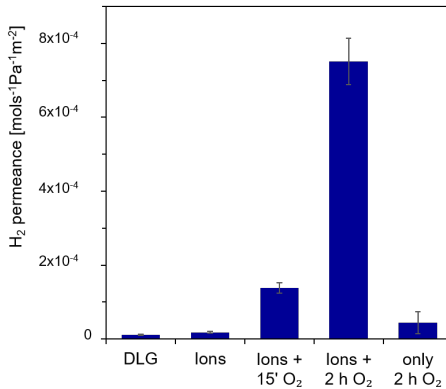


Figure 6.12: H_2 permeance evolution with treatment. Evolution of hydrogen permeance with different treatments shows an increase upon ion irradiation and further increase of permeance by orders of magnitude for oxygen etching of different treatment durations. Pure oxygen etching, without prior defect creation does not increase membrane permeance significantly.

6.2.2 Mixture Gas Transport

While the permselectivity analysis sheds light on pore size and the importance of chemical interaction for molecular-sieving-sized pores, it represents an idealization compared to gas separation applications. Therefore, mixture gas experiments were carried out for pairs of He/H_2 , H_2/CH_4 , and H_2/CO_2 (**Figure 6.15**). DLG membranes show molecular sieving of mixtures of H_2/CH_4 and H_2/CO_2 while He/H_2 is not

6. Gas Transport at the Limit of Atomic Thinness

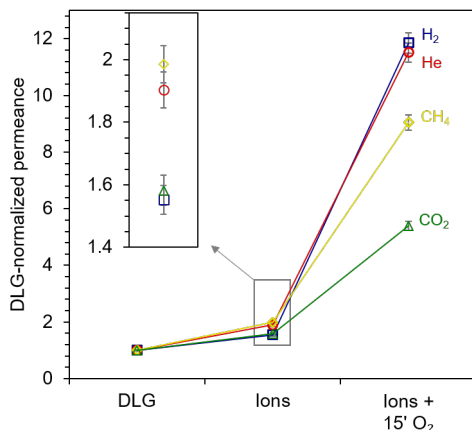


Figure 6.13: Single gas permeance evolution for various treatments. Evolution of permeance normalized to DLG permeance for different gases, respectively, with hydrogen (blue squares), CH_4 (yellow diamonds), helium (red circles), and CO_2 (green triangles). Each gas increases differently relative to its prior value indicating the insufficiency of effusion alone to describe transport and suggesting molecular effects of permeation to dominate transport.

sieved. This is in line with pores smaller than CO_2 . The mixture selectivities, Ψ , decrease upon treatment with ions, and subsequent etching toward values below Knudsen selectivity for H_2/CO_2 and H_2/He for 5 nm pores, agreeing with a gradual transition to lower selectivity for larger pores. The differences between permselectivity and mixture selectivity reveal molecular interaction during the separation of the gases. This interaction occurs either within the volume near the membrane or at its surface. Surface diffusion as a parallel pathway to direct gas-phase passage is theoretically predicted.^{25,26,28–30,30,33,130,150} In a gas mixture, molecules can adsorb competitively at the membrane, reducing the amount of each adsorbed species compared to a single gas situation. Stronger adsorption is predicted for gases such as CH_4 and CO_2 compared to H_2 and He .^{26,27} The permeance of each gas is then equal or smaller compared to the single gas situation. Hence, competitive adsorption is expected to reduce selectivity in a mixture

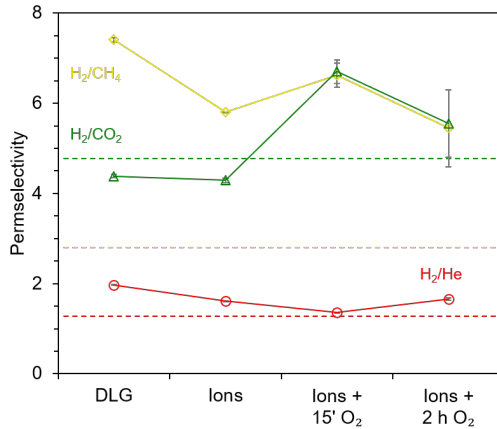


Figure 6.14: Evolution of permselectivities. Ion irradiation typically decreases permselectivities in favor of the larger gas, however oxygen etching of 15 min can increase the selectivity values. Long oxygen etching shows a decline in selectivities in line with loss of molecular sieving properties for 2 h oxygen etched membranes having 5.5 nm average pore size.

for pairs such as H_2/CH_4 , H_2/CO_2 . Another possibility to reduce the mixture selectivity is the transfer of linear momentum of colliding molecules.¹⁵¹⁴⁶ In this case, the permeance of the heavier species increases compared to the single gas case, while the permeance of the light species decreases. The hydrogen permeance of two-hours-etched membranes within different gas mixtures normalized by its single gas permeance indeed reveals a reduction in hydrogen permeance, which changes proportionally to the molecular weight of the mixture partner (**Figure 6.16**). Importantly, the permeance of the heavier gas in mixtures with hydrogen increases above its single gas permeance and proportionally to the difference in molecular weight (**Figure 6.16**). This behavior identifies the transfer of linear momentum from the light to the heavy gas in the volume near the pore of a two-dimensional membrane to cause the differences between permselectivities and mixture selectivities for membranes with 5.5 nm average pores size.

6. Gas Transport at the Limit of Atomic Thinness

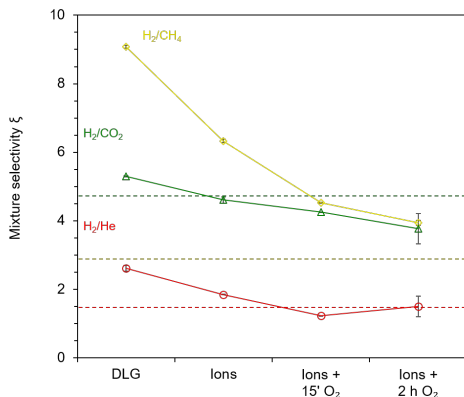


Figure 6.15: Variation in mixture selectivity. Treatments decrease mixture selectivity and the individual mixture selectivities differ from the permselectivities revealing gas mixture interaction.

Overall, the transport across membranes exposed to different treatments cannot be rationalized by a single dominating mechanism, such as size-based molecular sieving toward weight-based effusion. Instead, it is a complex process where pore chemistry and molecular interaction markedly influence the permeation of gases.

6.2.3 Pressure Effects

Another means to study the transport mechanisms and a step toward more realistic conditions is applying a pressure drop, ΔP , and variation of the crossflow conditions. While permeance and selectivity are unaffected by the cross-flow rate (**Figure 6.9**), pressure application across 5 nm membranes leads to a variation of permeance proportionally to the pressure drop, except for helium (**Figure 6.17**). Since the permeance of helium is independent of pressure, helium permeates purely effusive. Furthermore, the constant helium permeance allows

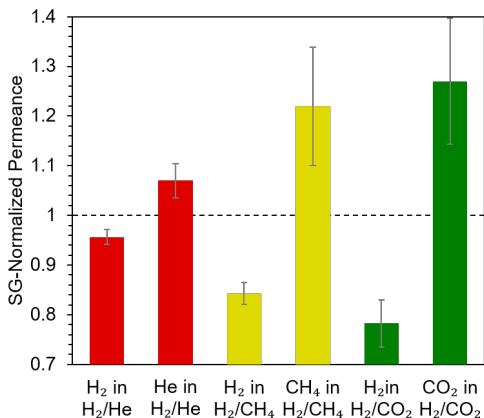


Figure 6.16: Permeance changes due to mixture effects. Permeance of each gas the presence of other gases for 2 h oxygen etched membranes, normalized by its SG permeance. Hydrogen permeance decreases in the presence of other gases, proportionally to the molecular weight of the other gas. Similarly, *He*, *CH₄*, and *CO₂* show higher permeance in mixtures with hydrogen. This observation shows transfer of linear momentum from the light and fast gas to the heavier and slower gas near the membrane pores.

for ruling out possible pore expansion due to stretching of the membrane during pressure application.

The other gases, however, display pressure-dependent permeance, implying the presence of another transport pathway. Surface diffusion is predicted to occur for adsorbing gases proportional to the gas pressure.¹³⁰ We attribute surface diffusion to the pressure-dependent permeances as predicted theoretically, revealing yet another aspect of the rich permeation behavior of gases across nanoporous graphene membranes.³³

Furthermore, we also studied the change in mixture selectivity when increasing the pressure drop across the membrane (**Figure 6.18**). Increasing the pressure drop reduces the mixture selectivity for gases with a large molecular weight ratio, while the separation factor in gas pairs with a small molecular weight ratio stays mostly unaffected. These results further underpin the importance of the transfer of lin-

6. Gas Transport at the Limit of Atomic Thinness

ear momentum in gas mixture separation across porous membranes of graphene and likely other two-dimensional materials as well.

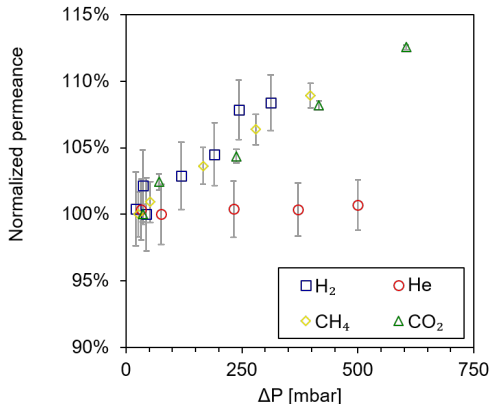


Figure 6.17: Pressure drop effect on permeance and separation. Single gas permeance as function of total applied pressure drop ΔP . Helium (red circles) permeance is unaffected confirming helium to permeate in a purely effusive manner. The other gases hydrogen (blue squares), methane (yellow diamonds) CO_2 (green triangles) show increasing permeance with higher pressure drop. This reveals an additional transport pathway across the nanopores apart from effusion.

6.2.4 Membrane Performance Assessment

Ultimately, any membrane performance is characterized by its selectivity *versus* permeance trade-off (**Figure 6.19**). The membranes fabricated in this study exhibit unprecedented hydrogen permeance of up to 1×10^7 GPU surpassing state-of-the-art membranes and the upper-bound of polymers by up to three orders of magnitude at similar H_2/CH_4 selectivity of ≈ 3.8 . Increasing selectivity to molecular sieving levels is achieved with membranes exposed to short etching in agreement to the theoretically predicted upper bound for permeation

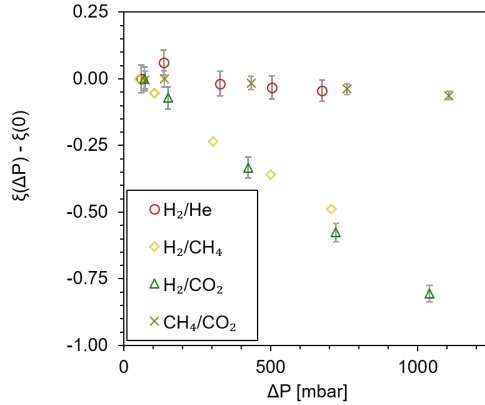


Figure 6.18: Change in mixture selectivity due to mixture gas effects. Variation of mixture selectivity with change in applied pressure drop. Mixture selectivities of H_2/CH_4 and H_2/CO_2 decrease for higher applied pressures (H_2/He red circles, H_2/CH_4 yellow diamonds, H_2/CO_2 green triangles, and CH_4/CO_2 dark green crosses).

across a 2D porous membrane material with $\approx 1 \times 10^{15} \text{ m}^{-2}$ pore density.¹²⁹

6. Gas Transport at the Limit of Atomic Thinness

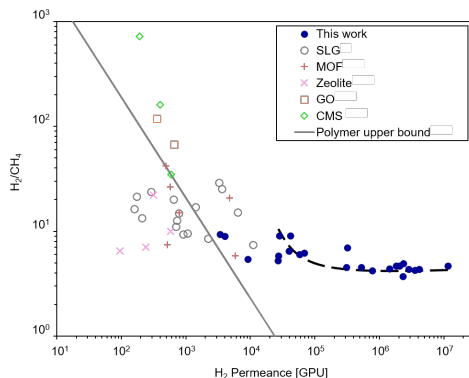


Figure 6.19: Figure of merit of hydrogen-methane separation. The full blue circles represent all studied membranes where from left to right corresponds to DLG, ion irradiation, followed by increasing oxygen etching duration in the range from 15 min to 2 h. Robeson upper bound (1 μm thick selective layer)^{49,152} for hydrogen methane separation. Atomically thin porous graphene shows superior performance compared to state-of-the-art polymers with different permeation-separation characteristics stemming from the permeation mechanisms across nanopores in graphene. Up to three orders higher permeance for two-hour oxygen etched membranes is possible at similar selectivity with other state-of-the-art membranes (SLG⁴⁰, Metal-organic frameworks (MOF)^{153,154}, zeolites^{155,156}, graphene oxide (GO)^{157,158}, carbon molecular sieves (CMS)^{159,160}. Increased selectivities can be obtained for a reduction in oxygen etching duration at the cost of markedly reduced permeance with up to 9.3 H_2/CH_4 selectivity with 30 000 GPU membranes. The black dashed line indicates the 2D-membrane upper bound for pore densities of $5 \times 10^{14} \text{ m}^{-2}$ and hydrogen permeation across a 2D membrane.

6.3 Conclusions

In conclusion, we have developed and optimized a two-step dry etching procedure to create large-scale graphene membranes with decoupled pore size and density control. Energetic ion irradiation of graphene followed by dry and scalable etching in oxygen at 1 mbar and 300 °C, selectively transforms ion-induced defects to larger nanopores resulting in a method of independent control of pore density and pore size. The decoupled pore number and pore size control allow for optimization of permeance and selectivity independently, and the study of the dominating separation mechanisms for different pore sizes. Membranes

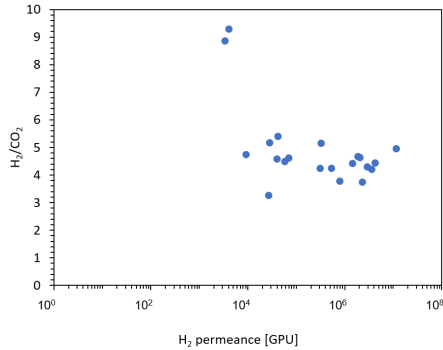


Figure 6.20: Figure of merit for H_2 - CO_2 separation. Permeance-selectivity trade-off for separation of hydrogen from mixture with carbon dioxide for various membranes from DLG to 2 h etched membranes.

with up to three orders of magnitude higher permeance than previously reported at similar selectivity and membranes with moderate permeance but higher selectivity in the molecular sieving regime were fabricated and tested. Etching for 15 min enables angstrom-scale control over pore size leading to permeance increases of small gases by up to one order of magnitude and simultaneously increasing the membrane selectivity. We show that gas transport through the nanopores is affected collaboratively by molecular size, chemical affinity, surface diffusion, effusion, and the transfer of linear momentum in mixtures. The method presented here enabled the fabrication of large-scale nanoporous graphene membranes by independently tuning selectivity and permeance, which could also be characterized by investigating the various complex facets of gas permeation and separation. We believe these membranes to be a promising technology for a range of separation applications from osmosis to ultrafiltration.

Chapter 7

Scaling-Up to cm²-Scale

The separation of fluid mixtures often utilizes membranes due to continuous operation, compact modules.⁴ Currently, however, large-scale separation processes largely rely on distillation, which requires vast amounts of energy that could potentially be reduced to a tenth if better membranes can replace phase-change-based separation processes.¹ To overcome current membrane technology limitations, it has been a long-standing goal to reduce membrane thickness to enable more efficient separation processes.^{152,161} Recently, it was shown that for liquid separation and filtration processes, the ideal membrane thickness is, in fact, not infinitesimally thin but having a pore size to membrane thickness ratio near one.¹³⁹ While polymeric materials are intrinsically limited to a trade-off between thickness and selectivity,¹⁵² graphene, the two-dimensional crystal of carbon, provides the thinnest material possible with simultaneously high mechanical, chemical, and thermal strength, making it a superior candidate material for membranes.¹²⁷ Graphene is impermeable to all gases and molecules^{11,162}, except hydrogen¹⁶². After introducing pores, liquid, gaseous, and ionic transport is very efficient.¹²⁻¹⁴ Various technologies are available to create nanopores in graphene, using non-scalable serial processes^{45,163}, non-

7. Scaling-Up to cm^2 -Scale

selective oxidative etching approaches^{40,164} that cannot all pore size needs, and also particle-based approaches^{134,135} that lack the same problem. Recently, bottom-up synthesis of porous graphene have been investigated but either lack membrane scale^{24,132} and-or pore size control^{24,133}.

Furthermore, two-step selective approaches relied on the wet chemical etching of the membrane pores, which is problematic due to fabrication-induced membrane ruptures.⁵⁶ Recently, a two-step selective oxygen etching approach has been developed that overcomes previous scalability limitations, wet chemical etching, and offers independent pore size and porosity control.¹⁶⁵ The selective oxygen etching approach can serve as a platform for scalable-membrane synthesis, achieving any required pore size at an optimized porosity for any membrane separation application.

The experimental fabrication has long been limited to mechanically exfoliated graphene^{36,162} or membrane scales in the nanometer range^{24,132} or active membrane areas below the mm-scale^{36,45,55,63,165}. Larger active membrane areas typically are leaky, which may enable the study of transport but lack applicability outside laboratory environments.^{41–43,69,166–168} Few studies successfully achieved graphene membranes with active membrane areas in the millimeter-scale for successful separation demonstrations.^{40,122,134} Recently, major progress has been made by demonstrating cm-scale active membrane areas for desalination and nanofiltration.¹⁶⁹ Initial steps to integrate graphene membrane fabrication into roll-to-roll processes remained challenging due to the occurrence of various defects and ruptures that required subsequent defect sealing steps.^{164,170} Additionally, to harmful chemicals being used, the main driver of fabrication costs is the growth substrate, which has not been demonstrated to be removed in an etching-free manner¹⁷¹ for graphene membrane applications.

Despite the recent progress in scaling up graphene membranes, the multiple orders-of-magnitude gaps between membrane areas have currently been achieved, and membrane areas required for industrial ap-

plications, cost-efficient fabrication are yet to be demonstrated. Membrane fabrication must be scalable, cost-efficient, and reliable to push graphene membranes closer toward application.

This chapter aims to develop scaled-up graphene membranes, using processes that are entirely cost-efficient and compatible with roll-to-roll fabrication approaches. Using such processes lays the foundation to move from cm-scale membranes to meter-scale membranes without a change of technology.

Scaling up the graphene membrane area requires applying a widely applicable support membrane to enable macroscopic handling of graphene, etching-free transfer of graphene from its growth catalyst to enable catalyst reuse as well as scalable and fast processes for pore introduction and fabrication, all combined.

The general goal of fabrication procedure is outlined in **Figure 7.1**. Starting with the synthesis of large scale graphene subsequently, defects can be introduced into the graphene to form nucleation centers similar to our previous work approach.¹⁶⁵ Upon defect nucleation, nanoporous could be synthesized into the graphene while it is still on the growth catalyst, again similar to the approach in our previous work.¹⁶⁵ Then, a porous polymeric support is added to form a support-graphene-catalyst composite. The porous support serves a dual purpose: first is increases the mechanical strength during transfer - it replaces the sacrificial polymeric support layer that is otherwise required - and second, it serves as a support membrane in the later application of the graphene membrane. Lastly, the composite needs to be separated at the graphene-catalyst interface to reuse the catalyst and obtain the final nanoporous graphene supported by a porous polymer.

As each process step involves its individual optimization, several processing steps are developed independently of each other, if possible, in order to reduce complexity.

First, two available polymeric support membranes are compared for their compatibility with etching free transfer and their potential to

7. Scaling-Up to cm^2 -Scale

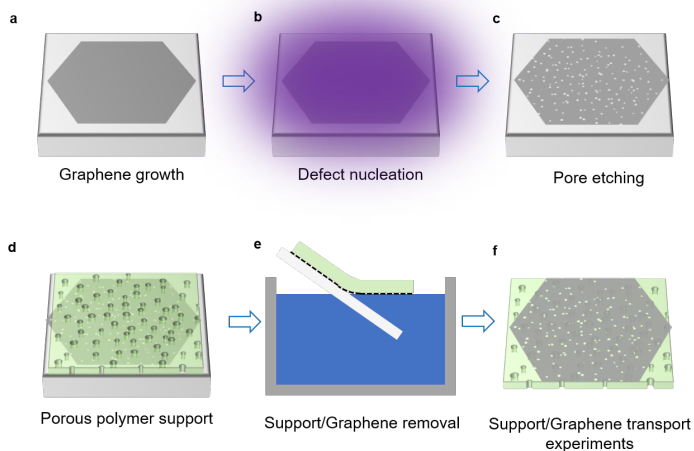


Figure 7.1: Fabrication procedure **a** Graphene is synthesized on a catalytic substrate. **b** Nanopore nucleation centers are introduced into the graphene. **c** Nanopores are expanded from the nucleation centers by means of selective etching. **d** A porous polymeric support is added onto the graphene. **e** The porous polymeric support, laminated to the porous graphene, are separated from the growth substrate to enable catalyst reuse. **f** A hierarchical nanoporous graphene membrane results.

give defect-free graphene membranes. After that, the pore growth while on the substrate is investigated. These two individual developments then lay the basis to merge the two steps into a fully versatile fabrication platform.

7.1 Support Membrane and Transfer

Graphene will always be applied in combination with other materials to form functional devices, be it transistors, mechanical composites, heat transfer pathways, or membrane applications. In almost all appli-

7.1. Support Membrane and Transfer

cations, graphene is not used while it is still on its growth substrate so that the transfer of graphene is unavoidable. Despite graphene being exceptionally strong, given its single atomic thickness, it only takes minute forces to rupture or destroy graphene.⁹ Thus, the majority of fabrication approaches involve the use of a mechanical support layer to increase the total mechanical strength of the composite during fabrication and handling.¹⁷² These layers are often sacrificial layers in that they will be removed afterward again, leaving residues and often impairing device performance. Poly(methyl methacrylate) (PMMA) is the dominating sacrificial transfer material, and its atomically clean removal has been widely investigated.^{173–179} Many other transfer materials have been tried, but none was yet able to replace PMMA as dominating sacrificial material.^{180–182}

These findings strongly support the need for mechanical support during the transfer of graphene, and indeed polymeric materials are also frequently used in membrane separation applications. Therefore, using a polymer during the transfer that can later also serve the function as mechanical support of graphene is standing to reason. If successful, fabrication would be significantly simplified, and atomic residues that often impair functionality would be avoided by design.

When scaling-up graphene membranes, it is additionally vital to consider the costs of fabrication and identify its main drivers, and the metal substrates are contributing mainly to overall operational costs if they are etched away during fabrication.¹⁸³ Therefore, it has been long desired to transfer graphene from its growth substrate without destroying either.

Various etching-free methods have been investigated, and they can be classified into dry delamination, water-assisted delamination, and electrochemical delamination.¹⁸⁴ While dry-transfer often produces large ruptures and defects rendering the method unsuitable for membrane applications¹⁸⁵, water-assisted and electrochemical methods have produced more promising results.^{171,172,183,186,187}

While the delamination of graphene from various growth substrates has been achieved, there is a debate on the intricate details of the

7. *Scaling-Up to cm²-Scale*

mechanism. Early studies attributed hydrogen bubble evolution between graphene and growth substrate to cause delamination¹⁸³, while other studies suggest water intercalation between graphene and the substrate to be key requirements¹⁸⁶, and yet again other studies found ion intercalation of the electrolytes to be necessary.¹⁸⁷

What is clear so far is that atomic details of the surface chemistry and molecular interaction between graphene and its respective substrate, as well as other factors from the electrolyte and electrochemical conditions, may all influence the delamination; these and the polymer for mechanical supporting graphene are expected to influence the delamination success.

Most delamination studies use PMMA as a supporting polymer, which is unsuitable as a supporting membrane in the application. Therefore, another polymer should be employed during transfer.

Two main types of supporting membranes for non-microscopic graphene membranes are dominating in the field. These are polycarbonate-track-etched (PCTE) membranes and polyethersulfone (PES) membranes based on phase inversion.

PCTE membranes are readily available for purchase with various properties and thus conceptually simple to integrate into membrane fabrication.¹²⁷ PCTE membranes have been used to support graphene membranes for various kinds of transport measurements ranging from diffusion-driven ion transport, burst pressure experiments to nanofiltration demonstrations.^{41,56,85,134,167,188} Typically, the graphene membranes were defective after transfer such that leakage transport occurred or it was necessary to develop subsequent defect sealing technologies^{41,56,85,167,188} or the graphene layers were stacked to increase the mechanical stability and prevent cracks in the active membrane area.¹³⁴ However, potential support optimization is limited for PCTE membranes due to their relatively small versatility.

PES membranes can be fabricated following the phase-inversion method, where a solution of PES and solvent are film cast onto a substrate

and then immersed in a nonsolvent.¹⁸⁹ The solvent and nonsolvent mix, such that locally the PES's precipitation limit is overcome, it precipitates and by this forms a porous membrane. The choice of solvent, nonsolvent, and phase inversion conditions are nearly boundless but also provide large parameter space to fabricate membranes with vastly ranging pore sizes, porosities, and cross-sectional morphologies.¹⁹⁰ Previous works with graphene have involved harmful solvents (N-Methyl-2-pyrrolidone (NMP)) and also resulted in leaky membranes,¹⁶⁸ however, the vast parameter space for fabrication optimization was not studied, leaving significant potential for improvement. The recently PES demonstrations as support membrane for graphene membranes for nanofiltration experiments^{168,170} furthermore required additional defect sealing steps after membrane fabrication with either blocking defects by filtration of larger polystyrene spheres or by interfacial polymerization. The vast parameter space for PES membrane fabrication has not been exploited yet.

While the above examples of PCTE and PES membranes to support graphene have demonstrated their potential use in real applications, all of the above works remove graphene from the growth substrate copper by etching the copper, and etching-free methods have not been investigated for graphene supported by either PCTE or PES. For both, the etching-free transfer has not been applied, and it is to be determined which is more promising for this transfer method. Thus, it was the aim to compare PCTE and PES membranes for their feasibility of graphene delamination and further use as membrane support.

7.1.1 Proof-of-concept

Based on the literature survey, PES solutions with dimethylsulfoxide (DMSO) as a solvent were prepared with 15 wt%. A 200 μm high film was casted using a film applicator (Zehntner, ZAA 2300) onto commercial graphene-copper substrates from Graphenea Inc. (**7.2 a**). After casting, the samples were immediately immersed in DI water

7. Scaling-Up to cm^2 -Scale

for 60 min and subsequently dried. For PCTE-supported membranes, the graphene-copper composites were placed on a 180°C hotplate for 2 min with PCTE membranes on top. This temperature is above the glass transition temperature of the PCTE membranes and caused the membranes to make conformal contact with the underlying graphene. Next, electrochemical delamination was performed using a two-electrode setup with current-voltage source and 0.5 M NaCl as electrolyte (**7.2 b**). The samples and a copper wire served as electrodes with 3 V and dried after transfer.

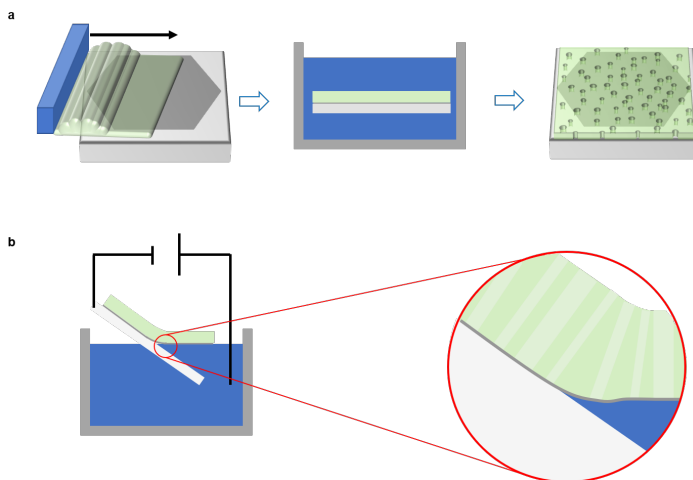


Figure 7.2: **a** Phase inversion fabrication of polyethersulfone membranes **b** Electrochemical transfer of the polymer-graphene composite from the growth substrate, where the delamination of graphene-PES composite from growth substrate happens.

Top-view analysis of the two types of graphene composite reveals significant differences in transfer yield. The PCTE supported graphene membranes display evenly distributed ruptures in the graphene of around $10\ \mu\text{m}$ in length, leaving significant portions of the PCTE uncovered and rendering the application of PCTE as support for large-scale electrochemically delaminated graphene membranes unsuitable. Opposed to this, the PES supported graphene membranes appears microscopically continuous, with few visible ruptures over PES pores,

7.1. Support Membrane and Transfer

but mesoscopic continuity. The surface morphology closely resembles the copper-graphene composite with waves and terraces, revealing an excellent conformal coating of the sample before electrochemical delamination. We attribute this excellent conformal coating to the fluid contact the PES solution makes with graphene before it solidifies and further attribute the graphene's mesoscopic continuity to the close conformal coating of the PES solution. Therefore, for further optimization, PCTE was neglected, and PES, with its vast parameter space of fabrication optimization, was chosen.

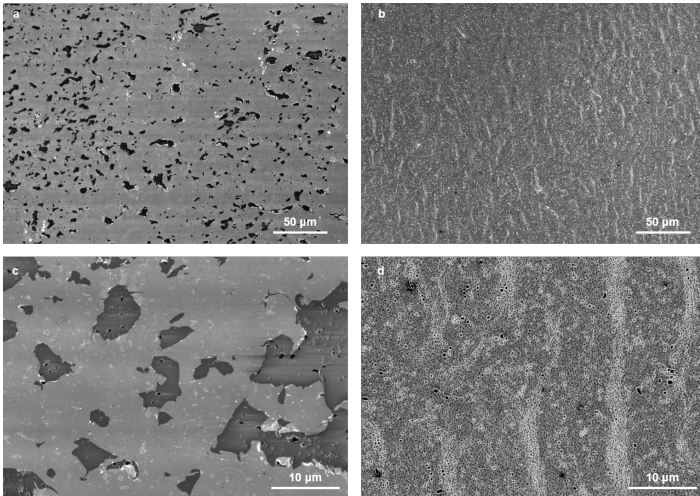


Figure 7.3: PCTE vs. PES supported graphene membranes. **a, c** Top view of graphene supported by PCTE membranes with ≈ 400 nm nominal pore size. Light grey areas mark graphene, dark grey areas show PCTE substrate without covering graphene. The transfer with PCTE displays significant ruptures of the graphene of around ≈ 10 μm length scale spread homogeneously across the samples. **b, d** Top view of graphene supported by PES membranes showing continuous coverage and absence of micron-scale defects as in the PCTE case.

7. Scaling-Up to cm^2 -Scale

7.1.2 Optimization

The mesoscopically superior continuity of PES supported graphene membranes together with its potential compatibility to roll-to-roll fabrication, low materials costs, and wide tuneability promises the potential of PES casting technology for large-scale graphene membranes.

One of the significant phase-inversion variations is the type of cross-sectional membrane area.¹⁹⁰ The cross-section is primarily dominated by the type of non-solvent and the kinetics of phase inversion. The resistance to the supporting material's flow should be minimal to harvest graphene's high potential as a membrane. Minimal flow resistance results from as large as possible channels in the support, a high support porosity, and straight channels. However, the pressure graphene can sustain during operation depends inversely on the size of the supporting material^{85,86} so that eventually a compromise will have to be made.

Non-solvent type

Two types of non-solvent were tested: DI water and air. While DMSO and water mix and locally reduce the PES concentration above the solubility limit to form a solid precipitate, air as a non-solvent leads to evaporation of DMSO over time, leading to significantly slower precipitation.

The faster solvent exchange using DI water as non-solvent then leads to wide, straight channels in the bulk of the membrane, a structure known as 'finger-like' (**Figure 7.4 a**), whereas the slow solvent exchange using air as non-solvent leads to smaller structures and a dense cross-sectional structure of interconnected voids forming what is known as 'sponge-like' structures (**Figure 7.4 c**).

The membrane surfaces additionally show striking differences. Using rapid phase inversion by solvent exchange with DI water, a high density of small (≈ 100 nm) at the graphene-PES interface results (**Figure**

7.4 b). Dark spots are freestanding graphene, grey is graphene supported by PES, and white parts are residues from the transfer. Slower phase inversion with simple solvent evaporation in air results in a lower density of larger pores (≈ 1000 nm) at the graphene-PES interface (**Figure 7.4 d**). We attribute the smaller pores to faster solvent exchange locally at the graphene, and therefore a higher density of PES pores with smaller diameter results. A high density of pores with a small diameter at the graphene interface is optimal to harvest graphene's potential as a high-performance membrane since high surface porosity allows high flow, and smaller support pores increase the operating pressure range of the membranes. Based on ≈ 100 nm surface pores in PES, the freestanding graphene could sustain an operating pressure of up to 100 bar.^{85,86}

Based on the superior cross-section and the more promising surface morphology, DI water immersion for phase separation was chosen as the most promising manufacturing path.

Polymer weight fraction

Phase inversion fabrication of membranes is affected by a plethora of factors: polymer weight percentage, solvent type, non-solvent type, temperature, relative humidity during membrane casting, and type and number of additives to the process. All of the above can influence the resulting membranes, and often the relation between membrane manufacturing and membrane performance skips the step of membrane morphology characterization or quantification.^{4,189,190}

After identifying DI water as a promising non-solvent, we varied the PES weight percentage to investigate its potential to affect membrane properties significantly and, more importantly, its capability to tune membrane fabrication toward rupture free graphene.

The weight percentage of PES in the DMSO solution affects the precipitation point and, therefore, also the membrane formation. The

7. Scaling-Up to cm^2 -Scale

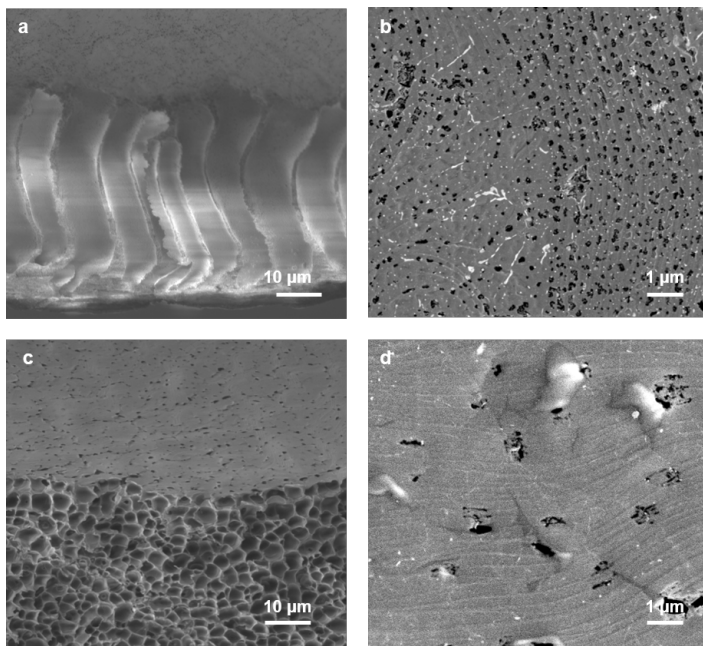


Figure 7.4: Air-drying vs. liquid immersion. a,c Liquid immersion membranes showing a finger-like cross-sectional structure with a high density of small graphene covered pores in PES. c,d Air-dried membranes show a sponge-like structural cross-section with a lower density of PES-surface pores, which are also larger in diameter.

limits of polymer fraction are given from a lower limit above which stable, continuous membranes form with a continuous graphene layer to an upper limit below which the solutions can be processed. These limits for our system were identified as $\approx 12\%$ and 27% . Fabricating membranes at the boundaries of this interval will provide insight into the possibility of the polymer weight fraction to influence the pore morphology (**Figure 7.5**). The membranes display a similar surface morphology, however intricate difference reveal the higher weight percent samples (**Figure 7.5 b**) having more microscopic ruptures and cracks on the order of a few microns in length scale, compared to low weight percent samples ((**Figure 7.5 a**)).

7.1. Support Membrane and Transfer

Manual evaluation reveals high density of PES pores at the surface ($\approx 5 \times 10^{12} \text{ m}^{-2}$) with typical length scale of $\approx 200 \text{ nm}$ (**Figure 7.5 c,d**), with almost indistinguishable differences.

These experiments show that the PES weight fraction has little effect on the surface pore density and pore size. However, the higher density of micron-scale cracks within the high weight percentage renders 15% the superior fabrication option for large-scale continuous graphene membranes.

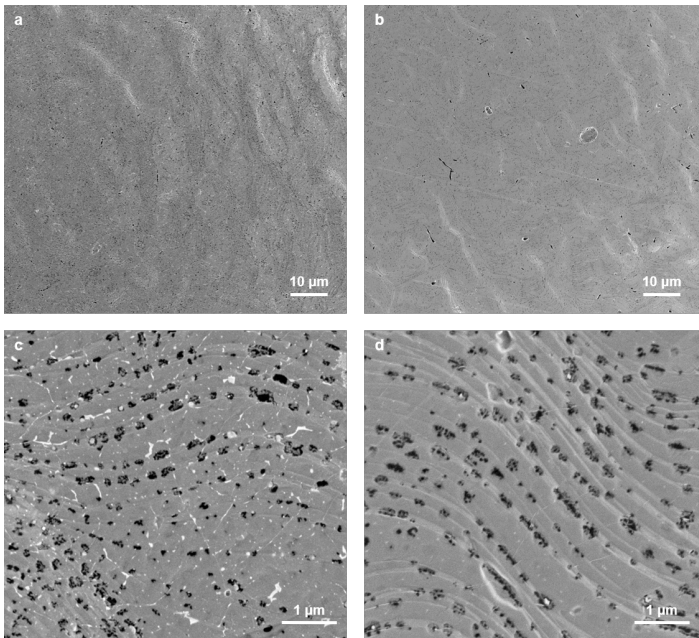


Figure 7.5: Influence of the PES weight percentage. a 15% vs. 24%. Both membrane types show marginal differences in PES surface pores and porosity. However, a markedly lower density of ruptures in the 15% membranes is observed. This lower rupture density is attributed to lower precipitation forces due to the lower weight percentage during phase inversion at the graphene interface.

Electrochemical Delamination

The etching-free removal of graphene from its growth catalyst is an essential step toward commercialization since the substrate etching dominates the fabrication costs. We investigated the possibility to delaminate PES-graphene from copper as well as PMMA-graphene from copper. The transparent nature of PMMA allowed obtaining a better understanding of the delamination mechanism. Most copper surfaces, even though they are covered by graphene, oxidize over time due to air or vapor intercalating in between the copper and graphene.

Using a 0.5 M *NaCl* solution as an electrolyte, delamination success depended on the state of the copper surface beneath the graphene. Freshly reduced copper obtained from hydrogen annealing the surface at 400 °C for 2 h and then spin-coated with PMMA delaminated very poorly, irrespective of delamination voltage. On the contrary, copper, which was slightly oxidized before delamination, could be reliably used for graphene delamination (7.6 a- c). Upon passing a threshold voltage of 0.8 V, a reaction front could be observed moving radially inward from the sample edge. This reveals that the reduction of copper oxide plays a key role in decoupling graphene from its growth substrate. Moving the delamination above 1.5 V resulted in bubble formation below the graphene, which caused ruptures in the material after transfer. We, therefore, proceeded to conduct electrochemical delamination using only oxidized copper surfaces and 1.2 V to speed up the reaction front.

After the graphene has delaminated from all sample edges, the delamination could be greatly accelerated by pulling the sample out of the electrolyte and carefully re-immersing it again to achieve a floating PMMA-graphene at the surface and make the interface between electrolyte, copper, and graphene readily accessible for the electrochemical reaction (**Figure 7.6 d - e**).

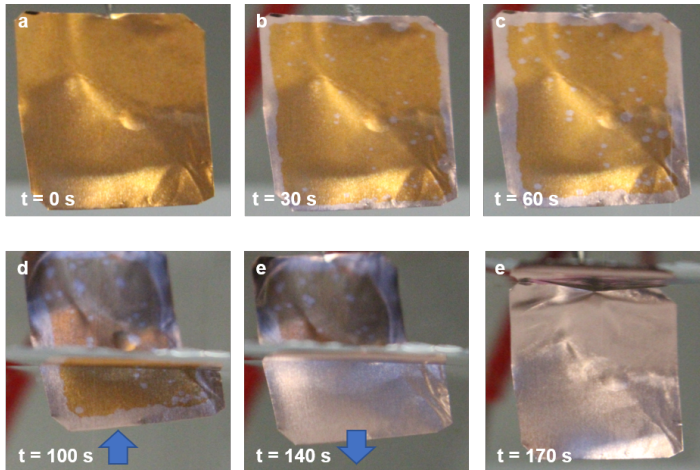


Figure 7.6: Optimization of electrochemical delamination. **a - c** Applying 1.2 V to oxidized copper covered by graphene and PMMA reveals a gradually inward moving reduction front changing the color of the copper surface. Defects in PMMA and graphene layer also lead to a copper reduction from the center of the sample. **c - e.** Picture series of the sample being pulled out of the solution and then carefully back in. The copper reduction now occurs significantly faster due to the accessible interface between electrolyte, graphene, and copper as the graphene-PMMA composite is floating on the electrolyte surface.

Graphene Rupture Analysis

However, graphene is occasionally broken, displayed by very dark, sharp-edged circular parts within the surface (**Figure 7.7**). The density of those ruptures in the graphene layer is manually estimated to $\approx 1 \times 10^{10} \text{ m}^{-2}$ at typically the size of the underlying PES pore ($O(1 \times 10^2 \text{ nm})$).

The rupture density corresponds to one broken graphene pore every 50 PES pores. A basic flow expectation comparison reveals that these ruptures will prevent the functioning of a filtration membrane: Using Sampsonian flow across a 100 nm ruptures and assuming one rupture every 50 PES pores, which each contains five graphene pores of 5 nm

7. Scaling-Up to cm^2 -Scale

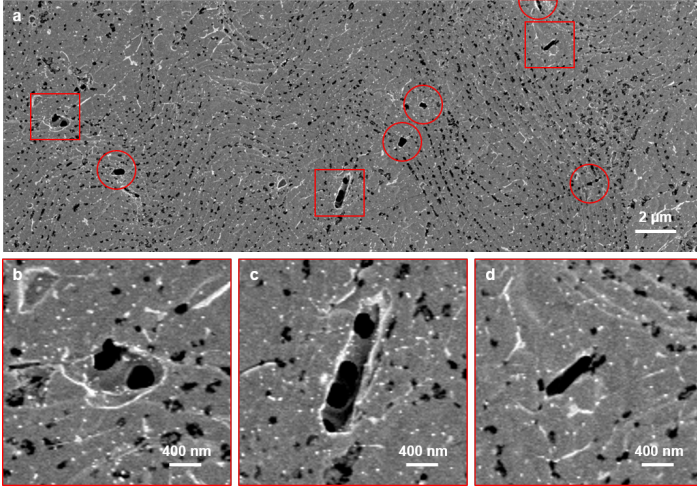


Figure 7.7: Sparse defects are detrimental. Overview image of a best-case membrane (a). Squares and circles frame ruptured graphene with each square frame being magnified in b,c, and d. Typical ruptures in graphene are between 100 nm and 500 nm in equivalent diameter.

(pore density = $6 \times 10^{14} \text{ m}^{-2}$), the ratio of leakage flow through the rupture to selective flow across the graphene is

$$\frac{Q_{\text{graphene}}}{Q_{\text{leakage}}} = 0.00125 \quad (7.1)$$

the leakage dominates the transport, and the membrane cannot be selective for $> 5 \text{ nm}$ objects. It is clearly important to reduce rupture size and density significantly.

7.1.3 Origin of Ruptures and Their Reduction

Due to the inherent importance of reducing the rupture density, it is valuable to investigate the rupture source in more detail.

7.1. Support Membrane and Transfer

Several possible reasons can cause ruptures in graphene: intrinsic defects in the crystal structure from CVD growth, ruptures from drying induced capillary pressures¹⁹¹, mechanical deformation during delamination and handling of the samples, or rupturing of the freestanding graphene that is not mechanically supported. Furthermore, instabilities at the grain boundaries between adjacent graphene crystals that merge during synthesis are known to have less mechanical integrity.¹⁹² To test for these various sources of ruptures in the graphene, different experiments were conducted. First, the potential of intrinsic defects, ruptures, or pinholes within the commercial graphene layer was tested. Testing for intrinsic defects can be done by exposing the graphene-copper composite to a copper etchant, such as APS, and then washing the sample in DI water.⁷⁰ Defect-free graphene acts as a barrier to the etchant and does not allow copper etching. Imperfect graphene allows the copper etchant to contact copper and thus etch away part of the material, forming a cavity. Then, this cavity can be observed using an electron microscope and allows subsequent estimation of the defect density.

We exposed commercial graphene-copper samples to 1 s of 0.1 M APS solution and compared it to a non-etched sample (**Figure 7.8**). The APS exposed sample clearly shows a significant fraction of the copper to be etched, leaving elongated trenches on the surface of $\approx 10 - 25 \mu\text{m}$ in lateral dimension with sub-micron widths. The underlying copper substrate morphology with curved terraces and steps remains. Regions of potentially de-coupled graphene from copper, where the image brightness is lower, remain.¹⁹³

A close observation reveals that graphene wrinkles, visible as thin, bright, edged lines in the untreated sample, are no longer observed in the etched sample. Additionally, the copper-etched trenches appear with very similar edges and dimensions, albeit wider. This observation suggests that the graphene wrinkles possess defects that act as entry points for the copper etchant, and etching proceed isotropically from there, maintaining the wrinkle's original geometry but widening it. Indeed, graphene wrinkles have previously been identified as potential

7. Scaling-Up to cm^2 -Scale

leakage pathways in graphene membranes due to folding induced defects in graphene.¹⁹⁴ These leakage points within the graphene crystal, in turn, result in reduced mechanical stability.^{86,195,196} We, therefore, attribute wrinkles to contribute to the ruptures observed in the transferred graphene.

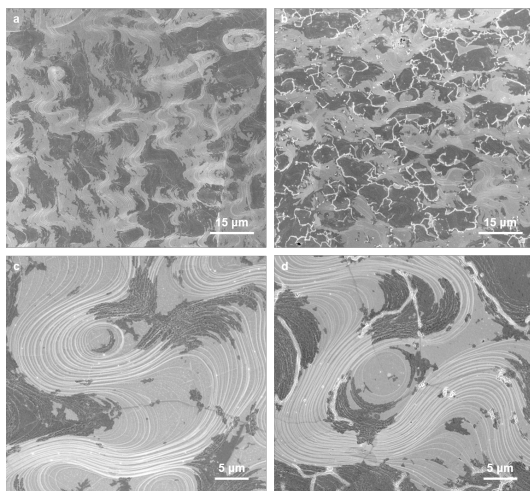


Figure 7.8: Copper etch test for graphene integrity. **a** Untreated graphene on copper. The wavy surface morphology and steps of the copper crystals can be seen. The contrast difference between dark and bright regions indicates de-coupled graphene from the copper substrate potentially due to gas intercalation. Thin, edge lines of bright are known as wrinkles in the graphene that emerge during cooling after graphene synthesis. **b** Graphene on copper surface after brief exposure for 1 s, 0.1 M APS solution. The underlying copper is slightly etched with thin, edge, elongated trenches. Their geometry resembles those of the wrinkles in the untreated sample. Additionally, no more wrinkles are observable in the etched sample. **c** Higher magnification image of the untreated sample. **d** Higher magnification of the etched sample.

The weakness of wrinkles is undoubtedly a problem and limitation for the membrane application of commercial graphene for membranes and appears intrinsic to the purchased product. However, the wrinkles themselves only cover a small fraction of the graphene surface due to their thinness.

Assuming the surface coverage of wrinkles to be between 0.1% and

1%, one could conceive that independent stacking of two individual graphene layers would reduce the weak points in the material in two ways: first, the overall mechanical stability is enhanced by the second graphene layer, and second, the probability of finding two wrinkles overlapping, stacked on one another, is the product of the surface coverage of the wrinkles. Consequently, stacking two layers of graphene subsequently may reduce the graphene surface's weak-spots by 4 to 6 orders of magnitude or more.

7.1.4 Double Layer Graphene

Due to the inherent limitations of commercial graphene, an adapted approach to achieve a lower density of graphene ruptures was developed. Using a sacrificial polymer layer, two layers of graphene were individually stacked to form a double layer graphene membrane that has been proven useable in the past compared to single-layer graphene for other substrates.¹³⁴

Sacrificial Polymer Type

The sacrificial polymer layer fulfills supporting graphene during transfer in a manner similar to our previous projects.^{139,165} However, this time, the previously utilized copper etching process was replaced by electrochemical delamination using the previously identified conditions for successful delamination.

Three types of polymer were compared for mechanical integrity during the electrochemical delamination process: PPA, PMMA (50k), and PMMA (950k) (**Figure 7.9**). While all polymers enabled electrochemical delamination of graphene, we found 950k PMMA to be more suited to achieve macroscopically continuous samples over cm-scale in

7. Scaling-Up to cm^2 -Scale

dimension. In contrast, PMMA (50k) tended to partially stick to the substrate and rupture in whiskers along the delamination direction, and PPA was very fragile during further handling. We found immersion of the polymer-covered samples in DI water for 10 h helpful in obtaining reproducible delamination due to the identified importance of copper surface oxidation. This observation is suggesting a new role of water intercalation successful graphene delamination.¹⁸⁶

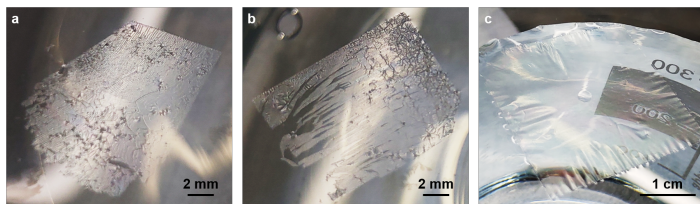


Figure 7.9: Sacrificial polymer for electrochemical transfer. **a** PPA gives a continuous layer, but crumpled locally. **b** PMMA (50k) ruptures along whiskers. **c** PMMA (950 k) gives the largest continuous layers and can be handled the easiest.

Using the sacrificial polymer layer approach with electrochemical delamination enabled the fabrication of $\approx 5 \text{ cm}^2$ -sized membranes of double-layer graphene with almost undetectable defects or ruptures on an asymmetric PES membrane formed using the most promising conditions identified above (**Figure 7.10**).

Based on various optimization iterations, the following membrane fabrication protocol was identified to yield the best results:

1. Sacrificial Layer

- (a) add SLG-Cu to 110°C hotplate, 2 min
- (b) spin coat 950 k PMMA at 4000 rpm, 40 s
- (c) 180°C hotplate, 2 min
- (d) cut edges

2. Electrochemical transfer

7.1. Support Membrane and Transfer

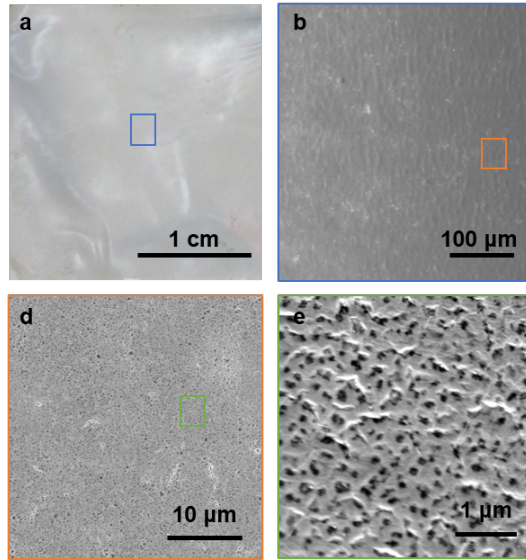


Figure 7.10: Successfully fabricated DLG membrane on PES support. a Optical photograph of a 5 cm² membrane. b-d Scanning electron microscopy images of the membrane with increasing magnifications.

- (a) NaCl solution, 0.5 M
- (b) fully immerse sample, apply 1.2 V, 2 min
- (c) pull-out and push in again to separate PMMA-SLG from Cu
- (d) fish to DI bath using freshly plasma treated SiO_2 wafer (rough side)
- (e) fish with flat SLG-Cu piece to make DLG
- (f) dry tilted

3. PMMA removal

- (a) place sample in H_2 , Ar flow at 400 °C, 2 h
- (b) oxidize Cu surface again by placing the sample in 90 °C DI water, 2 h

7. Scaling-Up to cm^2 -Scale

- (c) cut edges

4. PES creation

- (a) mix 15 % (wt.) solution PES in DMSO
- (b) cast to DLG, 5 mm/s
- (c) immerse in DI water for 5 min
- (d) swivel in ethanol for 2 min
- (e) dry tilted
- (f) cut PES to free Cu surface

Electrochemical transfer

- (a) soak sample in ethanol
- (b) fully immerse in EC bath, apply 1.2 V for 2 min
- (c) carefully remove PES-DLG from Cu surface
- (d) swivel in ethanol bath for 2 min
- (e) dry tilted

To summarize, as for the first part of the process development, it was found that PES membranes as support for graphene are promising and their fabrication using the green-solvent DMSO is possible. The electrochemical delamination of graphene works most reliably for an applied voltage of 1.2 V and an oxidized copper surface beneath the graphene. The oxidized copper surface reduces during the electrochemical process, releasing oxygen in between graphene and copper, which enables delamination.

Quantitative image analysis using ImageJ confirms the qualitative observations (**Figure 7.12**). Comparing the rupture density of the initial proof-of-concept fabrication recipe with those of a single layer after fabrication optimization and double layer after fabrication optimization, it can be seen that both rupture sizes and rupture density could

7.1. Support Membrane and Transfer

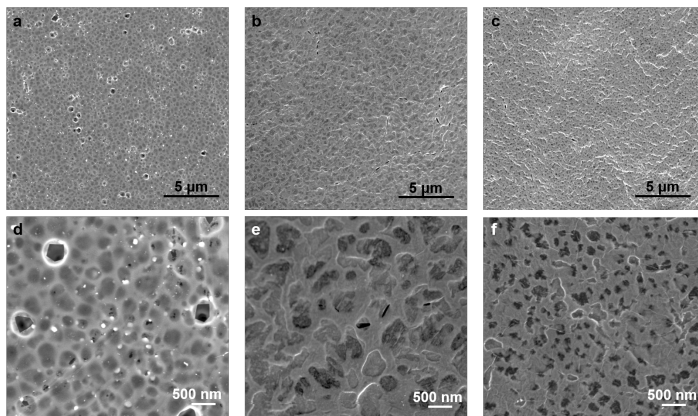


Figure 7.11: Comparing PES supported graphene membranes. **a,d** Single-layer graphene on PES from proof-of-concept recipe. Various ruptures are present, which are attributed to drying while wetted with water. **b,e** Single-layer graphene on PES from optimized transfer recipe. Few defects are visible, mostly resembling the shape of wrinkles. **c,f** Double-layer graphene from optimized transfer. Wrinkle-shaped defects are gone, few small defects still remain.

be reduced by almost an order of magnitude each. We speculate that rupture density could be significantly reduced by using bubble-free delamination voltages and ethanol washing the membranes before drying. Lower local pressure forces due to evaporating droplets of bubbles would contribute to lower ruptures. Remaining intrinsic membrane defects are attributed to intrinsic defects in graphene, more specifically from wrinkles and grain boundaries in the graphene.

An additional effect to reduce the rupture density in double-layer graphene may be the smaller PES-pore size at the graphene interface compared to both single-layer approaches (**Figure 7.13**), which will increase the maximum pressures the freestanding graphene membranes can sustain.^{85,86}

An analysis of the broken graphene area compared to the freestanding graphene area then also demonstrates a clear improvement of rupture reduction (**Figure 7.14**). The number of graphene-covered PES pores

7. Scaling-Up to cm^2 -Scale

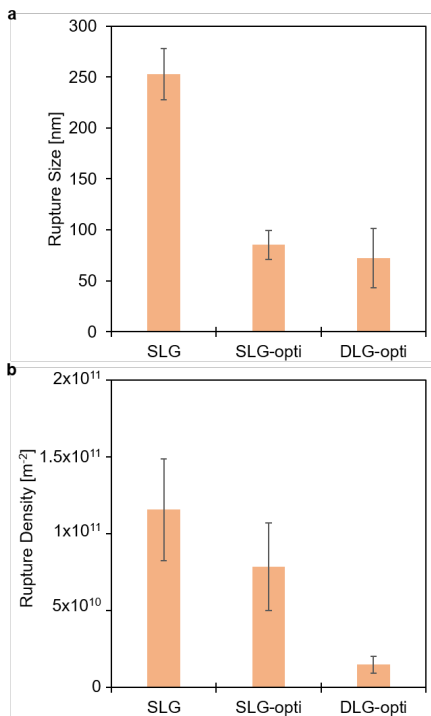


Figure 7.12: Comparing graphene ruptures from different fabrication approaches. **a** While the optimized fabrication protocol does not significantly change the PES pore size, it still increases the PES surface porosity (**b**). Fabricating double-layer membranes with the optimized protocol leads to smaller PES surface pores and surface porosity.

per graphene rupture could be increased from around 40 to ≈ 2000 after fabrication optimization and using double-layer graphene. What matters for the selectivity of the graphene area is the total rupture area compared to the total the available membrane area. The fabrication optimization enabled reducing this metric from initially around 3% to less than 0.1%. Analyzing the optimized transfer using single-layer graphene reveals that roughly 0.2% of the freestanding graphene area are defective. Independent stacking of two such layers in the transfer could cause the resulting fractional rupture area to be the

7.1. Support Membrane and Transfer

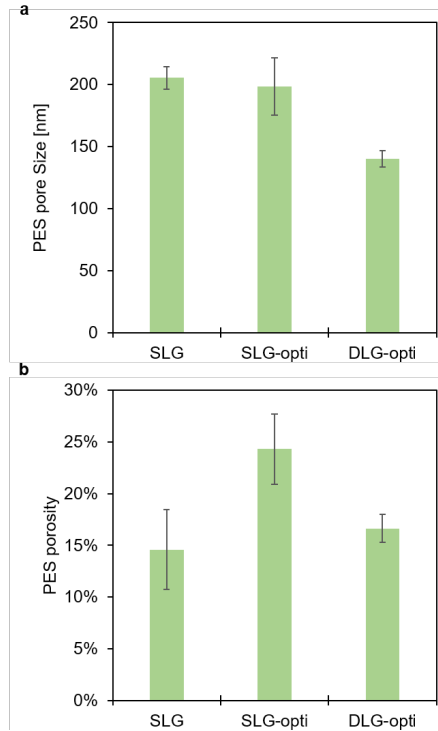


Figure 7.13: Comparing PES surface properties. **a** Single-layer graphene on PES from proof-of-concept protocol, optimized protocol, and double-layer protocol. The rupture size becomes significantly smaller after optimization, with average rupture areas corresponding to less than a tenth of the average rupture areas of the initial fabrication protocol. **b** Rupture density comparison also reveals significant improvement of the rupture density with double-layer graphene showing almost a tenth of the initial rupture density.

square of its initial value, giving expected double-layer graphene (DLG exp) fraction of only 0.001 %. However, the fabrication experiments with double-layer graphene reveal a higher fraction of 0.1 %, revealing that the stacking is not independent and that additional effects and interactions during double-layer graphene fabrication cause additional defects. Potentially, trapped gas or liquid pockets after double-layer creation may burst in the subsequent annealing steps.

7. Scaling-Up to cm^2 -Scale

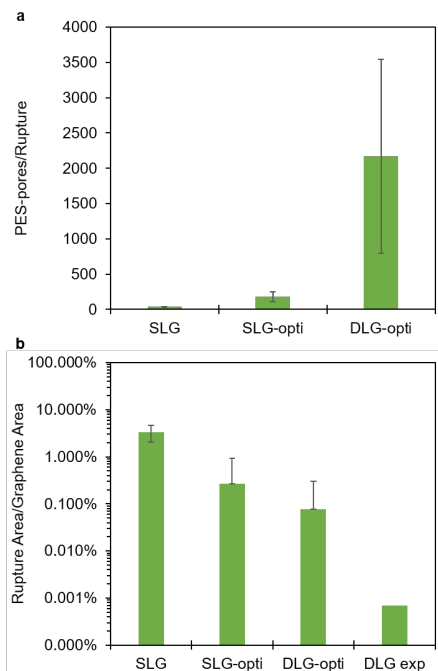


Figure 7.14: Quantification of the broken graphene area to freestanding graphene area. **a** The number of graphene-covered PES pres per rupture, increasing significantly after optimizing the transfer protocol and using double-layer graphene. The large error bar is in part due to the very few numbers of ruptures observed in the SEM images for analysis, giving strongly varying relative numbers per image. **b** The ratio of the ruptured-graphene area to the intact graphene area could be reduced from 3% in the initial experiment to less than 0.1%, albeit not reaching the expected ratio of 0.001% for double-layer graphene as the square of the single-layer value after optimization.

Ultimately, the optimization involved the utilization of ethanol washing, bubble-free delamination, and the use of double-layer graphene to reduce the rupture density of the membranes significantly (**Figure 7.11**). What is striking is the difference between single-layer transfer in terms of circular pores compared to the optimized transfer recipe. The optimized transfer recipe involves washing the membranes in ethanol to exchange water with ethanol in order to reduce capillary pressures during drying. We attribute these differences to the lower

7.1. Support Membrane and Transfer

capillary pressure in ethanol drying compared to water.

Interestingly, the PES pore size beneath double-layer graphene membranes is significantly smaller compared to single-layer graphene. Smaller PES pores are also beneficial for the membrane to sustain higher operating pressures. Furthermore, the ethanol washed single-layer graphene membranes reveal only defects that closely resemble the shape and dimensions of grain boundaries in graphene. This observation is another indication that, indeed, single-layer graphene membranes from a commercial source are limited by inherent weaknesses of poor inter-grain connectivity and that adding another layer of graphene to reduce their effect is a promising and needed measure toward large-scale membranes.

7.2 Defect Nucleation

With a fabrication approach that reduces the rupture density to a promising level, defect creation on the PES supported graphene can be tested to provide insight into two questions: First, "does graphene supported by PES rupture upon defect introduction?" And second, "Can the defective graphene already serve as a functioning membrane for separation applications?". To achieve defect generation on a large scale, we utilized short plasma exposure using low power dry air plasma (Harrick Plasma PCD-32G) to treat the membranes. Upon continued plasma exposure, the Raman spectrum of DLG graphene evolves and reveals the defect creation into the graphene lattice (**Figure 7.16**). After 20 s plasma exposure, graphene is still rupture-free (**Figure 7.15**) indicating defects to be below resolution limit of the electron microscope image and that no larger-scale ruptures result from plasma treatment.

7.3 Nanopore Growth

Membranes need various pore sizes, depending on the application. While plasma alone can make < 1 nm pores, it cannot expand the pores to larger sizes than due to its non-selective etching nature.^{11,55} A selective etching approach has been demonstrated for freestanding graphene.¹⁶⁵ Graphene, while supported on a substrate, can also be etched from the edge in various gas environments.^{197–199}

We investigated the possibility of etching graphene nanopores into a large-scale graphene samples *via* exposure to hydrogen at elevated temperature and while supported to its platinum growth substrate.

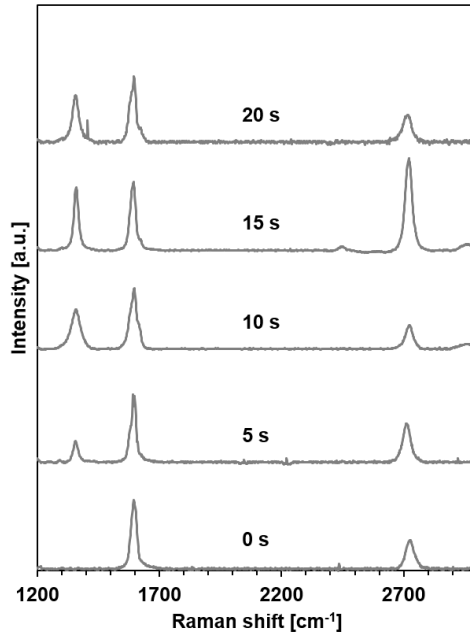


Figure 7.15: Raman spectrum evolution of plasma treated graphene supported by PES. Starting from initially defect-free graphene, exposure with plasma leads to an increase in the D-peak (1350 cm^{-1}) and simultaneously the 2D-peak intensity ($\approx 2700\text{ cm}^{-1}$) reduces, both indicating the introduction of defects into the graphene lattice.

7.3.1 Proof-of-concept

With the help of a custom-built environmental scanning electron microscope^{200–204}, graphene supported on a platinum foil was exposed to high temperatures in a hydrogen environment in order to etch graphene from its edges.

To test the etching capability, several artificial holes were drilled into the graphene-platinum using FIB. Subsequently, the sample was heated in hydrogen atmosphere at 17 Pa total pressure, and the surface was monitored using ESEM (**Figure 7.17**).

7. Scaling-Up to cm^2 -Scale

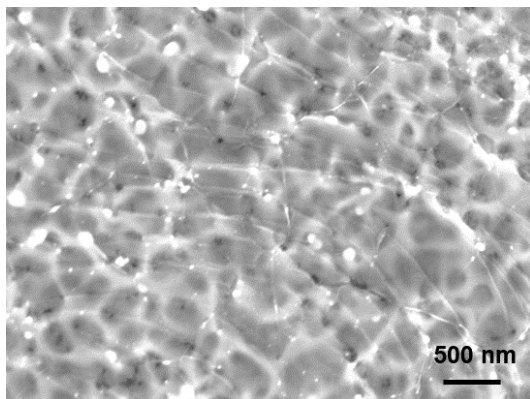


Figure 7.16: Successfully fabricated DLG membrane on PES support treated by dry air plasma. While the Raman spectrum reveals atomic scale defects in the graphene, no ruptures or additional defects in the graphene are observable in SEM, revealing the defects to be below the resolution limit.

Below an estimated threshold temperature of 600°C , no etching of graphene can be observed (**Figure 7.17 a, b**). The FIB-drilled ca. 500 nm circles appear slightly more dark on the graphene on its platinum growth catalyst, while very dark and homogeneously distributed spots mark graphene adlayers from secondary growth. As soon as the FIB drilled, defective graphene was found to etch away (**Figure 7.17 c**) the temperature was kept constant, and with a slight time shift of etching onset, all FIB-drilled pores show a marked change in contrast due to the uncovered platinum substrate that was previously below the defective graphene. The drilled pores continue to grow radially outward, and adlayers simultaneously etch radially inward (**Figure 7.17 d**), both revealing the intended selective edge-etching behavior. With prolonged etching, while the FIB drilled pores to continue to grow in size, also small, new pores emerge (**Figure 7.17 e**). These stem from intrinsic defects in the graphene lattice that initially etched undetected due to their small size. The graphene was polycrystalline and is thus expected to contain chemically weaker locations occasionally.²⁰⁵

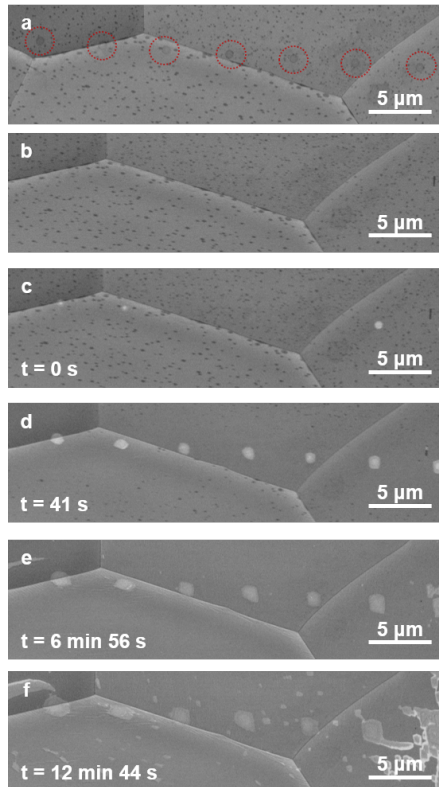


Figure 7.17: *In situ* pore growth observation. **a** Single-layer graphene covered platinum layer. Graphene grain boundaries are observable as long straight lines, small black islands are secondary nucleation islands of graphene, and dark grey circles, highlighted by red circles, are FIB-drilled pores of ≈ 500 nm pores in graphene. **c** Defected graphene etches away first in some of the circles. **d** All FIB drilled circles etch radially outwards; graphene ad-layers also etch away inwards. **e** Graphene ad-layers are etched away, FIB drilled pores continue to increase in size, but also small pores other locations emerge. **f** Small pores in other locations also continue to etch radially outward, with a slightly non-circular shape.

These experiments showed that radial etching of defects in graphene into larger nanopores is also possible while the graphene is supported on platinum. This approach may thus be a promising path toward pore fabrication for membrane applications. To further analyze the

7. Scaling-Up to cm^2 -Scale

experiments and better understand the etching behavior, quantitative image analysis is required.

7.3.2 Image Analysis and Quantification

Quantitative image analysis may yield valuable information such as pore size, pore density, pore growth rate, and can also allow more detailed analysis such as eccentricity and distribution. The complexity of the ESEM images, however, did not allow a simple threshold-based evaluation using ImageJ, as was applied in previous projects. Therefore, a more involved image quantification algorithm was written using Matlab, utilizing some features of ImageJ. Due to the need to track pores over time, the images had to be aligned precisely. This can be achieved with the StackReg package for ImageJ (**Figure 7.18**).²⁰⁶

After the image alignment, the images were cropped to the same field of view and adjusted for consistent contrast-brightness throughout all images from the etching experiment (**Figure 7.19**). Next, image processing steps such as noise reduction, background removal were applied before an anisotropic diffusion filter and local adaptive thresholding allowed to binarize the images into pore and non-pore parts (**Figure 7.20**).

The coordinates, sizes, perimeters, and other parameters can then be extracted from the binarized images in the labeling step. Last, the binarized images were analyzed over time *via* assigning detected pores of one time-step to a pore of a previous time step. In that way, the pore size over time for each pore could be tracked. Last, the pore size evolution can be evaluated into equivalent diameter evolution etch-start and more.

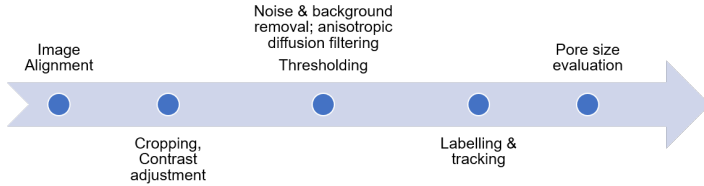


Figure 7.18: Quantitative pore size analysis algorithm. The raw images are aligned in a first step, then cropped to the region of interest, and a universal color-scale is applied. Next, image processing with noise and background removal, followed by anisotropic diffusion filtering and thresholding, enables binarizing the images into pore/no-pore regions. The identified pores are labeled and quantified. Last, the pores are tracked over time, allowing to obtain a quantitative pore size evaluation.

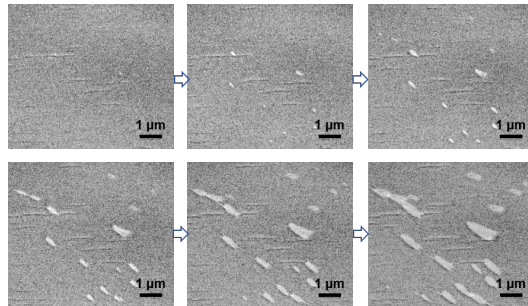


Figure 7.19: Graphene pore growth observation. Starting from intrinsic defects, nanopores in graphene grow over time, with radial increase but also with preference to non-circular shape.

7.3.3 Nanopore Growth Dynamics

The nanopore growth dynamics could be quantified after image processing (**Figure 7.21**). Defining the time zero as the time when the etching of the FIB-drilled pores commences, several nanopores grow to SEM-observable size within 10 min of etching. Once a pore can be observed, the radial growth rate follows a linear behavior over time with a diameter growth rate of ≈ 1 nm/s. Even though the pores created so far are far too large to be interesting for membrane appli-

7. Scaling-Up to cm^2 -Scale

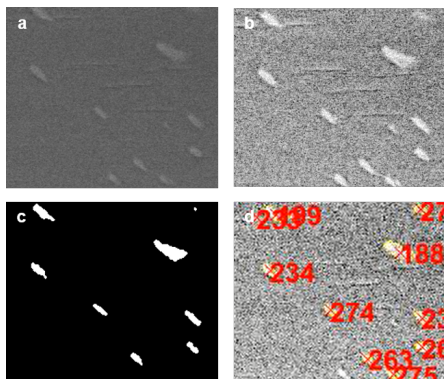


Figure 7.20: Image Processing. **a** Raw image of pores in graphene on platinum. **b** processed image before binarization occurs. **c** binarized image showing pores in white and graphene in black. Each pore can thus be evaluated in size and position, next to other geometric features. **d** Each pore is assigned an index, such that the pore in the next time step can again be correctly assigned.

cation, this pore growth rate is promising to reach small nanopores. The observed pore size distribution observed in the previous project as well as in the etching while on platinum appears to stem from the shift in etching onset, after which the pores then grow at a very similar rate. Consequently, the etching onset should be minimized in order to achieve narrow pore size distributions of the membranes.

Here, significant potential for pore growth optimization exists in the form of pressure, temperature, and gas composition. Still, as a proof-of-concept, it can be concluded that the selective etching approach described in the previous chapter can also be extended to graphene supported on its growth metal surface.

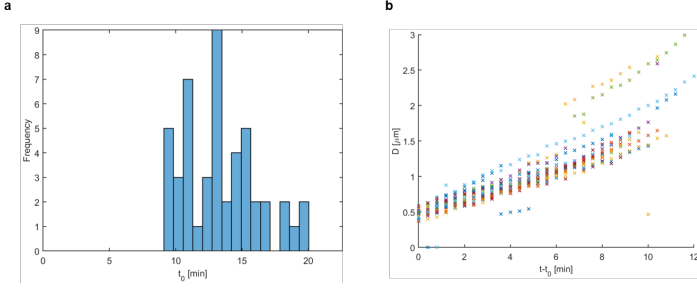


Figure 7.21: Pore growth dynamics. **a** Distribution of first pore detection time after etching start. After around 10 min of annealing, pores from intrinsic defects become observable with around 100 nm lateral dimension. After another 10 more minutes no more pores emerge, but only the available ones keep growing in size. **b** The pore diameter evolution for various pores, identified by individual colors. Most pore follow a linear growth over time with constant rate. Some pore merge, leading to step-wise increase in pore diameter.

7.4 Transport Estimation

The expected liquid transport across the fabricated membranes can be estimated by analyzing the membrane geometry in more detail (7.22) in combination with the quantified membrane properties of optimized double-layer transfer.

The total membrane thickness is $L = 70 \mu\text{m}$ and consists of straight channels with $2R_{PES,c} = 5 \mu\text{m}$ diameter and around 300 nm wall thickness. The surface of the PES membrane consist of $2r_{PES} = 140 \text{ nm}$ diameter pores with a density ($1 \times 10^{13} \text{ m}^{-2}$) that corresponds to $N_{PES,s} = 211$ PES surface pores per PES channel.

The flow passing through the membrane will experience various resistances: First, the flow either flows across the graphene nanopores or through a rupture, then the flow flows across a PES surface pore, which leads the flow into a PES channel. However, since there are always several graphene pores as well as ruptures per PES surface pore, the flow resistance of each graphene pore is in parallel to the other graphene pores and ruptures that are on the same PES pore. Similarly, a number of PES pores then lead the flow into a single

7. Scaling-Up to cm^2 -Scale

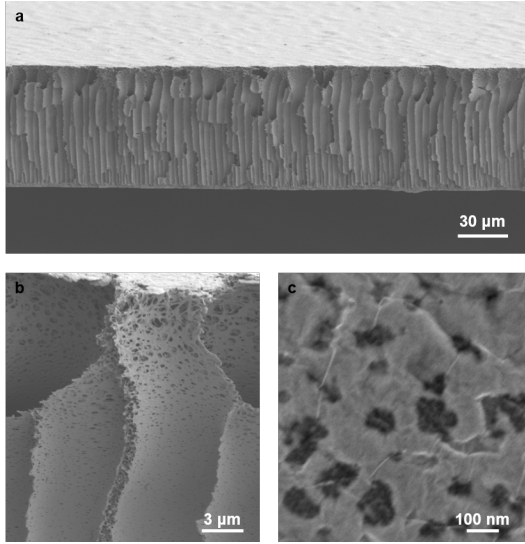


Figure 7.22: Geometry of optimized hierarchical membrane. **a** Birds-eye view of the membrane cross-section and surface. **b** Detailed view of top-part of cross-section in contact with graphene membrane. **c** high magnification image of double layer graphene spanning PES nanopores.

PES channel. The PES pores also act in parallel at that stage. A resistance network follows a nested structure of a number of parallel resistances that are then connected in series (**Figure 7.23**). The flow across graphene is well described by Sampson's formula, and the thin surface layer of the PES allows assuming Sampsonian transport for the ruptures and the PES surface pores. The channel will follow the Hagen-Poiseuille formula due to its aspect ratio.

The transport resistances are thus:

$$R_G = \frac{3\mu}{r_G^3} \quad (7.2)$$

$$R_{rupt} = \frac{3\mu}{r_{rupt}^3} \quad (7.3)$$

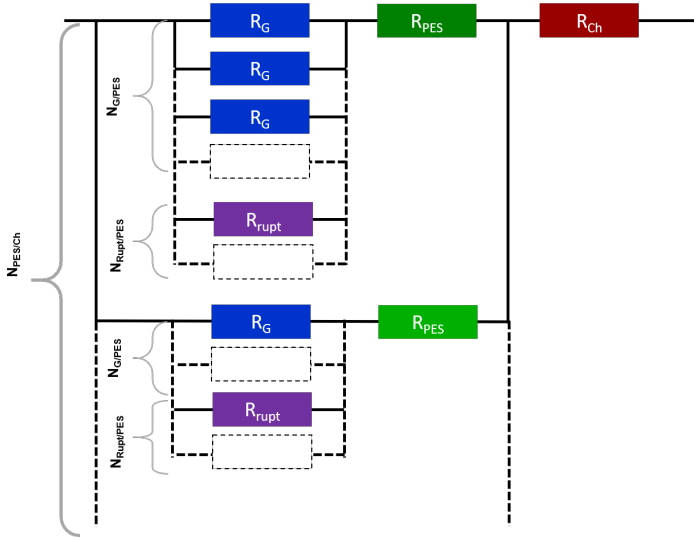


Figure 7.23: Equivalent resistance network of the hierarchical membranes. The flow experiences three overall resistances in series: the graphene surface with nanopores and ruptures in parallel to each other, followed by the PES pores that are in parallel to each other, and finally, the PES channel.

$$R_{PES,s} = \frac{3\mu}{r_{PES,s}^3} \quad (7.4)$$

$$R_{PES,ch} = \frac{8\mu L}{R_{PES,c}^4} \quad (7.5)$$

for graphene nanopores, R_G , ruptures, R_{rupt} , PES surface pores, $R_{PES,s}$, and the PES channel, $R_{PES,ch}$. The combined graphene and rupture resistance per PES pore is evenly distributed across all graphene nanopores, $N_{G,PES}$, and the ruptures, N_{rupt} , that lead to one PES

7. Scaling-Up to cm^2 -Scale

surface pore such that:

$$R_{surf,tot} = \left(\frac{N_{G,PES}}{R_G} + \frac{N_{rupt,PES}}{R_{rupt}} \right)^{-1} \quad (7.6)$$

This surface resistance is in series with each PES surface pore, that again a parallel to each other. Consequently, the resistance to flow for all PES surface pores acting in parallel to each other is

$$R_{PES,s,tot} = \frac{R_{surf,tot} + R_{PES,s}}{N_{PES,ch}} \quad (7.7)$$

This resistance is then in series with the PES channel resistance, giving the overall flow resistance across the membrane:

$$R_{tot} = R_{PES,s,tot} + R_{PES,ch} \quad (7.8)$$

Then, the total flow across the membrane can be calculated:

$$Q_{tot} = \frac{\Delta P}{R_{tot}} \quad (7.9)$$

Since selectivity occurs at the graphene surface, only the graphene nanopore resistance and the rupture resistance need to be considered to predict the membrane selectivity.

We define the selectivity as the transport across the graphene nanopores divided by the total transport across the graphene nanopores and the ruptures.

$$S = \frac{Q_G}{Q_{surf}} = \frac{R_{surf,tot}}{R_{tot,G}} = \frac{N_{G,PES} \times r_G^3}{N_{G,PES} \times r_G^3 + N_{rupt,PES} \times r_{rupt}^3} \quad (7.10)$$

or

$$S = \frac{n_G'' r_G^3}{n_G'' r_G^3 + n_{rupt}'' r_{rupt}^3} \quad (7.11)$$

using the respective areal number densities n .

Using this equation, the selectivity of the filtration membrane can be estimated from the ratio of flow across graphene pores to the total flow. Assuming 5 nm graphene pores at a typically obtainable density of $n_G = 1 \times 10^{15} \text{ m}^{-2}$ or small pores of 1 nm at high pore density⁵⁵, and keeping the measured rupture sizes in optimized double layer transfer, with $n_{rupt} = 1.5 \times 10^{10} \text{ m}^{-2}$ for the 5 nm membranes and $n_G = 1 \times 10^{16} \text{ m}^{-2}$ for the 0.7 nm membranes. The respective selectivities of the membrane would be $S(5nm, 10^{15}m^{-2}) = 97.1\%$ and $S(0.7nm, 10^{17}m^{-2}) = 47.9\%$. Consequently, the quality of membrane fabrication is promising to enable a selective membrane even for pores approaching atomic dimensions.

The model can furthermore be used to set a target rupture density to increase selectivity, assuming different rupture sizes for the above 5 nm membranes (pore density of $1 \times 10^{15} \text{ m}^{-2}$) (**Figure 7.24 a**) and 1 nm membranes (pore density of $1 \times 10^{16} \text{ m}^{-2}$). It can be seen that to achieve more than 90 % selectivity, the optimized double layer fabrication strategy is promising to 5 nm pores and a moderate selectivity of 65 % could be expected for 1 nm pores.

The situation becomes more challenging when the target selectivity of 1 nm membranes is above 95 %, here the rupture density should be decreased by at least another factor of ten.

7.5 Discussion

This chapter outlined a path toward roll-to-roll compatible graphene manufacturing processes and investigated the individual process steps. Graphene membranes supported by PES membranes can be successfully and reliably delaminated by electrochemical means. Currently, intrinsic defects in the single-layer graphene, such as wrinkles, limit

7. Scaling-Up to cm^2 -Scale

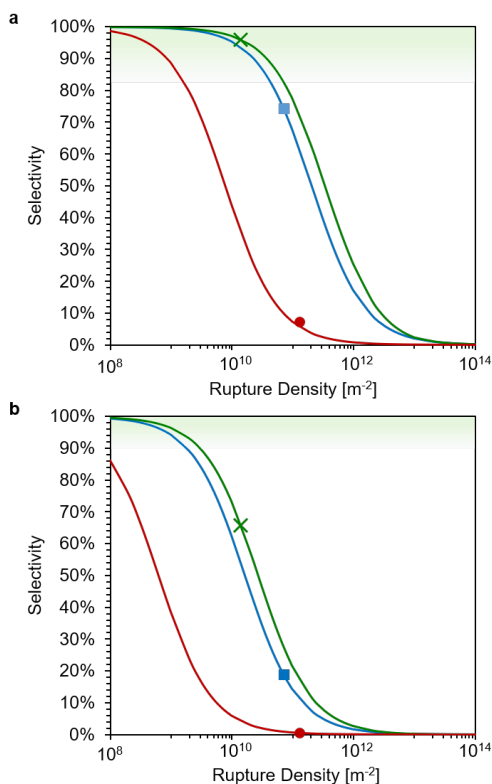


Figure 7.24: Predicted membrane selectivity for a given graphene membrane and pressure-driven flow. **a** Assuming a 5 nm membrane with pore density of $1 \times 10^{15} \text{ m}^{-2}$. The solid red line corresponds to defect sizes of 253 nm as obtained from the initial single layer fabrication (red circle). The blue line corresponds to 85 nm defects as obtained after single layer transfer optimization (blue square). The green line corresponds to defects of 72 nm diameter, as measured from optimized double-layer graphene transfer (green cross). It can be seen that another reduction of the rupture density for double-layer graphene could push the expected selectivity to above 99%. **b** Expected membrane selectivity, assuming 1 nm graphene pores at pore density of $1 \times 10^{16} \text{ m}^{-2}$. Color code is the same as in **a**. To obtain selective membranes for such small graphene pores, the rupture density should be reduced by another factor of 10.

the direct application of the single-layer graphene as a membrane. However, it was found that creating double-layer graphene membranes

can significantly reduce the ruptures density and size, achieving over 99.9% graphene surface coverage. Analytical transport modeling was applied to predict the membrane selectivity of the fabricated membranes, assuming realistic graphene pore sizes and density. It was shown that the membranes are promising to achieve > 90% selectivity if 5 nm are created within the membrane. Oxygen plasma exposure was identified as a promising approach for nucleating atomically small defects in graphene while supported on its growth substrate or when freestanding on PES membranes. Furthermore, nanopore growth using the selective etching principle can also be achieved when graphene is supported by its growth catalyst at promising rates for membrane fabrication.

Nevertheless, the individual process steps still need more improvement, especially graphene synthesis and pore growth, and merging into a complete process before graphene membranes at cm-scale can be fabricated in a roll-to-roll process and applied to various separation applications. Additionally, testing liquid filtration experiments with the available optimized double-layer transfer recipe is mandatory.

Chapter 8

Conclusions & Outlook

8.1 Conclusions

This thesis showed that the research field of graphene membranes is highly dynamic, with rapid progress but equally important challenges for the technical realization of graphene membranes.

From the challenges of graphene membranes, this thesis first applied a well-controlled membrane fabrication technology to study liquid permeation across nanoporous graphene membranes and of membranes with gradually increasing thickness. Liquid transports across nanoporous graphene for a range of fluid properties, pressures, and pore sizes following Sampson's formula accurately. The controlled thickness variation allowed to challenge the currently idealized membrane thickness of single atomic thickness by demonstrating a gradual flow transition from Sampson's formula to Hagen-Poiseuille formalism, which is described the Dagan's formula. For membranes with aspect ratios below one, the flow enhancement due to marginal intra-channel viscosity reduction is small. On the other hand, in-plane stresses continue to increase significantly. Consequently, the ideal membrane thickness

8. Conclusions & Outlook

from a permeance *versus* stability point of view has aspect ratios near one.

Furthermore, the fouling behavior of graphene membranes was investigated, and a suitable model was identified. Graphene membranes foul due to particulate deposition at its surface, with so far relatively low lifetimes. These limitations are attributed to the high flow compared to 3D membranes. Atomic layer deposition was identified as a promising route for membrane lifetime enhancement by a factor of ≈ 2 using conformal titania deposition.

Overcoming the limits of state-of-the-art graphene fabrication techniques was another goal of this thesis. The developed technique allows controlled parallel, scalable, and precise pore formation of sub-nm to ≈ 5 nm with tunable pore density at high porosity. This pore size range was previously not addressable and is essential for applications ranging from gas separation, water desalination to nanofiltration. The developed technique applied low-dose ion irradiation to create randomly located defects into the graphene crystals; upon defect generation, selective etching of carbon edge atoms leads to the gradual expansion of the initial atomic defects into permeable nanopores in graphene.

The parallel pore growth technology is particularly crucial for scalable graphene membrane fabrication due to the titanic number of pores required in technologically relevant applications. The technique demonstrated pore growth and size expansion with angstrom-scale precision using gas separation experiments.

The membranes fabricated with the newly developed selective oxygen etching technique demonstrated a range of high gas separation performance. The gradual pore growth can increase permselectivity up to 50% and, at the same time, increase the permeance by a factor of ≈ 10 , starting from highly selective membranes displaying molecular sieving characteristics at unmatched gas permeance. Prolonged selective oxygen etching leads to larger pore sizes up to ≈ 5 nm with reduced selectivity but permeance increases of more than two orders

of magnitude, creating membranes with extreme permeance at still attractive selectivity.

The parallel pore growth technique and the fact that no additional transport pathways are created allowed studying gas permeation mechanisms of the various gases and their mixtures. The permselectivity of gas pairs is typically higher than the mixture permeation and separation case. This finding was attributed to the effects of molecular momentum transfer near the pores since gases with higher molecular weight pass the graphene nanopores in the presence of a lighter gas with a higher rate, a phenomenon which can be explained by momentum transfer from light to heavy molecules during molecular collisions. Furthermore, pressure studies revealed that gases such as H_2 , CH_4 , and CO_2 all permeate across graphene nanopores along with an additional, previously theoretically hypothesized pathway of surface adsorbed diffusion. Their permeance increases for higher pressures, an observation incompatible with pure molecular effusion across nanopores. Instead, molecules adsorbed to the graphene surface experience a concentration gradient to the permeate side of the membrane and diffuse toward it, where they then desorb into the permeate gas stream.

While the transport physics across nanopores is intriguingly rich and offers tremendous room for further research, other aspects of technological application seem more pressing to the author. Most notably, the size of available graphene membranes in laboratory-scale experiments is mostly in the micro-meter range and rarely reaches to the millimeter or even centimeter-scale. Nevertheless, any real application requires membrane areas orders of magnitude larger than this.

Various limitations prevent the availability of larger graphene membranes. For one, the synthesis area of membrane-grade quality graphene is not available commercially to this date, but also process integration to enable cheap, environmentally friendly fabrication of graphene membranes that can be integrated into membrane modules or other devices is lacking.

8. Conclusions & Outlook

To address these limitations, another graphene membrane fabrication technique was conceived and developed to the proof-of-concept stage. PES obtained as a versatile method to create porous support of single and double layer was investigated. Copper oxidation prior to electrochemical delamination was identified as mandatory for successful delamination. Together with ethanol washing and bubbling-free delamination, the transfer of single-layer graphene was identified to be merely limited by intrinsic weaknesses from grain boundaries and wrinkles. Double-layer graphene fabrication could overcome single layer limitations. Plasma exposure of graphene supported by PES was demonstrated as a promising route to create atomically small defects into the material, and hydrogen etching of graphene defects into pores, while it is supported on its growth catalyst, demonstrated a feasible simplification of state-of-the-art fabrication methods. All processes are compatible with roll-to-roll fabrication, and low-cost and membrane areas of up to 5 cm^2 were demonstrated. The optimized membrane fabrication protocol enables reducing rupture density and the average area around two orders of magnitude, each and thus significantly improving the membrane integrity. Analytical flow modeling across the hierarchical membranes predicted the rupture density low enough to enable successful nanofiltration when pores are introduced into the membranes.

8.2 Outlook

Graphene has been proven to be exceptionally promising for various technologies, but at the same time criticized for a perceived slow rate of adaption into industries and difficulties in delivering the same outstanding performance measured in laboratory environments in a real-world situation.^{207,208}

In terms of graphene membrane performance, plenty of room for improvement indeed remains. State-of-the-art graphene membranes with sub-nm to few-nm pores typically have porosities below the 1 % range and are supported by yet another membrane having a few percent porosity. Optimizing these porosities holds the promise to yet again increase permeance by one or more orders of magnitude.

Additionally, the potential to achieve higher selectivity with graphene nanopores is far from exhausted, and on a fundamental level, various important questions for basic research are yet to be answered.

For one, the measured selectivities typically mismatch the predicted selectivities, often by orders of magnitude. A clear relation between pore size and selectivity is lacking, the intricate effects of pore edge chemistry remain poorly understood, as are mixture gas effects such as pore blocking, selective adsorption, and relative contributions from the surface to direct flow require better understanding, such that rational engineering membrane pore size and functionalization to achieve a desired permeance and selectivity, can be further advanced.

In my opinion, the fundamental benefits for graphene as a superior membrane material are sufficiently well established in terms of permeance, mechanical, thermal, and chemical stability, and promising routes of fabrication have been developed. Slowly, also membrane selectivities above polymeric materials are achieved with scalable processes. I am therefore convinced that graphene membranes are capable of living up to their promise to improve separation technologies with higher throughput, selectivity, and smaller device footprint, as well as lower energy costs.

Yet, the most urgent challenges now come to close the gap between membrane sizes successfully fabricated in lab-scale environments and membrane sizes required by industry. Depending on the application, these can range from 1 m^2 to 1000 m^2 per membrane and required membrane production capabilities far above 1 km^2 per year to establish market entry. This mismatch should be closed for a holistic graphene

8. *Conclusions & Outlook*

membrane fabrication process at competitive costs to truly leave the lab and bring benefit to society.

Additionally, high-performance membrane materials are rarely applied just by themselves but integrated into modules and processes, a task that is also inevitable.

Overall, I am therefore confident that the research field of graphene membranes for separation will continue to thrive, both fundamentally and applied. Fundamental studies will better understand the separation and permeation mechanisms and applied research to further refine fabrication methods for larger membrane scales and integration. Ultimately, this knowledge will enable engineering these high-performance membranes for the desired permeance and selectivity that are demanded by the respective applications, and fabrication will be integrated to roll-to-roll process lines such that the full potential of graphene as a membrane can be utilized for a better tomorrow.

References

- [1] David S. Sholl and Ryan P. Lively. Seven chemical separations to change the world. *Nature*, 532(7600):435–437, apr 2016.
- [2] Menachem Elimelech and William A. Phillip. The future of seawater desalination: Energy, technology, and the environment. *Science*, 333(6043):712–717, 2011.
- [3] Ahmad Fauzi Ismail, Kailash Chandra Khulbe, and Takeshi Matsuura. *Gas separation membranes: Polymeric and inorganic*. Springer International Publishing, Cham, 2015.
- [4] Richard W. Baker. Membrane Technology and Applications. In *Membrane Technology and Applications*, pages 303–324. John Wiley & Sons, Ltd, Chichester, UK, jul 2012.
- [5] Yuri Yampolskii and Benny Freeman. *Membrane Gas Separation*. John Wiley & Sons, Ltd, Chichester, UK, aug 2010.
- [6] K. S. Novoselov, A. K. Geim, S. V. Morozov, D. Jiang, Y. Zhang, S. V. Dubonos, I. V. Grigorieva, and A. A. Firsov. Electric field in atomically thin carbon films. *Science*, 306(5696):666–669, oct 2004.
- [7] A. K. Geim and K. S. Novoselov. The rise of graphene. *Nature Materials*, 6(3):183–191, mar 2007.

References

- [8] Alexander A. Balandin, Suchismita Ghosh, Wenzhong Bao, Irene Calizo, Desalegne Teweldebrhan, Feng Miao, and Chun Ning Lau. Superior thermal conductivity of single-layer graphene. *Nano Letters*, 8(3):902–907, 2008.
- [9] Changgu Lee, Xiaoding Wei, Jeffrey W. Kysar, and James Hone. Measurement of the elastic properties and intrinsic strength of monolayer graphene. *Science*, 321(5887):385–388, jul 2008.
- [10] Vikas Berry. Impermeability of graphene and its applications. *Carbon*, 62:1–10, 2013.
- [11] J. Scott Bunch, Scott S. Verbridge, Jonathan S. Alden, Arend M. Van Der Zande, Jeevak M. Parpia, Harold G. Craighead, and Paul L. McEuen. Impermeable atomic membranes from graphene sheets. *Nano Letters*, 8(8):2458–2462, 2008.
- [12] Myung E. Suk and N. R. Aluru. Water transport through ultrathin graphene. *Journal of Physical Chemistry Letters*, 1(10):1590–1594, 2010.
- [13] Kyaw Sint, Boyang Wang, and Petr Král. Selective ion passage through functionalized graphene nanopores. *Journal of the American Chemical Society*, 130(49):16448–16449, 2008.
- [14] De En Jiang, Valentino R. Cooper, and Sheng Dai. Porous graphene as the ultimate membrane for gas separation. *Nano Letters*, 9(12):4019–4024, dec 2009.
- [15] Stephen Pope. Turbulent flows By Pope. *Pope*, 2000.
- [16] Lyderic Bocquet and Elisabeth Charlaix. Nanofluidics, from bulk to interfaces. *Chemical Society Reviews*, 39(3):1073–1095, 2010.
- [17] Nikita Kavokine, Roland R Netz, and Lydéric Bocquet. Fluids at the Nanoscale: From Continuum to Subcontinuum Transport. *Annual Review of Fluid Mechanics*, pages 377–410, 2021.

- [18] R A Sampson. V. On Stokes's current function. *Proceedings of the Royal Society of London*, 49(296-301):46–53, 1891.
- [19] R. Roscoe. XXXI. The flow of viscous fluids round plane obstacles. *The London, Edinburgh, and Dublin Philosophical Magazine and Journal of Science*, 40(302):338–351, 1949.
- [20] Zeev Dagan, Sheldon Weinbaum, and Robert Pfeffer. An infinite-series solution for the creeping motion through an orifice of finite length. *Journal of Fluid Mechanics*, 115(Feb):505–523, 1982.
- [21] Stephen J. Blundell and Katherine M. Blundell. *Concepts in Thermal Physics*. Oxford University Press, oct 2009.
- [22] Martin Knudsen. Die Molekularströmung der Gase durch Öffnungen und die Effusion. *Annalen der Physik*, 333(5):999–1016, 1909.
- [23] Yafei Li, Zhen Zhou, Panwen Shen, and Zhongfang Chen. Two-dimensional polyphenylene: Experimentally available porous graphene as a hydrogen purification membrane. *Chemical Communications*, 46(21):3672–3674, may 2010.
- [24] Stephan Blankenburg, Marco Bieri, Roman Fasel, Klaus Müllen, Carlo A. Pignedoli, and Daniele Passerone. Porous graphene as an atmospheric nanofilter. *Small*, 6(20):2266–2271, oct 2010.
- [25] Andreas W. Hauser and Peter Schwerdtfeger. Methane-selective nanoporous graphene membranes for gas purification. *Physical Chemistry Chemical Physics*, 14(38):13292–13298, 2012.
- [26] Huailiang Du, Jingyuan Li, Jing Zhang, Gang Su, Xiaoyi Li, and Yuliang Zhao. Separation of hydrogen and nitrogen gases with porous graphene membrane. *Journal of Physical Chemistry C*, 115(47):23261–23266, 2011.

References

- [27] Joshua Schrier. Fluorinated and nanoporous graphene materials as sorbents for gas separations. *ACS Applied Materials and Interfaces*, 3(11):4451–4458, 2011.
- [28] Joshua Schrier. Carbon dioxide separation with a two-dimensional polymer membrane. *ACS Applied Materials and Interfaces*, 4(7):3745–3752, 2012.
- [29] Lee W. Drahushuk and Michael S. Strano. Mechanisms of gas permeation through single layer graphene membranes. *Langmuir*, 28(48):16671–16678, 2012.
- [30] Chengzhen Sun, Michael S.H. Boutilier, Harold Au, Pietro Poesio, Bofeng Bai, Rohit Karnik, and Nicolas G. Hadjiconstantinou. Mechanisms of molecular permeation through nanoporous graphene membranes. *Langmuir*, 30(2):675–682, 2014.
- [31] Meixia Shan, Qingzhong Xue, Nuannuan Jing, Cuicui Ling, Teng Zhang, Zifeng Yan, and Jingtang Zheng. Influence of chemical functionalization on the CO₂/N₂ separation performance of porous graphene membranes. *Nanoscale*, 4(17):5477–5482, 2012.
- [32] Kylene Solvik, Jessica A. Weaver, Anna M. Brockway, and Joshua Schrier. Entropy-driven molecular separations in 2D-nanoporous materials, with application to high-performance paraffin/olefin membrane separations. *Journal of Physical Chemistry C*, 117(33):17050–17057, 2013.
- [33] Chengzhen Sun and Bofeng Bai. Fast mass transport across two-dimensional graphene nanopores: Nonlinear pressure-dependent gas permeation flux. *Chemical Engineering Science*, 165:186–191, 2017.
- [34] Yong Wang, Qingyuan Yang, Chongli Zhong, and Jinping Li. Theoretical investigation of gas separation in functionalized nanoporous graphene membranes. *Applied Surface Science*, 407:532–539, jun 2017.

- [35] Boyao Wen, Chengzhen Sun, and Bofeng Bai. Inhibition effect of a non-permeating component on gas permeability of nanoporous graphene membranes. *Physical Chemistry Chemical Physics*, 17(36):23619–23626, 2015.
- [36] Steven P. Koenig, Luda Wang, John Pellegrino, and J. Scott Bunch. Selective molecular sieving through porous graphene. *Nature Nanotechnology*, 7(11):728–732, 2012.
- [37] Luda Wang, Lee W. Drahushuk, Lauren Cantley, Steven P. Koenig, Xinghui Liu, John Pellegrino, Michael S. Strano, and J. Scott Bunch. Molecular valves for controlling gas phase transport made from discrete ångström-sized pores in graphene. *Nature Nanotechnology*, 10(9):785–790, 2015.
- [38] Lee W. Drahushuk, Luda Wang, Steven P. Koenig, J. Scott Bunch, and Michael S. Strano. Analysis of time-varying, stochastic gas transport through graphene membranes. *ACS Nano*, 10(1):786–795, 2016.
- [39] Sukang Bae, Hyeongkeun Kim, Youngbin Lee, Xiangfan Xu, Jae Sung Park, Yi Zheng, Jayakumar Balakrishnan, Tian Lei, Hye Ri Kim, Young Il Song, Young Jin Kim, Kwang S. Kim, Barbaros Özyilmaz, Jong Hyun Ahn, Byung Hee Hong, and Sumio Iijima. Roll-to-roll production of 30-inch graphene films for transparent electrodes. *Nature Nanotechnology*, 5(8):574–578, 2010.
- [40] J. Zhao, G. He, S. Huang, L. F. Villalobos, M. Dakhchoune, H. Bassas, and K. V. Agrawal. Etching gas-sieving nanopores in single-layer graphene with an angstrom precision for high-performance gas mixture separation. *Science Advances*, 5(1):1–10, 2019.
- [41] Michael S.H. Boutilier, Chengzhen Sun, Sean C. O’Hern, Harold Au, Nicolas G. Hadjiconstantinou, and Rohit Karnik. Implications of permeation through intrinsic defects in graphene on the

References

- design of defect-tolerant membranes for gas separation. *ACS Nano*, 8(1):841–849, 2014.
- [42] Michael S.H. Boutilier, Nicolas G. Hadjiconstantinou, and Rohit Karnik. Knudsen effusion through polymer-coated three-layer porous graphene membranes. *Nanotechnology*, 28(18):184003, 2017.
- [43] Michael S.H. Boutilier, Doojoon Jang, Juan Carlos Idrobo, Piran R. Kidambi, Nicolas G. Hadjiconstantinou, and Rohit Karnik. Molecular Sieving Across Centimeter-Scale Single-Layer Nanoporous Graphene Membranes. *ACS Nano*, 11(6):5726–5736, 2017.
- [44] Kek Kiong Tio and Satwindar Singh Sadhal. Boundary conditions for stokes flows near a porous membrane. *Applied Scientific Research*, 52(1):1–20, 1994.
- [45] Kemal Celebi, Jakob Buchheim, Roman M. Wyss, Amirhossein Droudian, Patrick Gasser, Ivan Shorubalko, Jeong Il Kye, Changho Lee, and Hyung Gyu Park. Ultimate permeation across atomically thin porous graphene. *Science*, 344(6181):289–292, 2014.
- [46] Recep Zan, Quentin M. Ramasse, Ursel Bangert, and Konstantin S. Novoselov. Graphene reknits its holes. *Nano Letters*, 12(8):3936–3940, 2012.
- [47] Jaekwang Lee, Zhiqing Yang, Wu Zhou, Stephen J. Pennycook, Sokrates T. Pantelides, and Matthew F. Chisholm. Stabilization of graphene nanopore. *Proceedings of the National Academy of Sciences of the United States of America*, 111(21):7522–7526, 2014.
- [48] Kuang He, Alex W. Robertson, Chuncheng Gong, Christopher S. Allen, Qiang Xu, Henny Zandbergen, Jeffrey C. Grossman, Angus I. Kirkland, and Jamie H. Warner. Controlled formation

- of closed-edge nanopores in graphene. *Nanoscale*, 7(27):11602–11610, 2015.
- [49] Ho Bum Park, Jovan Kamcev, Lloyd M. Robeson, Menachem Elimelech, and Benny D. Freeman. Maximizing the right stuff: The trade-off between membrane permeability and selectivity. *Science*, 356(6343):1138–1148, 2017.
- [50] Jason K. Holt, Hyung Gyu Park, Yinmin Wang, Michael Stadermann, Alexander B. Artyukhin, Costas P. Grigoropoulos, Aleksandr Noy, and Olgica Bakajin. Fast mass transport through sub-2-nanometer carbon nanotubes. *Science*, 312(5776):1034–1037, 2006.
- [51] Itsuo Hanasaki and Akihiro Nakatani. Flow structure of water in carbon nanotubes: Poiseuille type or plug-like? *Journal of Chemical Physics*, 124(14), 2006.
- [52] M. E. Suk and N. R. Aluru. Molecular and continuum hydrodynamics in graphene nanopores. *RSC Advances*, 3(24):9365–9372, 2013.
- [53] Zhao Qin and Markus J. Buehler. Nonlinear Viscous Water at Nanoporous Two-Dimensional Interfaces Resists High-Speed Flow through Cooperativity. *Nano Letters*, 15(6):3939–3944, 2015.
- [54] David Cohen-Tanugi and Jeffrey C. Grossman. Water desalination across nanoporous graphene. *Nano Letters*, 12(7):3602–3608, 2012.
- [55] Sumedh P. Surwade, Sergei N. Smirnov, Ivan V. Vlassiuk, Raymond R. Unocic, Gabriel M. Veith, Sheng Dai, and Shannon M. Mahurin. Water desalination using nanoporous single-layer graphene. *Nature Nanotechnology*, 10(5):459–464, may 2015.

References

- [56] Sean C. O’Hern, Doojoon Jang, Suman Bose, Juan Carlos Idrobo, Yi Song, Tahar Laoui, Jing Kong, and Rohit Karnik. Nanofiltration across defect-sealed nanoporous monolayer graphene. *Nano Letters*, 15(5):3254–3260, may 2015.
- [57] David Cohen-Tanugi and Jeffrey C. Grossman. Water permeability of nanoporous graphene at realistic pressures for reverse osmosis desalination. *Journal of Chemical Physics*, 141(7):74704, 2014.
- [58] Mohammad Heiranian, Amir Barati Farimani, and Narayana R. Aluru. Water desalination with a single-layer MoS₂ nanopore. *Nature Communications*, 6:8616, 2015.
- [59] Shijun Zhao, Jianming Xue, and Wei Kang. Ion selection of charge-modified large nanopores in a graphene sheet. *Journal of Chemical Physics*, 139(11):114702, 2013.
- [60] Myung E. Suk and N. R. Aluru. Ion transport in sub-5-nm graphene nanopores. *Journal of Chemical Physics*, 140(8):84707, 2014.
- [61] Zhongjin He, Jian Zhou, Xiaohua Lu, and Ben Corry. Bioinspired graphene nanopores with voltage-tunable ion selectivity for Na⁺ and K⁺. *ACS Nano*, 7(11):10148–10157, 2013.
- [62] S. Garaj, W. Hubbard, A. Reina, J. Kong, D. Branton, and J. A. Golovchenko. Graphene as a subnanometre trans-electrode membrane. *Nature*, 467(7312):190–193, 2010.
- [63] Tarun Jain, Benjamin C. Raser, Ricardo Jose S. Guerrero, Michael S.H. Boutilier, Sean C. O’Hern, Juan Carlos Idrobo, and Rohit Karnik. Heterogeneous sub-continuum ionic transport in statistically isolated graphene nanopores. *Nature Nanotechnology*, 10(12):1053–1057, 2015.
- [64] Jiandong Feng, Ke Liu, Michael Graf, Dumitru Dumcenco, Andras Kis, Massimiliano Di Ventra, and Aleksandra Radenovic.

- Observation of ionic Coulomb blockade in nanopores. *Nature Materials*, 15(8):850–855, 2016.
- [65] Jiandong Feng, Michael Graf, Ke Liu, Dmitry Ovchinnikov, Dumitru Dumcenco, Mohammad Heiranian, Vishal Nandigana, Narayana R. Aluru, Andras Kis, and Aleksandra Radenovic. Single-layer MoS₂ nanopores as nanopower generators. *Nature*, 536(7615):197–200, 2016.
- [66] A. Gadaleta, C. Sempere, S. Gravelle, A. Siria, R. Fulcrand, C. Ybert, and L. Bocquet. Sub-additive ionic transport across arrays of solid-state nanopores. *Physics of Fluids*, 26(1), 2014.
- [67] Ryan C. Rollings, Aaron T. Kuan, and Jene A. Golovchenko. Ion selectivity of graphene nanopores. *Nature Communications*, 7:11408, 2016.
- [68] Sean C. O’Hern, Michael S.H. Boutilier, Juan Carlos Idrobo, Yi Song, Jing Kong, Tahar Laoui, Muataz Atieh, and Rohit Karnik. Selective ionic transport through tunable subnanometer pores in single-layer graphene membranes. *Nano Letters*, 14(3):1234–1241, 2014.
- [69] Sean C. O’Hern, Cameron A. Stewart, Michael S.H. Boutilier, Juan Carlos Idrobo, Sreekar Bhaviripudi, Sarit K. Das, Jing Kong, Tahar Laoui, Muataz Atieh, and Rohit Karnik. Selective molecular transport through intrinsic defects in a single layer of CVD graphene. *ACS Nano*, 6(11):10130–10138, 2012.
- [70] Piran R. Kidambi, Rebekah A. Terry, Luda Wang, Michael S.H. Boutilier, Doojoon Jang, Jing Kong, and Rohit Karnik. Assessment and control of the impermeability of graphene for atomically thin membranes and barriers. *Nanoscale*, 9(24):8496–8507, 2017.
- [71] Meng Miao, Marco Buongiorno Nardelli, Qi Wang, and Yingchun Liu. First principles study of the permeability of

References

- graphene to hydrogen atoms. *Physical Chemistry Chemical Physics*, 15(38):16132–16137, 2013.
- [72] S. Hu, M. Lozada-Hidalgo, F. C. Wang, A. Mishchenko, F. Schedin, R. R. Nair, E. W. Hill, D. W. Boukhvalov, M. I. Katsnelson, R. A.W. Dryfe, I. V. Grigorieva, H. A. Wu, and A. K. Geim. Proton transport through one-atom-thick crystals. *Nature*, 516(7530):227–230, 2014.
- [73] Jennifer L. Achtyl, Raymond R. Unocic, Lijun Xu, Yu Cai, Muralikrishna Raju, Weiwei Zhang, Robert L. Sacci, Ivan V. Vlasiouk, Pasquale F. Fulvio, Panchapakesan Ganesh, David J. Wesolowski, Sheng Dai, Adri C.T. Van Duin, Matthew Neurock, and Franz M. Geiger. Aqueous proton transfer across single-layer graphene. *Nature Communications*, 6:6539, 2015.
- [74] Michael I. Walker, Philipp Braeuninger-Weimer, Robert S. Weatherup, Stephan Hofmann, and Ulrich F. Keyser. Measuring the proton selectivity of graphene membranes. *Applied Physics Letters*, 107(21):213104, nov 2015.
- [75] Igor Poltavsky, Limin Zheng, Majid Mortazavi, and Alexandre Tkatchenko. Quantum tunneling of thermal protons through pristine graphene. *Journal of Chemical Physics*, 148(20):1–5, 2018.
- [76] Max Seel and Ravindra Pandey. Proton and hydrogen transport through two-dimensional monolayers. *2D Materials*, 3(2):0, 2016.
- [77] Qiuju Zhang, Minggang Ju, Liang Chen, and Xiao Cheng Zeng. Differential Permeability of Proton Isotopes through Graphene and Graphene Analogue Monolayer. *Journal of Physical Chemistry Letters*, 7(17):3395–3400, 2016.
- [78] M. Lozada-Hidalgo, S. Hu, O. Marshall, A. Mishchenko, A. N. Grigorenko, R. A.W. Dryfe, B. Radha, I. V. Grigorieva, and

- A. K. Geim. Sieving hydrogen isotopes through two-dimensional crystals. *Science*, 351(6268):68–70, 2016.
- [79] Le Shi, Ao Xu, Guanhua Chen, and Tianshou Zhao. Theoretical Understanding of Mechanisms of Proton Exchange Membranes Made of 2D Crystals with Ultrahigh Selectivity. *Journal of Physical Chemistry Letters*, 8(18):4354–4361, 2017.
- [80] J. M.H. Kroes, A. Fasolino, and M. I. Katsnelson. Density functional based simulations of proton permeation of graphene and hexagonal boron nitride. *Physical Chemistry Chemical Physics*, 19(8):5813–5817, 2017.
- [81] L. Tsetseris and S. T. Pantelides. Graphene: An impermeable or selectively permeable membrane for atomic species? *Carbon*, 67:58–63, 2014.
- [82] M. Lozada-Hidalgo, S. Zhang, S. Hu, A. Esfandiar, I. V. Grigorieva, and A. K. Geim. Scalable and efficient separation of hydrogen isotopes using graphene-based electrochemical pumping. *Nature Communications*, 8(May):15215, 2017.
- [83] Wei L. Wang and Efthimios Kaxiras. Graphene hydrate: theoretical prediction of a new insulating form of graphene. *New Journal of Physics*, 12(12):125012, dec 2010.
- [84] B. Radha, A. Esfandiar, F. C. Wang, A. P. Rooney, K. Gopinadhan, A. Keerthi, A. Mishchenko, A. Janardanan, P. Blake, L. Fumagalli, M. Lozada-Hidalgo, S. Garaj, S. J. Haigh, I. V. Grigorieva, H. A. Wu, and A. K. Geim. Molecular transport through capillaries made with atomic-scale precision. *Nature*, 538(7624):222–225, 2016.
- [85] Luda Wang, Christopher M. Williams, Michael S.H. Boutilier, Piran R. Kidambi, and Rohit Karnik. Single-Layer Graphene Membranes Withstand Ultrahigh Applied Pressure. *Nano Letters*, 17(5):3081–3088, 2017.

References

- [86] David Cohen-Tanugi and Jeffrey C. Grossman. Mechanical strength of nanoporous graphene as a desalination membrane. *Nano Letters*, 14(11):6171–6178, 2014.
- [87] Stefan Howorka. Building membrane nanopores. *Nature Nanotechnology*, 12(7):619–630, 2017.
- [88] Jay R. Werber, Chinedum O. Osuji, and Menachem Elimelech. Materials for next-generation desalination and water purification membranes. *Nature Reviews Materials*, 1(5):16018, apr 2016.
- [89] Mark A. Shannon, Paul W. Bohn, Menachem Elimelech, John G. Georgiadis, Benito J. Mariñas, and Anne M. Mayes. Science and technology for water purification in the coming decades. *Nature*, 452(7185):301–310, 2008.
- [90] M. Ulbricht. Introduction to Membrane Science and Technology. Von H. Strathmann. *Chemie Ingenieur Technik*, 85(10):1643–1644, 2013.
- [91] Gaoliang Wei, Xie Quan, Shuo Chen, and Hongtao Yu. Super-permeable Atomic-Thin Graphene Membranes with High Selectivity. *ACS Nano*, 11(2):1920–1926, 2017.
- [92] Martha K. Small and W. D. Nix. Analysis of the accuracy of the bulge test in determining the mechanical properties of thin films. *Journal of Materials Research*, 7(6):1553–1563, 1992.
- [93] Eleonora Secchi, Sophie Marbach, Antoine Niguès, Derek Stein, Alessandro Siria, and Lydéric Bocquet. Massive radius-dependent flow slippage in carbon nanotubes. *Nature*, 537(7619):210–213, 2016.
- [94] Jakob Buchheim. *Graphene membranes synthesis and mass transport across atomic thickness porous membranes*. PhD thesis, ETH Zurich, 2016.

- [95] Carlos S. Ruiz-Vargas, Houlong L. Zhuang, Pinshane Y. Huang, Arend M. van der Zande, Shivank Garg, Paul L. McEuen, David A. Muller, Richard G. Hennig, and Jiwoong Park. Softened Elastic Response and Unzipping in Chemical Vapor Deposition Graphene Membranes. *Nano Letters*, 11(6):2259–2263, jun 2011.
- [96] J. HERMIA. Constant Pressure Blocking Filtration Laws - Application Topower-Law Non-Newtonian Fluids. *Trans Inst Chem Eng*, V 60(N 3):183–187, 1982.
- [97] W. R. Bowen, J. I. Calvo, and A. Hernández. Steps of membrane blocking in flux decline during protein microfiltration. *Journal of Membrane Science*, 101(1-2):153–165, 1995.
- [98] Xinran Wang, Scott M. Tabakman, and Hongjie Dai. Atomic layer deposition of metal oxides on pristine and functionalized graphene. *Journal of the American Chemical Society*, 130(26):8152–8153, 2008.
- [99] Zhiwei Xu, Mengyao Yue, Lei Chen, Baoming Zhou, Mingjing Shan, Jiarong Niu, Baodong Li, and Xiaoming Qian. A facile preparation of edge etching, porous and highly reactive graphene nanosheets via ozone treatment at a moderate temperature. *Chemical Engineering Journal*, 240:187–194, 2014.
- [100] Simon Gravelle, Laurent Joly, Christophe Ybert, and Lydéric Bocquet. Large permeabilities of hourglass nanopores: From hydrodynamics to single file transport. *Journal of Chemical Physics*, 141(18):18C526, 2014.
- [101] Kaare H. Jensen, André X.C.N. Valente, and Howard A. Stone. Flow rate through microfilters: Influence of the pore size distribution, hydrodynamic interactions, wall slip, and inertia. *Physics of Fluids*, 26(5):52004, 2014.

References

- [102] Simon Gravelle, Laurent Joly, François Detcheverry, Christophe Ybert, Cécile Cottin-Bizonne, and Lydéric Bocquet. Optimizing water permeability through the hourglass shape of aquaporins. *Proceedings of the National Academy of Sciences of the United States of America*, 110(41):16367–16372, 2013.
- [103] Thomas B. Sisan and Seth Lichter. The end of nanochannels. *Microfluidics and Nanofluidics*, 11(6):787–791, 2011.
- [104] Harold L. Weissberg. End correction for slow viscous flow through long tubes. *Physics of Fluids*, 5(9):1033–1036, 1962.
- [105] J. Happel and H. Brenner. *Low Reynolds number hydrodynamics - with special applications to particulate media.*, volume 1. Springer Science & Business Media, 1983.
- [106] J. Crank. *The mathematics of diffusion. 2nd Edn.* Clarendon Press, 1957.
- [107] Lukas Madauß, Jens Schumacher, Mandakranta Ghosh, Oliver Ochedowski, Jens Meyer, Henning Lebius, Brigitte Ban-D’Etat, Maria Eugenia Toimil-Molares, Christina Trautmann, Rob G.H. Lammertink, Mathias Ulbricht, and Marika Schleberger. Fabrication of nanoporous graphene/polymer composite membranes. *Nanoscale*, 9(29):10487–10493, 2017.
- [108] Thomas R. Gaborski, Jessica L. Snyder, Christopher C. Striemer, David Z. Fang, Michael Hoffman, Philippe M. Fauchet, and James L. McGrath. High-performance separation of nanoparticles with ultrathin porous nanocrystalline silicon membranes. *ACS Nano*, 4(11):6973–6981, 2010.
- [109] Yang Yang, Petr Dementyev, Niklas Biere, Daniel Emmrich, Patrick Stohmann, Riko Korzetz, Xianghui Zhang, André Beyer, Sascha Koch, Dario Anselmetti, and Armin Götzhäuser. Rapid Water Permeation Through Carbon Nanomembranes with Sub-Nanometer Channels. *ACS Nano*, 12(5):4695–4701, 2018.

- [110] Jens H. Walther, Konstantinos Ritos, Eduardo R. Cruz-Chu, Constantine M. Megaridis, and Petros Koumoutsakos. Barriers to superfast water transport in carbon nanotube membranes. *Nano Letters*, 13(5):1910–1914, 2013.
- [111] Mainak Majumder, Nitin Chopra, Rodney Andrews, and Bruce J. Hinds. Nanoscale hydrodynamics: Enhanced flow in carbon nanotubes. *Nature*, 438(7064):44, 2005.
- [112] Feng Du, Liangti Qu, Zhenhai Xia, Lianfang Feng, and Liming Dai. Membranes of vertically aligned superlong carbon nanotubes. *Langmuir*, 27(13):8437–8443, 2011.
- [113] Fangqiang Zhu, Emad Tajkhorshid, and Klaus Schulten. Pressure-induced water transport in membrane channels studied by molecular dynamics. *Biophysical Journal*, 83(1):154–160, 2002.
- [114] Yi Wang, Klaus Schulten, and Emad Tajkhorshid. What makes an aquaporin a glycerol channel? A comparative study of AqpZ and GlpF. *Structure*, 13(8):1107–1118, aug 2005.
- [115] T. Walz, B. L. Smith, M. L. Zeidel, A. Engel, and P. Agre. Biologically active two-dimensional crystals of aquaporin CHIP. *Journal of Biological Chemistry*, 269(3):1583–1586, 1994.
- [116] Mainak Majumder, Nitin Chopra, and Bruce J. Hinds. Mass transport through carbon nanotube membranes in three different regimes: Ionic diffusion and gas and liquid flow. *ACS Nano*, 5(5):3867–3877, 2011.
- [117] Alberto Striolo. The mechanism of water diffusion in narrow carbon nanotubes. *Nano Letters*, 6(4):633–639, 2006.
- [118] John A. Thomas and Alan J.H. McGaughey. Water flow in carbon nanotubes: Transition to subcontinuum transport. *Physical Review Letters*, 102(18):184502, 2009.

References

- [119] Kerstin Falk, Felix Sedlmeier, Laurent Joly, Roland R. Netz, and Lydéric Bocquet. Molecular origin of fast water transport in carbon nanotube membranes: Superlubricity versus curvature dependent friction. *Nano Letters*, 10(10):4067–4073, 2010.
- [120] Ming Ma, François Grey, Luming Shen, Michael Urbakh, Shuai Wu, Jefferson Zhe Liu, Yilun Liu, and Quanshui Zheng. Water transport inside carbon nanotubes mediated by phonon-induced oscillating friction. *Nature Nanotechnology*, 10(8):692–695, 2015.
- [121] Zhe Yuan, Jesse D. Benck, Yannick Eatmon, Daniel Blankshtein, and Michael S. Strano. Stable, Temperature-Dependent Gas Mixture Permeation and Separation through Suspended Nanoporous Single-Layer Graphene Membranes. *Nano Letters*, 18(8):5057–5069, aug 2018.
- [122] Shiqi Huang, Mostapha Dakhchoune, Wen Luo, Emad Oveisi, Guangwei He, Mojtaba Rezaei, Jing Zhao, Duncan T.L. Alexander, Andreas Züttel, Michael S. Strano, and Kumar Varoon Agrawal. Single-layer graphene membranes by crack-free transfer for gas mixture separation. *Nature Communications*, 9(1):1–11, 2018.
- [123] Majharul Haque Khan, Mina Moradi, Mostapha Dakhchoune, Mojtaba Rezaei, S. Huang, Jing Zhao, and Kumar Varoon Agrawal. Hydrogen sieving from intrinsic defects of benzene-derived single-layer graphene. *Carbon*, 153:458–466, 2019.
- [124] Fernando Vallejos-Burgos, François Xavier Coudert, and Katsumi Kaneko. Air separation with graphene mediated by nanowindow-rim concerted motion. *Nature Communications*, 9(1):1–9, 2018.
- [125] Chengzhen Sun and Bofeng Bai. Molecular sieving through a graphene nanopore: non-equilibrium molecular dynamics simulation. *Science Bulletin*, 62(8):554–562, 2017.

- [126] Chengzhen Sun and Bofeng Bai. Gas diffusion on graphene surfaces. *Physical Chemistry Chemical Physics*, 19(5):3894–3902, 2017.
- [127] Luda Wang, Michael S.H. Boutilier, Piran R. Kidambi, Doo-joon Jang, Nicolas G. Hadjiconstantinou, and Rohit Karnik. Fundamental transport mechanisms, fabrication and potential applications of nanoporous atomically thin membranes. *Nature Nanotechnology*, 12(6):509–522, 2017.
- [128] K. P. Schlichting and H. G. Park. Chapter 3: Mass Transport Across Atomically Thin Membranes. In *RSC Nanoscience and Nanotechnology*, volume 2019 of *Nanoscience & Nanotechnology Series*, pages 43–75. The Royal Society of Chemistry, 2019.
- [129] Zhe Yuan, Ananth Govind Rajan, Rahul Prasanna Misra, Lee W. Drahushuk, Kumar Varoon Agrawal, Michael S. Strano, and Daniel Blankshtein. Mechanism and Prediction of Gas Permeation through Sub-Nanometer Graphene Pores: Comparison of Theory and Simulation. *ACS Nano*, 11(8):7974–7987, aug 2017.
- [130] Zhe Yuan, Rahul Prasanna Misra, Ananth Govind Rajan, Michael S. Strano, and Daniel Blankshtein. Analytical prediction of gas permeation through graphene nanopores of varying sizes: Understanding transitions across multiple transport regimes. *ACS Nano*, 13(10):11825–11833, 2019.
- [131] Marco Bieri, Matthias Treier, Jinming Cai, Kamel Ait-Mansour, Pascal Ruffieux, Oliver Gröning, Pierangelo Gröning, Marcel Kastler, Ralph Rieger, Xinliang Feng, Klaus Müllen, and Roman Fasel. Porous graphenes: Two-dimensional polymer synthesis with atomic precision. *Chemical Communications*, (45):6919–6921, 2009.
- [132] César Moreno, Manuel Vilas-Varela, Bernhard Kretz, Aran Garcia-Lekue, Marius V. Costache, Markos Paradinas, Mirko

References

- Panighel, Gustavo Ceballos, Sergio O. Valenzuela, Diego Peña, and Aitor Mugarza. Bottom-up synthesis of multifunctional nanoporous graphene. *Science*, 360(6385):199–203, 2018.
- [133] Christof Neumann, David Kaiser, Michael J. Mohn, Matthias Fuser, Nils Eike Weber, Oliver Reimer, Armin Golzhauser, Thomas Weimann, Andreas Terfort, Ute Kaiser, and Andrey Turchanin. Bottom-Up Synthesis of Graphene Monolayers with Tunable Crystallinity and Porosity. *ACS Nano*, 13(6):7310–7322, 2019.
- [134] Kyoungjun Choi, Amirhossein Droudian, Roman M. Wyss, Karl Philipp Schlichting, and Hyung Gyu Park. Multifunctional wafer-scale graphene membranes for fast ultrafiltration and high permeation gas separation. *Science Advances*, 4(11):1–10, nov 2018.
- [135] Sung Soo Kim, Myung Jin Park, Jeong Hee Kim, Gwanghyun Ahn, Sunmin Ryu, Byung Hee Hong, and Byeong Hyeok Sohn. Strain-Assisted Wafer-Scale Nanoperforation of Single-Layer Graphene by Arrayed Pt Nanoparticles. *Chemistry of Materials*, 27(20):7003–7010, 2015.
- [136] O. Lehtinen, J. Kotakoski, A. V. Krasheninnikov, A. Tolvanen, K. Nordlund, and J. Keinonen. Effects of ion bombardment on a two-dimensional target: Atomistic simulations of graphene irradiation. *Physical Review B - Condensed Matter and Materials Physics*, 81(15):153401, apr 2010.
- [137] O. Lehtinen, J. Kotakoski, A. V. Krasheninnikov, and J. Keinonen. Cutting and controlled modification of graphene with ion beams. *Nanotechnology*, 22(17):175306, apr 2011.
- [138] Christopher J. Russo and J. A. Golovchenko. Atom-by-atom nucleation and growth of graphene nanopores. *Proceedings of the National Academy of Sciences of the United States of America*, 109(16):5953–5957, apr 2012.

- [139] Jakob Buchheim, Karl Philipp Schlichting, Roman M. Wyss, and Hyung Gyu Park. Assessing the Thickness-Permeation Paradigm in Nanoporous Membranes. *ACS Nano*, 13(1):134–142, 2019.
- [140] Joachim Dahl Thomsen, Jens Kling, David M.A. MacKenzie, Peter Bøggild, and Timothy J. Booth. Oxidation of suspended graphene: Etch dynamics and stability beyond 1000 °c. *ACS Nano*, 13(2):2281–2288, 2019.
- [141] Johan M. Carlsson, Felix Hanke, Suljo Linic, and Matthias Scheffler. Two-Step Mechanism for Low-Temperature Oxidation of Vacancies in Graphene. *Physical Review Letters*, 102(16):1–4, 2009.
- [142] Caroline A. Schneider, Wayne S. Rasband, and Kevin W. Eliceiri. NIH Image to ImageJ: 25 years of image analysis. *Nature Methods*, 9(7):671–675, 2012.
- [143] Jothi Priyanka Thiruraman, Paul Masih Das, and Marija Drndić. Irradiation of Transition Metal Dichalcogenides Using a Focused Ion Beam: Controlled Single-Atom Defect Creation. *Advanced Functional Materials*, 29(52):1904668, dec 2019.
- [144] L. M. Malard, M. A. Pimenta, G. Dresselhaus, and M. S. Dresselhaus. Raman spectroscopy in graphene. *Physics Reports*, 473(5-6):51–87, 2009.
- [145] M. M. Lucchese, F. Stavale, E. H. Martins Ferreira, C. Vilani, M. V.O. Moutinho, Rodrigo B. Capaz, C. A. Achete, and A. Jorio. Quantifying ion-induced defects and Raman relaxation length in graphene. *Carbon*, 48(5):1592–1597, 2010.
- [146] E. H. Martins Ferreira, Marcus V.O. Moutinho, F. Stavale, M. M. Lucchese, Rodrigo B. Capaz, C. A. Achete, and A. Jorio. Evolution of the Raman spectra from single-, few-, and many-layer graphene with increasing disorder. *Physical Review B - Condensed Matter and Materials Physics*, 82(12), 2010.

References

- [147] Jon Zubeltzu, Andrey Chuvilin, Fabiano Corsetti, Amaia Zurutuza, and Emilio Artacho. Knock-on damage in bilayer graphene: Indications for a catalytic pathway. *Physical Review B - Condensed Matter and Materials Physics*, 88(24):245407, dec 2013.
- [148] E. L. C. and Philip R. Bevington. Data Reduction and Error Analysis for the Physical Sciences. *Journal of the American Statistical Association*, 67(337):249, mar 1972.
- [149] Guangping Lei, Chao Liu, Hui Xie, and Fenhong Song. Separation of the hydrogen sulfide and methane mixture by the porous graphene membrane: Effect of the charges. *Chemical Physics Letters*, 599:127–132, 2014.
- [150] Aaron W. Thornton, Tamsyn Hilder, Anita J. Hill, and James M. Hill. Predicting gas diffusion regime within pores of different size, shape and composition. *Journal of Membrane Science*, 336(1-2):101–108, 2009.
- [151] R. D. Present and A. J. Debethune. Separation of a gas mixture flowing through a long tube at low pressure. *Physical Review*, 75(7):1050–1057, 1949.
- [152] Lloyd M. Robeson. The upper bound revisited. *Journal of Membrane Science*, 320(1-2):390–400, 2008.
- [153] Zixi Kang, Ming Xue, Lili Fan, Lin Huang, Lijia Guo, Guoying Wei, Banglin Chen, and Shilun Qiu. Highly selective sieving of small gas molecules by using an ultra-microporous metal-organic framework membrane. *Energy and Environmental Science*, 7(12):4053–4060, 2014.
- [154] Feng Zhang, Xiaoqin Zou, Xue Gao, Songjie Fan, Fuxing Sun, Hao Ren, and Guangshan Zhu. Hydrogen selective NH₂-MIL-53(Al) MOF membranes with high permeability. *Advanced Functional Materials*, 22(17):3583–3590, 2012.

- [155] Chen Zhou, Chenfang Yuan, Yaqiong Zhu, Jürgen Caro, and Aisheng Huang. Facile synthesis of zeolite FAU molecular sieve membranes on bio-adhesive polydopamine modified Al₂O₃ tubes. *Journal of Membrane Science*, 494:174–181, 2015.
- [156] Halil Kalipcilar, Travis C. Bowen, Richard D. Noble, and John L. Falconer. Synthesis and separation performance of SSZ-13 zeolite membranes on tubular supports. *Chemistry of Materials*, 14(8):3458–3464, 2002.
- [157] Jingjing Yang, Dian Gong, Guihua Li, Gaofeng Zeng, Qiyang Wang, Yelei Zhang, Guojuan Liu, Ping Wu, Evgeny Vovk, Zheng Peng, Xiaohong Zhou, Yong Yang, Zhi Liu, and Yuhan Sun. Self-Assembly of Thiourea-Crosslinked Graphene Oxide Framework Membranes toward Separation of Small Molecules. *Advanced Materials*, 30(16):e1705775, 2018.
- [158] Hang Li, Zhuonan Song, Xiaojie Zhang, Yi Huang, Shiguang Li, Yating Mao, Harry J. Ploehn, Yu Bao, and Miao Yu. Ultra-thin, molecular-sieving graphene oxide membranes for selective hydrogen separation. *Science*, 342(6154):95–98, 2013.
- [159] Hui Hsin Tseng, Ching Ting Wang, Guo Liang Zhuang, Petr Uchytíl, Jirina Reznickova, and Katka Setnickova. Enhanced H₂/CH₄ and H₂/CO₂ separation by carbon molecular sieve membrane coated on titania modified alumina support: Effects of TiO₂ intermediate layer preparation variables on interfacial adhesion. *Journal of Membrane Science*, 510:391–404, 2016.
- [160] Chen Zhang and William J. Koros. Ultraselective Carbon Molecular Sieve Membranes with Tailored Synergistic Sorption Selective Properties. *Advanced Materials*, 29(33):1–6, 2017.
- [161] Priya Banerjee, Rasel Das, Papita Das, and Aniruddha Mukhopadhyay. Membrane technology. In *Carbon Nanostructures*, pages 127–150. Wiley Online Library, 2018.

References

- [162] P. Z. Sun, Q. Yang, W. J. Kuang, Y. V. Stebunov, W. Q. Xiong, J. Yu, R. R. Nair, M. I. Katsnelson, S. J. Yuan, I. V. Grigorieva, M. Lozada-Hidalgo, F. C. Wang, and A. K. Geim. Limits on gas impermeability of graphene. *Nature*, 579(7798):229–232, mar 2020.
- [163] Michael D. Fischbein and Marija Drndić. Electron beam nanosculpting of suspended graphene sheets. *Applied Physics Letters*, 93(11):2006–2009, 2008.
- [164] Peifu Cheng, Mattigan M. Kelly, Nicole K. Moehring, Wonhee Ko, An Ping Li, Juan Carlos Idrobo, Michael S.H. Boutilier, and Piran R. Kidambi. Facile Size-Selective Defect Sealing in Large-Area Atomically Thin Graphene Membranes for Sub-Nanometer Scale Separations. *Nano Letters*, 20(8):5951–5959, 2020.
- [165] Karl Philipp Schlichting and Dimos Poulikakos. Selective Etching of Graphene Membrane Nanopores: From Molecular Sieving to Extreme Permeance. *ACS Applied Materials and Interfaces*, 12(32):36468–36477, jul 2020.
- [166] Piran R. Kidambi, Doojoon Jang, Juan Carlos Idrobo, Michael S.H. Boutilier, Luda Wang, Jing Kong, and Rohit Karnik. Nanoporous Atomically Thin Graphene Membranes for Desalting and Dialysis Applications. *Advanced Materials*, 29(33):1700277, sep 2017.
- [167] Piran R. Kidambi, Michael S.H. Boutilier, Luda Wang, Doojoon Jang, Jeehwan Kim, and Rohit Karnik. Selective Nanoscale Mass Transport across Atomically Thin Single Crystalline Graphene Membranes. *Advanced Materials*, 29(19), 2017.
- [168] Yanzhe Qin, Yongyou Hu, Stephan Koehler, Liheng Cai, Junjie Wen, Xiaojun Tan, Weiwei L. Xu, Qian Sheng, Xu Hou, Jianming Xue, Miao Yu, and David Weitz. Ultrafast Nanofiltration through Large-Area Single-Layered Graphene Membranes. *ACS Applied Materials and Interfaces*, 9(11):9239–9244, mar 2017.

- [169] Yanbing Yang, Xiangdong Yang, Ling Liang, Yuyan Gao, Huanyu Cheng, Xinming Li, Mingchu Zou, Anyuan Cao, Renzhi Ma, Quan Yuan, and Xiangfeng Duan. Large-area graphene-nanomesh/ carbon-nanotube hybrid membranes for ionic and molecular nanofiltration. *Science*, 364(6445):1057–1062, jun 2019.
- [170] Piran R. Kidambi, Dhanushkodi D. Mariappan, Nicholas T. Dee, Andrey Vyatskikh, Sui Zhang, Rohit Karnik, and A. John Hart. A Scalable Route to Nanoporous Large-Area Atomically Thin Graphene Membranes by Roll-to-Roll Chemical Vapor Deposition and Polymer Support Casting. *ACS Applied Materials and Interfaces*, 10(12):10369–10378, mar 2018.
- [171] Yu Wang, Yi Zheng, Xiangfan Xu, Emilie Dubuisson, Qiaoliang Bao, Jiong Lu, and Kian Ping Loh. Electrochemical delamination of CVD-grown graphene film: Toward the recyclable use of copper catalyst. *ACS Nano*, 5(12):9927–9933, 2011.
- [172] Lai Peng Ma, Wencai Ren, and Hui Ming Cheng. Transfer Methods of Graphene from Metal Substrates: A Review. *Small Methods*, 3(7):1900049, 2019.
- [173] Yung Chang Lin, Chuanhong Jin, Jung Chi Lee, Shou Feng Jen, Kazu Suenaga, and Po Wen Chiu. Clean transfer of graphene for isolation and suspension. *ACS Nano*, 5(3):2362–2368, 2011.
- [174] Yung Chang Lin, Chun Chieh Lu, Chao Huei Yeh, Chuanhong Jin, Kazu Suenaga, and Po Wen Chiu. Graphene annealing: How clean can it be? *Nano Letters*, 12(1):414–419, 2012.
- [175] Xuelei Liang, Brent A. Sperling, Irene Calizo, Guangjun Cheng, Christina Ann Hacker, Qin Zhang, Yaw Obeng, Kai Yan, Hailin Peng, Qiliang Li, Xiaoxiao Zhu, Hui Yuan, Angela R. Hight Walker, Zhongfan Liu, Lian Mao Peng, and Curt A. Richter. Toward clean and crackless transfer of graphene. *ACS Nano*, 5(11):9144–9153, 2011.

References

- [176] Junmo Kang, Dolly Shin, Sukang Bae, and Byung Hee Hong. Graphene transfer: Key for applications. *Nanoscale*, 4(18):5527–5537, 2012.
- [177] Cheng Gong, Herman Carlo Floresca, David Hinojos, Stephen McDonnell, Xiaoye Qin, Yufeng Hao, Srikar Jandhyala, Greg Mordi, Jiyoung Kim, Luigi Colombo, Rodney S. Ruoff, Moon J. Kim, Kyeongjae Cho, Robert M. Wallace, and Yves J. Chabal. Rapid selective etching of PMMA residues from transferred graphene by carbon dioxide. *Journal of Physical Chemistry C*, 117(44):23000–23008, 2013.
- [178] Di Yan Wang, I. Sheng Huang, Po Hsun Ho, Shao Sian Li, Yun Chieh Yeh, Duan Wei Wang, Wei Liang Chen, Yu Yang Lee, Yu Ming Chang, Chia Chun Chen, Chi Te Liang, and Chun Wei Chen. Clean-lifting transfer of large-area residual-free graphene films. *Advanced Materials*, 25(32):4521–4526, 2013.
- [179] Tomohiro Yasunishi, Yuya Takabayashi, Shigeru Kishimoto, Ryo Kitaura, Hisanori Shinohara, and Yutaka Ohno. Origin of residual particles on transferred graphene grown by CVD. *Japanese Journal of Applied Physics*, 55(8):80305, 2016.
- [180] A. Capasso, M. De Francesco, E. Leoni, T. Dikonimos, F. Buonocore, L. Lancellotti, E. Bobeico, M. S. Sarto, A. Tamburrano, G. De Bellis, and N. Lisi. Cyclododecane as support material for clean and facile transfer of large-area few-layer graphene. *Applied Physics Letters*, 105(11):3–4, 2014.
- [181] Guohui Zhang, Aleix G. Güell, Paul M. Kirkman, Robert A. Lazenby, Thomas S. Miller, and Patrick R. Unwin. Versatile Polymer-Free Graphene Transfer Method and Applications. *ACS Applied Materials and Interfaces*, 8(12):8008–8016, 2016.
- [182] Wei Sun Leong, Haozhe Wang, Jingjie Yeo, Francisco J. Martin-Martinez, Ahmad Zubair, Pin Chun Shen, Yunwei Mao, Tomas Palacios, Markus J. Buehler, Jin Yong Hong, and Jing Kong.

- Paraffin-enabled graphene transfer. *Nature Communications*, 10(1):1–8, 2019.
- [183] Libo Gao, Wencai Ren, Huilong Xu, Li Jin, Zhenxing Wang, Teng Ma, Lai Peng Ma, Zhiyong Zhang, Qiang Fu, Lian Mao Peng, Xinhe Bao, and Hui Ming Cheng. Repeated growth and bubbling transfer of graphene with millimetre-size single-crystal grains using platinum. *Nature Communications*, 3(1):1–7, dec 2012.
- [184] Fangzhu Qing, Yufeng Zhang, Yuting Niu, Richard Stehle, Yuanfu Chen, and Xuesong Li. Towards large-scale graphene transfer, 2020.
- [185] Choon Ming Seah, Brigitte Vigolo, Siang Piao Chai, and Abdul Rahman Mohamed. Transfer of wafer-scale graphene onto arbitrary substrates: Steps towards the reuse and recycling of the catalyst. *2D Materials*, 5(4), 2018.
- [186] Ken Verguts, Koen Schouteden, Cheng Han Wu, Lisanne Peters, Nandi Vrancken, Xiangyu Wu, Zhe Li, Maksiem Erkens, Clement Porret, Cedric Huyghebaert, Chris Van Haesendonck, Stefan De Gendt, and Steven Brems. Controlling Water Intercalation Is Key to a Direct Graphene Transfer. *ACS Applied Materials and Interfaces*, 9(42):37484–37492, oct 2017.
- [187] Ken Verguts, João Coroa, Cedric Huyghebaert, Stefan De Gendt, and Steven Brems. Graphene delamination using 'electrochemical methods': An ion intercalation effect. *Nanoscale*, 10(12):5515–5521, 2018.
- [188] Piran R. Kidambi, Doojoon Jang, Juan Carlos Idrobo, Michael S.H. Boutilier, Luda Wang, Jing Kong, and Rohit Karnik. Nanoporous Atomically Thin Graphene Membranes for Desalting and Dialysis Applications. *Advanced Materials*, 29(33), 2017.

References

- [189] H. Strathmann and K. Kock. The formation mechanism of phase inversion membranes. *Desalination*, 21(3):241–255, 1977.
- [190] Gregory R. Guillen, Yinjin Pan, Minghua Li, and Eric M.V. Hoek. Preparation and characterization of membranes formed by nonsolvent induced phase separation: A review. *Industrial and Engineering Chemistry Research*, 50(7):3798–3817, 2011.
- [191] Reto B. Schoch, Jongyoon Han, and Philippe Renaud. Transport phenomena in nanofluidics. *Reviews of Modern Physics*, 80(3):839–883, 2008.
- [192] Gwan Hyoung Lee, Ryan C. Cooper, Sung Joo An, Sunwoo Lee, Arend Van Der Zande, Nicholas Petrone, Alexandra G. Hammerberg, Changgu Lee, Bryan Crawford, Warren Oliver, Jeffrey W. Kysar, and James Hone. High-strength chemical-vapor-deposited graphene and grain boundaries. *Science*, 340(6136):1073–1076, 2013.
- [193] Aiyi Dong, Qiang Fu, Mingming Wei, Yun Liu, Yanxiao Ning, Fan Yang, Hendrik Bluhm, and Xinhe Bao. Facile oxygen intercalation between full layer graphene and Ru(0001) under ambient conditions. *Surface Science*, 634:37–43, 2015.
- [194] Jinsung Kwak, Se Yang Kim, Yongsu Jo, Na Yeon Kim, Sung Youb Kim, Zonghoon Lee, and Soon Yong Kwon. Unraveling the Water Impermeability Discrepancy in CVD-Grown Graphene. *Advanced Materials*, 30(30):e1800022, 2018.
- [195] Yilun Liu and Xi Chen. Mechanical properties of nanoporous graphene membrane. *Journal of Applied Physics*, 115(3):034303, jan 2014.
- [196] Ardavan Zandiatashbar, Gwan Hyoung Lee, Sung Joo An, Sunwoo Lee, Nithin Mathew, Mauricio Terrones, Takuya Hayashi, Catalin R. Picu, James Hone, and Nikhil Koratkar. Effect of defects on the intrinsic strength and stiffness of graphene. *Nature Communications*, 5:3186, 2014.

- [197] Dechao Geng, Bin Wu, Yunlong Guo, Birong Luo, Yunzhou Xue, Jianyi Chen, Gui Yu, and Yunqi Liu. Fractal etching of graphene. *Journal of the American Chemical Society*, 135(17):6431–6434, 2013.
- [198] Liming Xie, Liying Jiao, and Hongjie Dai. Selective etching of graphene edges by hydrogen plasma. *Journal of the American Chemical Society*, 132(42):14751–14753, 2010.
- [199] Xinran Wang and Hongjie Dai. Etching and narrowing of graphene from the edges. *Nature Chemistry*, 2(8):661–665, 2010.
- [200] Zhu Jun Wang, Gisela Weinberg, Qiang Zhang, Thomas Lunkenbein, Achim Klein-Hoffmann, Michalina Kurnatowska, Milivoj Plodinec, Qing Li, Lifeng Chi, R. Schloegl, and Marc Georg Willinger. Direct observation of graphene growth and associated copper substrate dynamics by in situ scanning electron microscopy. *ACS Nano*, 9(2):1506–1519, feb 2015.
- [201] Zhu Jun Wang, Jichen Dong, Yi Cui, Gyula Eres, Olaf Timpe, Qiang Fu, Feng Ding, R. Schloegl, and Marc Georg Willinger. Stacking sequence and interlayer coupling in few-layer graphene revealed by in situ imaging. *Nature Communications*, 7:1–12, 2016.
- [202] Zhu Jun Wang, Feng Ding, Gyula Eres, Markus Antonietti, Robert Schloegl, and Marc Georg Willinger. Formation Mechanism, Growth Kinetics, and Stability Limits of Graphene Adlayers in Metal-Catalyzed CVD Growth. *Advanced Materials Interfaces*, 5(14):1–7, 2018.
- [203] Cédric Barroo, Zhu Jun Wang, Robert Schlögl, and Marc Georg Willinger. Imaging the dynamics of catalysed surface reactions by in situ scanning electron microscopy. *Nature Catalysis*, 3(1):30–39, 2020.

References

- [204] Zhu Jun Wang, Jichen Dong, Linfei Li, Guocai Dong, Yi Cui, Yang Yang, Wei Wei, Raoul Blume, Qing Li, Li Wang, Xiaozhi Xu, Kaihui Liu, Cédric Barroo, Joost W.M. Frenken, Qiang Fu, Xinhe Bao, Robert Schlögl, Feng Ding, and Marc Georg Willinger. The Coalescence Behavior of Two-Dimensional Materials Revealed by Multiscale in Situ Imaging during Chemical Vapor Deposition Growth. *ACS Nano*, 14(2):1902–1918, feb 2020.
- [205] Oleg V. Yazyev and Yong P. Chen. Polycrystalline graphene and other two-dimensional materials. *Nature Nanotechnology*, 9(10):755–767, 2014.
- [206] Philippe Thévenaz, Urs E. Ruttimann, and Michael Unser. A pyramid approach to subpixel registration based on intensity. *IEEE Transactions on Image Processing*, 7(1):27–41, 1998.
- [207] Wei Kong, Hyun Kum, Sang Hoon Bae, Jaewoo Shim, Hyunseok Kim, Lingping Kong, Yuan Meng, Kejia Wang, Chansoo Kim, and Jeehwan Kim. Path towards graphene commercialization from lab to market. *Nature Nanotechnology*, 14(10):927–938, 2019.
- [208] Terrance Barkan. Graphene: the hype versus commercial reality. *Nature Nanotechnology*, 14(10):904–906, 2019.

Curriculum Vitae

Personal Information

Karl-Philipp Schlichting

Date and Place of Birth: 9.02.1990, Stuttgart, Germany

Education & Professional Experience

- | | | |
|----------------------|--|------------------------|
| 09/2015 –
12/2020 | Doctoral Studies, ETH Zurich | Zurich,
Switzerland |
| | Department of Mechanical & Process Engineering
Experimental mass transport across nanoporous graphene membranes | |
| 09/2014 –
03/2015 | Master Thesis, Georgia Institute of Technology | Atlanta, USA |
| | School of Mechanical Engineering
Numerical heat and mass transport studies:
Coding of a finite element solver for heat and mass diffusion. Analysis and optimization of heat transfer and chemical kinetics in a chemical reactor driven concentrated solar irradiation. | |

8. Curriculum Vitae

- 09/2013 – **Master of Science, ETH Zurich (grade: 5.43/6)** Zurich, Switzerland
03/2015
Department of Mechanical & Process Engineering
Focus on heat and mass transfer: Computational fluid dynamics, renewable energies and sustainable technologies.
Research project using computational fluid dynamics to simulate particle-laden flows in a hydrothermal reactor.
- 06/2013 – **Volkswagen AG** Wolfsburg, Germany
09/2013
Coorporate Research & Developemt internship
Development of a thermal conductivity measurement device for fuel cell components.
- 09/2010 – **Bachelor of Science, ETH Zurich (grade: 4.74/6)** Zurich, Switzerland
06/2013
Department of Mechanical & Process Engineering
achelor thesis: Monte Carlo based heat transfer simulationsof concentrated solar irradiation coupled with convective cool-ing for concentrated solar power plants.
- 09/2009 – **Senvion AG** Hamburg, Germany
08/2010
Internal & External Communication
- 06/2009 – **Hauni Maschinenbau GmbH** Reinbek, Germany
08/2009
Metal working internship
- 2001 – **Abitur, Sachsenwaldschule Reinbek** Reinbek, Germany
2009
Final grade: 1.7

Publications

Scientific Journals and Books

1. **Schlichting, K.-P.**, Poulikakos D. (2020). Selective Etching of Graphene Membrane Nanopores: From Molecular Sieving to Extreme Permeance. **ACS Applied Materials & Interfaces**. DOI:10.1021/acscami.0c07277
2. Buchheim, J.*, **Schlichting, K.-P.***, Wyss, R.M., Park, H.G. (2018). Assessing the Thickness-Permeation Paradigm in Nano-porous Membranes. **ACS Nano**. DOI:10.1021/acsnano.8b04875 (*equal contribution)
3. **Schlichting, K.-P.**, H.G. Park (2018). Mass Transport across Atomically Thin Membranes. **Graphene-based Membranes for Mass Transport Applications**.
4. Choi, K., Droudian A., Wyss, R.M., **Schlichting, K.-P.** Park, H.G. (2018). Multifunctional Wafer-Scale Graphene Membranes for Fast Ultrafiltration and High Permeation Gas Separation. **Science Advances**, DOI:10.1126/sciadv.aau0476
5. Bush, H. E., **Schlichting, K.-P.**, Gill, R. J., Jeter, S. M., & Loutzenhiser, P. G. (2017). Design and Characterization of a Novel Upward Flow Reactor for the Study of High-Temperature Thermal Reduction for Solar-Driven Processes. **Journal of Solar Energy Engineering**. DOI:10.1115/1.4037191

Patents

Schlichting, K.-P.* (2019) METHOD FOR MAKING POROUS FILTER MEMBRANES. **Priority filing**

Conference Presentations

1. **Schlichting, K.-P.*** (2019). Gas Permeation and Separation Across Selectively Etched Nanoporous Graphene Membranes. **Materials Research Society**. Fall Meeting, Boston, USA
2. **Schlichting, K.-P.** Rational Thickness of Nanoporous Membranes (2018) **From solid state to biophysics conference**, Dubrovnik, Croatia
3. **Schlichting, K.-P.** Rational Thickness of Nanoporous Membranes (2018) **Materials and Processes Graduate Symposium, ETH Zurich**, Switzerland